Theory of Ultracold Atomic Collisions in Radio-frequency Fields

Daniel J. Owens

A Thesis presented for the degree of
Doctor of Philosophy

Joint Quantum Centre Durham-Newcastle
Department of Chemistry
University of Durham

November 2018

Theory of Ultracold Atomic Collisions in Radio-frequency Fields

Abstract

This thesis has investigated the dynamics of ultracold atomic collisions in the presence of both static magnetic and oscillating radio-frequency (rf) fields.

The boundstate structure and scattering length of ^{39}K+^{133}Cs was examined in the presence of only a static magnetic field, where it was found that no Feshbach resonance of suitable width for magnetoassociation existed at a magnetic field where caesium can be cooled to degeneracy. We then showed that zero-energy Feshbach resonances may be engineered using an rf field in places where they did not previously exist. An rf field with frequency 79.9 MHz was chosen to induce a resonance near 21 G. The widths of such rf-induced Feshbach resonances increase quadratically with rf field strength. The resonances presented are lossless with circularly polarized rf, and the molecules created are long-lived even with plane-polarized RF.

Collisional losses in rf-dressed magnetic traps were also investigated. An rf-induced loss mechanism that does not exist in the absence of rf radiation was identified. This mechanism is not suppressed by a centrifugal barrier in the outgoing channel, and can be much faster than spin relaxation, which is centrifugally suppressed. We explore the dependence of the rf-induced loss rate on singlet and triplet scattering lengths, hyperfine splittings and the strength of the rf field. The results were interpreted in terms of an adiabatic model of the collision dynamics, and calculate the corresponding nonadiabatic couplings. The loss rate can vary by 10 orders of magnitude as a function of singlet and triplet scattering lengths. ^{87}Rb is a special case, where several factors combine to reduce rf-induced losses; as a result, they are slow compared to spin-relaxation losses. For most other alkali-metal pairs, rf-induced losses are expected to be much faster and may dominate. For heteronuclear mixtures an rf-modified spin-exchange mechanism was identified that results in loss rates orders of magnitude greater than the rf-induced loss rates in homonuclear cases. Fast loss is expected in mixtures where the Landé g-factors differ.

Declaration

I confirm that no part of the material offered has previously been submitted by myself for a degree in this or any other University. Where material has been generated through joint work, the work of others has been indicated.

Acknowledgements

Many thanks to my supervisor Jeremy Hutson for his guidance and for pushing me to do my best over the past four years. My thanks also extend to the current and previous members of the research group including Ruth Le Sueur, Matthew Frye, Christophe Vailant, Caroline Blackely, Ting Xie, Dermot Green, Masato Morita, Tijs Carman and Baochun Yang who have contributed to my work through informative discussions, helped wrangle MOLSCAT into submission and provided encouragement when I needed it most. Thanks also to Christopher Foot and Elliot Bentine in the physics department of Oxford University for their support, and without whom I would not have become interested in key aspects of the work presented in this thesis. Finally, thanks to the EPSRC for the funding this PhD.

Contents

List of Figures

List of Tables

Chapter 1

Introduction

The areas of ultracold chemistry and physics (generally defined as systems below a temperature of 1 mK) have seen significant progress in the previous two decades. The road to ultracold temperatures has been paved with important scientific discoveries such as superconductivity [1] and superfluidity [2, 3], culminating in the observation of the Bose-Einstein Condensate (BEC) [4, 5] for which the Nobel prize in physics was awarded in 2001[6, 7]. The existence of the BEC was theorised by Bose and Einstein in 1924 [8, 9], and so this achievement represents a significant advance in experimental physics over the course of the 20th century. Since the first observation of the atomic BEC the field of ultracold science has exploded and is now more than ever full of exciting future applications.

Ultracold matter does not behave like the objects we encounter day-to-day. When the temperature is reduced to near absolute zero the translational motion of matter is greatly reduced and the classical theories we are familiar with break down as quantum-mechanical effects dominate and become apparent on the macroscopic scale. Bohr's correspondence principle applies in the limit of large quantum numbers, but in the ultracold regime the quantum numbers needed to describe available states are small; the averaging over high quantum number states that marks a convergence of quantum and classical mechanics is lost, and systems at ultracold temperatures can often be described using relatively few states. Matter also becomes more wave-like as temperature decreases; the wave nature of a particle can

be quantified by the de Broglie wavelength,

$$\lambda_{\mathrm{dB}} = \frac{h}{p} = \frac{h}{\sqrt{2mE}} \tag{1.0.1}$$

where h is Planck's constant, p is the momentum of the particle, m is the particle mass and E is the kinetic energy of the particle. The de Broglie wavelength can be thought to characterise the space occupied by a particle, and as λ_{dB} becomes comparable to the inter-particle separation with decreasing temperature, the wave-functions of these particles can interfere with one another to form a single coherent wave. If the particles are bosons (particles possessing integer spin) this state of matter is known as a BEC, a macroscopic quantum state in which all the bosons are in the same quantum state ie quantum degenerate. Fermions (particles possessing half-integer spin) exhibit different behavior due to the Pauli principle, which means identical fermions may not exist in the same state. This leads to the fermionic analogue of the BEC, the Degenerate Fermi-Gas (DFG) [10], where the lowest number of possible states are occupied for a given number of particles. The force that prevents white dwarf and neutron stars from collapsing is also a result of the Pauli principle, and is known as Fermi-degeneracy pressure [11].

1.1 Ultracold Atoms and Molecules

The controlled cooling and trapping of atoms has been possible for over two decades, with the first experiments reaching sub-mK temperatures in the 1980s [12–15]. Laser cooling [16–18] is an extremely important technique in the production of ultracold atoms, the development of which won the Nobel prize in physics in 1997 [19]. Laser cooling relies upon an absorption-emission cycle, which slows and cools the atoms through the absorption of photons with a linear momentum opposite to the target atoms. In a specific form of laser cooling known as Doppler cooling this is done by red-detuning pairs of counter-propagating laser beams for each Cartesian axis; atoms traveling towards a laser source will absorb photons whose frequency is blue-shifted to atomic resonance, be slowed and pushed back into the trap. The reliance of laser cooling upon photon absorption/emission means that temperatures are ultimately

limited by photon recoil, and so it is rarely used in isolation. It is often employed as a precursor to other techniques which require a relatively cold sample to begin with such as evaporative cooling [20] which can reach temperatures in the tens of nK. Evaporative cooling works by removing the most energetic atoms from the tail of the Maxwell-Boltzmann distribution; energetic pathways are provided only to atoms in higher states by manipulating the trapping potential, effectively cooling the system. An everyday analogue to this is blowing on your cup of tea to cool it down - by removing the water molecules with above average energy from the surface of the tea the temperature of the cup as a whole is decreased.

Since the first atomic BECs were created using sodium and rubidium-87 [4, 5], many other atoms have been successfully cooled to degeneracy. These are predominately alkali-metal species, with BECs of lithium, potassium, 85-rubidium and caesium have all been successfully produced [21–24]. Fermionic isotopes have also been cooled to degeneracy with DFGs of potassium and lithium having been successfully produced [10, 25]. Beyond the alkali metals, degeneracy has also been reached with hydrogen [26], alkaline-earth metals calcium and strontium [27, 28], the transition metal chromium [29] and the alkaline-earth-like lanthanide ytterbium [30]. Recent interest in the large electric and magnetic dipole moments of high-spin species has lead to an interest in the condensates of lanthanides erbium and dysprosium [31–33].

Following the successes in cooling atomic gases to ultracold temperatures, the next logical step is the translation of these techniques to the production of quantum degenerate molecules. Molecular structure is relatively complex compared to atoms; in even the simplest diatomic molecule there are rotational and vibrational energy levels to consider on top of the hyperfine structure of each atom. This extra structure provides opportunities to build systems where a variety of interactions can be altered by choosing appropriate molecules, and these interactions can be tuned by manipulating molecular energy levels with external fields [34]. For these reasons making ultracold molecules has become a major priority in the field in the past decade or so.

Whilst cold molecules have been produced successfully since 1998 [35], reaching ultracold temperatures presents significant challenges. The complexities of

molecular structure that offer new opportunities in the field also result in difficulties reaching ultracold temperatures with techniques that have been successful for atoms. Direct cooling methods like laser cooling become difficult because of the large number of quantum states available to a molecule; losses to states outside the core absorption-emission loop are much more likely. While examples of direct laser cooling of molecules do exist [36–47], its limitations are much more apparent in the molecular world. Much more prevalent in the production of ultracold molecules are indirect methods such as photoassociation [48] where colliding atoms are associated with the aid of a photon, and magnetoassociation [49–53], which associates colliding atoms by tuning magnetic fields such that the colliding atoms end up in a bound state. Magnetoassociation has been investigated in several homonuclear alkali-metal systems [54–60] and heteronuclear systems such as rubidium-caesium [61–65], potassium-caesium [66, 67], potassium-rubidium [68, 69], rubidium-strontium [70] and sodium-potassium [71]. These indirect methods are advantageous because the processes are adiabatic in principle meaning the resultant molecules inherit the temperature of the constituent atoms.

1.1.1 Applications of Ultracold Atoms and Molecules

An exciting and potentially far-reaching application of ultracold atoms and molecules is the development of quantum computing [72–74]. The manipulation of long-range interactions between atoms or molecules trapped in lattices is one proposed way to store information; molecules with permanent electric and magnetic dipoles are of particular interest for this. The full realisation of a functioning quantum computer in this fashion is still some way off, but quantum simulation [75, 76] is a more immediate goal; complicated Hamiltonians that modern CPUs cannot diagonalise in a realistic time frame can be mimicked experimentally by manipulating inter-lattice interactions between atoms/molecules and the solutions obtained by observation.

Production of atoms and molecules in specific quantum states has advantages for ultra-precise spectroscopy [77]. With the removal of thermal averaging and the population of a single state, transitions to more coherent and longer-lived excited states are possible, contributing to a greater signal-to-noise ratio. The accuracy of

spectroscopic measurements is also improved due to the reduction in the broadening of spectral lines due to the low velocity spread of atoms and molecules in the ultracold regime. The accuracy of ultracold spectroscopy has greatly reduced the uncertainties in atomic clocks [78, 79], which are the current standard of time with the SI second defined by a hyperfine transition in caesium.

The sensitivity of ultracold systems to very small changes is important to testing our understanding of fundamental principles in physics. In particular, some molecules may be sensitive to small changes in fundamental constants that atoms are not. Ultracold molecules may allow us to measure these changes such as the time variation of the proton-electon mass ratio ($m_{\mathrm{p}}/m_{\mathrm{e}}$) [80–82]. Testing physics beyond the standard model may also be aided by ultracold atoms and molecules, such as the search for the Electron Dipole Moment (EDM) [83–85] and even the identification of dark matter [86].

In recent years there has been considerable interest in signatures of quantum chaos in atomic collisions [33]. Complex atomic species such as ytterbium, erbium and dysprosium have been investigated in this context [31, 32, 87, 88], as have collisions involving molecules such as CaH and CaF [89].

Control over atomic and molecular motion may lead to exciting possibilites such as controlled chemical reactions [90], where the reactants are individually manipulated; atomic and molecular motions in the ultracold regime are generally slow enough that perturbations from external fields are enough to control the relative positions and orientations. Selection of the quantum states participating in potentially reactive collisions may lead to opportunities for further control by allowing or disallowing collisional processes as demonstrated for Li + CaH [91, 92]. Chemical reactions at such temperatures would also be subject to quantum-mechanical effects unobservable at temperatures beyond the mK range, allowing further insight into qunatum-tunnelling dependent reaction rates and quantum threshold effects [93].

1.2 Radio-frequency Fields

The applications of ultracold atoms and molecules are dependent upon manipulating them with the aid of external fields. Static magnetic and electric fields are typically used in this capacity, and they are often accompanied by oscillating electromagnetic fields such as radio-frequency (rf) fields which can induce transitions between hyperfine states in the trapped atoms. These transitions can be controlled by adjusting the frequency, amplitude and polarisation of the rf field, as well as the angle it makes with the quantisation axis.

The technique of rf spectroscopy has a rich history, notably providing the current standard of time as defined by an rf hyperfine transition in ground state caesium [94]. Spectroscopy of ultracold systems using rf radiation was first demonstrated 30 years ago with the measurement of the size and temperature of a cloud of ultracold atoms [95] and has since been used to determine molecular binding energies by directly measuring bound-state energies [96] as well as confirming the creation of Feshbach molecules through their rf-dissociation spectra [97]. Direct measurement of mean-field interaction energies using rf spectroscopy has also allowed the determination of the s-wave scattering length near a Feshbach resonance [98, 99].

As well as simply probing ultracold atoms, rf radiation has also been key to reaching temperatures and densities needed to produce BECs. Using an rf field to drive hyperfine transitions of atoms with above average energy in a trap to untrapped states is an effective form of evaporative cooling known as an rf knife [100].

Modification of scattering properties using rf radiation to dress individual species in a mixture offers opportunities for further control over ultracold systems [101], and this type of dressing has been suggested as a way to modify existing Feshbach resonances [102, 103]. Molecule formation via rf-association of atoms has been demonstrated [104–107], as has the association of atoms into Effimov trimers using rf fields [108–110].

Modification of traditional traps for ultracold atoms using additional electromagnetic fields is well established [111–113]. In particular, rf-dressed magnetic traps [114–118] use the interaction of different hyperfine states coupled together via the rf field to trap atoms. This allows the creation of complex and novel trap geometries

such as rings [119–121] and shells [117]. These geometries are valuable in many fields including condensate splitting and interferometry [122–125], and the study of low-dimensional quantum systems [118, 126]. Besides modifying magnetic traps, rf fields have also been used to alter optical lattices [127, 128] and create periodic potential landscapes [129, 130]. Measurement of the interaction energies between lattice sites is also possible with rf fields [131].

This thesis focuses on the theory of ultracold atomic collisions in the presence of an rf field in combination with a static magnetic field. The interaction of the atoms with the rf field is presented in a dressed atom picture. To understand the collisional processes that occur, an understanding of scattering theory and atomic structure is required.

1.3 Scattering and Coupled Channel Calculations

Because de Broglie wavelengths are comparable to atomic separation at the temperatures considered in this work atomic collisions can be considered quantum-mechanical in nature, requiring the use of a quantum collision theory. Both the underlying scattering theory and its context within quantum mechanics is discussed in great detail and at its full breadth elsewhere [132]. Below is a brief overview of scattering in the context of atomic collison based upon reference [133] where aspects of scattering unique to ultracold collisions are dicussed, as are the Hamiltonians for the specific case of collisions between ^{1}S alkali-metal atoms in the presence of a magnetic field and the case of the same collision in a combination of magnetic and rf fields.

1.3.1 Scattering Theory

Whilst the work of this thesis revolves around the scattering of *structured* particles (specifically atoms with hyperfine levels), we can understand a great deal about scattering if we first consider collisions between *structureless* particles. The wavefunction for such a system in the absence of any scattering is a plane wave of form $e^{i\boldsymbol{kR}}$ where $\boldsymbol{k}$ is the wave vector with corresponding magnitude (wave number) k,

and $\boldsymbol{R}$ is the inter-particle distance. In the presence of scattering the wavefunction behaves approximately as an interference of the plane wave with a spherical wave dependent on a scattering angle, θ

$$\Psi(R) \approx \Psi_0(R) + f(\theta)\frac{e^{ikR}}{R} \quad \text{as} \quad R \to \infty \tag{1.3.2}$$

where $\Psi_0(R)$ is the incoming plane wave and $f(\theta)$ is the scattering amplitude. When no scattering event takes place the spherical component and, thus, $f(\theta)$ is zero. We can then introduce this wavefunction in the time-independent Schrödinger equation

$$\hat{H}\Psi(R) = E\Psi(R) \tag{1.3.3}$$

$$\left[\frac{-\hbar^2}{2\mu}\nabla^2 + V(R)\right]\Psi(R) = E\Psi(R) \tag{1.3.4}$$

where $\hat{H}$ is the Hamiltonian, $\mu = (m_1 m_2)/(m_1 + m_2)$ is the reduced mass for the system, $(-\hbar^2/2\mu)\nabla^2$ is the kinetic energy operator, $V(R)$ is the potential for the collision and E is the collision energy. E is usually measured relative to the energy of the separated particles so that $V(R) \to 0$ as $R \to \infty$. $\Psi(R)$ can be expanded in spherical harmonics

$$\Psi(R) = R^{-1}\sum_l \psi_L(R)P_L(\cos\theta) \tag{1.3.5}$$

where P_L are Legendre polynomials. The L subscript refers to a quantised angular momentum given by the orbital angular momentum operator $\hat{L} = \boldsymbol{R} \times \hat{p}$, where $\hat{p}$ is the linear momentum operator. Substituting 1.3.5 into equation 1.3.4 gives

$$\left[\frac{-\hbar^2}{2\mu}\frac{d^2}{dR^2} + V_L(R)\right]\psi_L(R) = E\psi_L(R) \tag{1.3.6}$$

where $V_L(R)$ is the centrifugally corrected interaction potential:

$$V(R) + \frac{\hbar^2 L(L+1)}{2\mu R^2} \tag{1.3.7}$$

The $L(L+1)$ term introduces a centrifugal barrier to the potential for $L > 0$. We can apply boundary conditions to 1.3.6 by noting that $V(R) \gg 0$ at $R = 0$, and

$V(R) \to 0$ as $R \to \infty$.

$$\psi_L(R) \to 0 \quad \text{as} \quad \mathrm{R} \to 0 \tag{1.3.8}$$

$$\psi_L(R) \approx kRj_L(kR + \eta_L) \quad \text{as} \quad \mathrm{R} \to \infty \tag{1.3.9}$$

where j_L are spherical Bessel functions, kRj_L is the solution to 1.3.6 with $V(R) = 0$ (a situation where the particles are non-interacting) and η_L is the phase shift. The spherical Bessel functions have asymptotic form

$$j_L \approx (kR)^{-1} \sin(kR - \frac{L\pi}{2}) \tag{1.3.10}$$

which allows us to rewrite the asymptotic scattering wavefunction as

$$\psi_L \approx (kR)^{-1} \sin(kR - \frac{L\pi}{2} + \eta_L) \tag{1.3.11}$$

In an attractive potential equation 1.3.6 also supports bound states (states with quantised energies less than the separated atoms) as well as scattering states. Bound states require a different boundary condition at short range:

$$\psi_L(R) \to 0 \quad \text{as} \quad R \to \infty \quad \text{or} \quad R \to 0 \tag{1.3.12}$$

1.3.2 Coupled-Channel Equations

In real systems we have interactions between particles with structure. The Hamiltonian of equation (1.3.6) must be re-written to take into account the structure of the colliding particles:

$$\frac{-\hbar^2}{2\mu}\nabla^2 + \sum_i \hat{h}_i^{\text{internal}}(\tau) + V_L(R, \tau) \tag{1.3.13}$$

We introduce τ to represent all coordinates except the interparticle distance, R. The internal Hamiltonians for both particles, contained within the sum $\sum \hat{h}_i^{\text{internal}}(\tau)$, are independent of R while the potential, $V(R, \tau)$, now depends upon these extra degrees of freedom. We can now think of the wavefunction as a combination of

radially dependent wavefunctions, $\psi(R)$, and wavefunctions dependent on the other coordinates, $\phi(\tau)$

$$\Psi(R,\tau) = R^{-1}\sum_i \phi_i(\tau)\psi_i(R) \tag{1.3.14}$$

$\phi_i(\tau)$ form a basis set in τ and are referred to as channel functions. These channel functions can be chosen to best suit a system, for example in this work electron and nuclear spin functions are used for alkali-metal atoms, and these are combined with photon numbers and associated angular momentum to build a photon-dressed basis set (see Section 1.5). Regardless of what channel functions are chosen, it is important the size of the basis set be large enough to reach numerical convergence.

$\psi_i(R)$ is typically propagated numerically on a grid. By applying 1.3.14 to the Schrödinger equation and projecting onto the basis function ϕ_j, we obtain sets of coupled equations:

$$\left[\frac{-\hbar^2}{2\mu}\frac{d^2}{dR^2} - E\right]\psi_j(R) = -\sum_i W_{ji}(R)\psi(R) \tag{1.3.15}$$

where $W_{ji}(R)$ are elements of the interaction matrix $\boldsymbol{W}$, given by

$$W_{ji}(R) = \int \phi_j(\tau)^* \left[\sum_i \hat{h}_i^{\text{internal}}(\tau) + V(R,\tau) + \frac{\hat{L}^2}{2\mu R^2}\right]\phi_i(\tau) \tag{1.3.16}$$

$\boldsymbol{W}$ can be rotated into a basis where it is diagonal asymptotically, if it is not already, and its elements correspond to different configurations of the particles at $R = \infty$. These diagonal elements describe the possible collision channels which, depending on their energy relative to the kinetic energy of the colliding particles, E, either energetically *open* ($W_{ii} < E$) or *closed* ($W_{ii} > E$). All open channels are available for scattered particles to occupy; conceptually we envisage an incoming wave in a single channel, and outgoing waves in all open channels. The boundary conditions for the scattering wavefunctions are

$$\Psi(R,\tau) = 0 \quad \text{as} \quad R \to 0 \tag{1.3.17}$$

$$\Psi(R,\tau) \approx R^{-1}\left[\phi_j k_j^{1/2} e^{-ik_j R + iL_j\pi/2} + \sum_i S_{ji}\phi_i(\tau) k_i^{1/2} e^{ik_i R + iL_i\pi/2}\right] \quad \text{as} \quad R\to\infty \tag{1.3.18}$$

Boundary condition 1.3.18 has a solution for each allowed incoming channel; the first term within the brackets refers to the incoming wave in channel j, and the sum over i takes into account scattered waves into every open channel. S_{ij} are elements of the S-matrix, $\mathbf{S}$, an $N_{\text{open}} \times N_{\text{open}}$ matrix (where N_{open} refers to the number of open channels) which characterises each solution and from which we can obtain most of the useful information we need about a collision. However, the short range boundary condition 1.3.17 is not unique to any one solution for the long range condition 1.3.18. We can have a total of N solutions where N is the number of channel functions, and each solution is a vector of length N. Because we can't know which combination we will need it is standard practice to propagate each solution to long range as part of a $N \times N$ wavefunction matrix, $\mathbf{\Psi}(R)$. Although these solutions are not necessarily real we can choose real solutions for convenience, such solutions at long range are subject to the boundary condition

$$\mathbf{\Psi}(R) = \mathbf{J}(R) + \mathbf{N}(R)\mathbf{K} \quad \text{as} \quad R\to\infty \tag{1.3.19}$$

where $\mathbf{J}$ and $\mathbf{N}$ are diagonal matrices with open and closed channel elements which are composed of spherical Bessel functions. $\mathbf{K}$ is a real symmetric matrix indicative of the asymptotic wavefunction, from which the S-matrix can be found:

$$\mathbf{S} = (1 + i\mathbf{K}_{\text{oo}})^{-1}(1 - \mathbf{K}_{\text{oo}}) \tag{1.3.20}$$

Where the subscript oo refers to the diagonal open channel-open channel part of $\mathbf{K}$. The S-matrix has diagonal elements

$$S_{ii} = e^{2i\eta_i} \tag{1.3.21}$$

The S-matrix contains information about the completed scattering event.

1.3.3 Numerical Propagation of the Wavefunction

As mentioned above, numerical propagation of $\mathbf{\Psi}(R)$ to long range is required to obtain the correct combination of solutions. However, problems arise from the propagation of $\mathbf{\Psi}(R)$ directly; in the classically forbidden regions of the potentials channel functions originating from closed channels can be numerically unstable causing the wavefunction to explode exponentially. To avoid this, propagation of the log-derivative matrix [134–138] can be carried out. A more in depth discussion on the numerical methods described below can be found in ref [139].

The log-derivative wavefunction is written as

$$\mathbf{Y}(R) = \frac{d}{dR} \ln \mathbf{\Psi}(R) \tag{1.3.22}$$

$$\mathbf{Y}(R) = \frac{d\mathbf{\Psi}}{dR} \left[\mathbf{\Psi}(R)\right]^{-1}. \tag{1.3.23}$$

$\mathbf{Y}(R)$ is then propagated from a point within the inner classically forbidden region R_{min}, to a point at long range R_{max}, chosen to be far enough outside the potential well that $V(R)$ is essentially 0. The K-matrix can then be obtained from the asymptotic wavefunction, but we do not need this explicitly as we can use the log-derivative wavefunction

$$\mathbf{K} = -\frac{\mathbf{Y}(R_{\text{max}})\mathbf{N}(R_{\text{max}}) - \mathbf{N}'(R_{\text{max}})}{\mathbf{Y}(R_{\text{max}})\mathbf{J}(R_{\text{max}}) - \mathbf{J}'(R_{\text{max}})} \tag{1.3.24}$$

The S-matrix can then calculated from $\mathbf{K}$ by using the relation (1.3.20).

For bound states the propagation is two-fold with an inwards propagation denoted $\mathbf{Y}^{-}$ from a maximum, R_{max}, chosen to be within the outer clasically forbidden region, and an outwards propagation denoted $\mathbf{Y}^{+}$ from a minimum, R_{min}, chosen to be within the inner classically forbidden region. These two propagations are matched at a point, R_{mid}, chosen to be in the classically allowed region. If the energy for the chosen propagation is an eigenvalue then

$$\Psi^{+}(R_{\text{mid}}) = \Psi^{-}(R_{\text{mid}}) \quad \text{and} \quad \left[\Psi^{+}\right]'(R_{\text{mid}}) = \left[\Psi^{-}\right]'(R_{\text{mid}}) \tag{1.3.25}$$

must be true. We can now write

$$\left[Y^{+}(R_{\text{mid}}) - Y^{-}(R_{\text{mid}})\right] \Psi(R_{\text{mid}}) = 0 \tag{1.3.26}$$

Note that $\Psi(R_{\text{mid}})$ is an eigenvector of $[Y^{+}(R_{\text{mid}}) - Y^{-}(R_{\text{mid}})]$. This is only valid if

$$\det|Y^{+} - Y^{-}| = 0 \quad \text{at} \quad R_{\text{mid}} \tag{1.3.27}$$

Thus we can identify the energies where a bound state exists by looking for zeroes in the determinant of the log-derivative matrix.

1.3.4 Ultracold Scattering

Scattering in the ultracold regime can be viewed as more straightforward in some respects when compared to scattering at higher temperatures due to the fact that a relatively small number of quantum states and partial waves contribute to scattering events. Ultracold scattering can consequently be more easily understood by focusing on specific incoming channels and predicting the relatively few outgoing channels.

An important property when studying scattering is the k-dependent scattering length, $a_L(k)$, where k is the wave vector of the incoming channel and the L subcript is the partial wave of the channel. $a_L(k)$ is dependent on the phase shift, η_L, resulting from an elastic collison and is given by

$$a_L(k) = \frac{-\tan \eta_L}{k} \tag{1.3.28}$$

in the single channel case. At very low energy the interactions between atoms may be characterised by just the s-wave scattering length, $a(k)$; the kinetic energy of the collisions at such low temperatures are often not great enough to overcome the centrifugal barriers presented by end-over-end angular momenta $L \geq 1$, so s-wave collisions with $L = 0$ tend to dominate. The dependence of the scattering length upon energy also disappears as the temperature approaches zero so we can think of an ultracold collision being characterised by a k-independent s-wave scattering length, a.

The scattering length can be understood physically by looking at the behaviour of the wavefunction. Within the range of the potential well the wavefunction oscillates, as it leaves this range it oscillates less and less eventually becoming a straight line asymptotically. The inter-particle distance at which this straight line or its extrapolation crosses is equal to the scattering length. This is equivalent to the radius of a hard-sphere potential with an infinite wall at $R = a$, and so in some sense gives a sense of the size of the colliding particles. The scattering length can take a positive or negative value; a positive value indicates a repulsive interaction between the particles as there exists an effective hard sphere, as described above. A negative value relates to an attractive interaction as the wall of the hard sphere exists at negative R, where the colliding particles won't experience it.

In the multichannel case with more than one open channel the scattering length becomes complex,

$$a = \alpha - i\beta, \tag{1.3.29}$$

where α and β are the respective real and imaginary components which contain information about elastic and inelastic scattering, respectively. a is calculated from the diagonal elements of the S-matrix

$$a = \frac{1}{ik}\left(\frac{1 - S_{ii}(k)}{1 + S_{ii}(k)}\right). \tag{1.3.30}$$

1.4 Alkali-Dimer Systems

This thesis focuses on the scattering of alkali-metal atoms in combined magnetic and rf fields and so it is necessary to understand their structure. Equation 1.3.13 contained a term for the sum of internal Hamiltonians for each particle of the system of interest, $\sum_i \hat{h}_i^{\text{internal}}$. For an individual alkali-metal atom this internal Hamiltonian is

$$\hat{h}_{\text{alk}} = \zeta \hat{i} \cdot \hat{s} + (g_e \mu_{\text{B}} \hat{s}_z + g_n \mu_{\text{B}} \hat{i}_z) B_z, \tag{1.4.31}$$

where the first term is the hyperfine interaction of the nuclear and electronic spins, where ζ is the hyperfine coupling constant and $\hat{i}$ and $\hat{s}$ are the nuclear and electronic spin angular momentum operators. The hyperfine interaction has non-zero matrix

elements given by

$$\langle i\, m_i,\, s\, m_s|\hat{i}\cdot\hat{s}|i\, m_i,\, s\, m_s\rangle = m_i m_s \tag{1.4.32}$$

and

$$\begin{aligned}\langle i\, m_i,\, s\, m_s|\hat{i}\cdot\hat{s}|i\, m_i \pm 1,\, s\, m_s \mp 1\rangle = \\ \frac{1}{2}[s(s+1) - m_s(m_s \pm 1)]^{1/2}[i(i+1) - m_i(m_i \pm 1)]^{1/2}\end{aligned} \tag{1.4.33}$$

where $m_{i/s}$ is the projection of the nuclear/electronic spin onto the quantisation axis. The second term of 1.4.31 is the Zeeman interaction of the spin projections with an external magnetic field of strength B_z which defines the quantisation axis, where g_e and g_n are the electronic and nuclear g-factors, respectively, which are chosen to follow the convention of Arimondo *et al.* [140], and $\hat{i}_z$ and $\hat{s}_z$ are the nuclear and electronic spin projection operators which have matrix elements

$$\langle i, m_i|\hat{i}_z|i', m_i'\rangle = \delta_{i,i'}\delta_{m_i,m_i'}m_i \tag{1.4.34}$$

$$\langle s, m_s|\hat{s}_z|s', m_s'\rangle = \delta_{s,s'}\delta_{m_s,m_s'}m_s \tag{1.4.35}$$

The total Hamiltonian for the dimer is then

$$\frac{\hbar^2}{2\mu}\left[R^{-1}\frac{d^2}{dR^2}R + \frac{\hat{L}}{R^2}\right] + \hat{h}^a_{\text{alk}} + \hat{h}^b_{\text{alk}} + \hat{V}(R) \tag{1.4.36}$$

where we include two distinct $\hat{h}_{\text{alk}}$, one for each alkali-metal atom denoted by the a/b superscript. This thesis presents scattering and bound state calculations of alkali-dimer systems using this Hamiltonain and the decoupled basis

$$|s_{\text{a}}, m_{s,\text{a}}\rangle|i_{\text{a}}, m_{i,\text{a}}\rangle|s_{\text{b}}, m_{s,\text{b}}\rangle|i_{\text{b}}, m_{i,\text{b}}\rangle|L, M_L\rangle \tag{1.4.37}$$

where the electronic and nuclear spins for each atom are considered separately alongside the end-over-end angular momentum, L, and its projection, M_L. Hamiltonian 1.4.36 also contains the potential term $\hat{V}(R)$ which is made up of two parts, an isotropic potential operator dependent on the molecular potential energy surface,

$\hat{V}^{\mathrm{c}}(r)$, and a magnetic dipole and spin-orbit coupling operator $\hat{V}^{\mathrm{d}}(r)$:

$$\hat{V}(R) = \hat{V}^{\mathrm{c}}(R) + \hat{V}^{\mathrm{d}}(R) \tag{1.4.38}$$

Alkali metals are ^{2}S atoms with electronic spin $s = 1/2$ and electronic orbital angular momentum $l = 0$ so we can have two possible symmetries when we combine the two spins to give us either a $^1\Sigma$ or $^3\Sigma$ state. The isotropic potential operator can then be thought of as being made of two components

$$\hat{V}^{\mathrm{c}}(R) = V_0(R)\hat{\mathcal{P}}^{(0)} + V_1(R)\hat{\mathcal{P}}^{(1)} \tag{1.4.39}$$

where $V_0(R)$ and $V_1(R)$ are the potential curves for the singlet and triplet electronic states of the pair, respectively, and $\hat{\mathcal{P}}^{(0)}$ and $\hat{\mathcal{P}}^{(1)}$ are projection operators that project onto singlet and triplet subspaces, respectively.

1.5 Photon-Dressed Basis Set and Hamiltonian

To incorporate the effects of rf radiation on a single atom, we build a basis set of photon-dressed functions in an uncoupled representation, $|s, m_s\rangle|i, m_i\rangle|N, M_N\rangle$, where N is the photon number with respect to the average photon number N_0, and M_N is the projection of the angular momentum carried by N photons. This thesis focuses primarily on circularly polarized radiation, with either $M_N = N$ (right-circularly polarized, σ_+) or $M_N = -N$ (left-circularly polarized, σ_-). The rf field is of the form

$$\boldsymbol{B}(t) = B_{\mathrm{rf}}[\hat{e}_{\mathrm{X}} \cos 2\pi\nu t \pm \hat{e}_{\mathrm{Y}} \sin 2\pi\nu t] \tag{1.5.40}$$

for σ_+ and σ_-, respectively, where $\hat{e}_{\mathrm{X}}$ and $\hat{e}_{\mathrm{Y}}$ are unit vectors along the X and Y axes. The Hamiltonian of an rf field with σ_- polarization is

$$\hat{h}_{\mathrm{rf}} = h\nu(\hat{a}_-^\dagger \hat{a}_- - N_0) \tag{1.5.41}$$

where $\hat{a}_-$ and $\hat{a}_-^\dagger$ are photon annihilation and creation operators for σ_- photons.

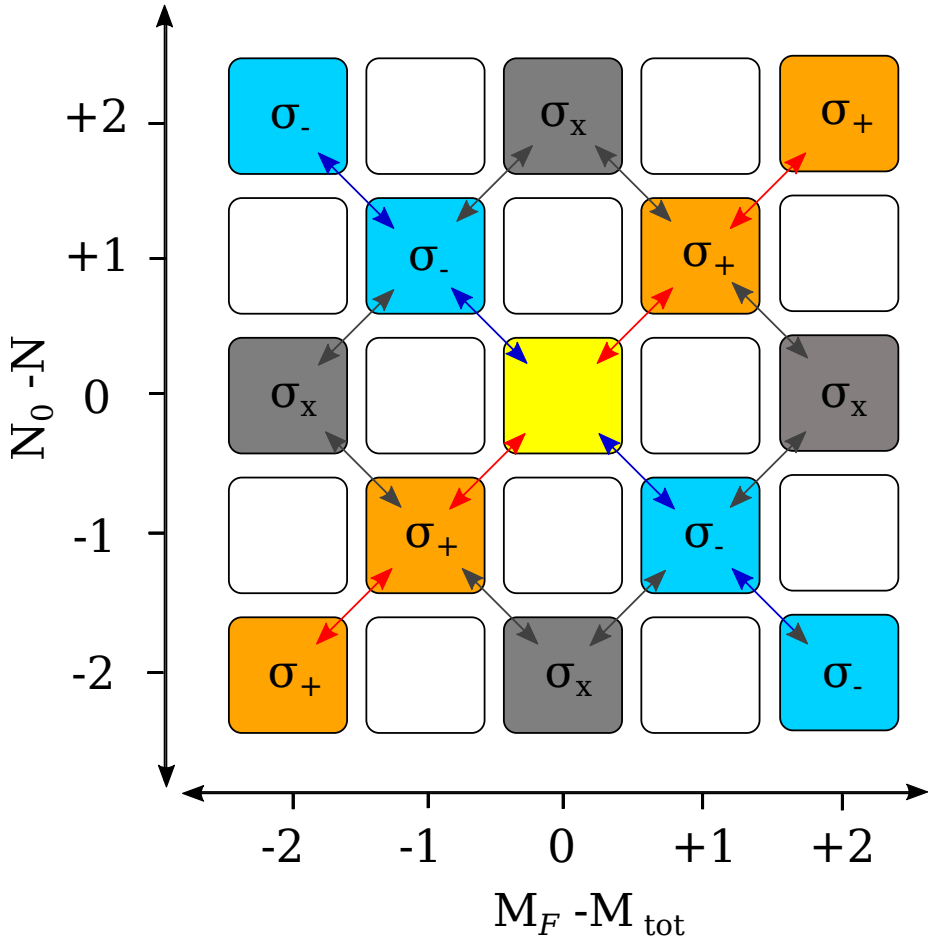

Figure 1.1: Photon-dressed basis scheme for circularly and linearly polarised rf radiation recreated from Ref. [141]. The yellow square is equivalent to the rf-free system. In $\sigma_\pm$ polarisation the system may follow the red/blue lines to the red/blue squares, whilst σ_X polarisation may follow any diagonal path including the grey arrows to the grey squares.

The interaction of the rf field with an atom is written

$$\hat{h}_{\mathrm{rf}}^{\mathrm{int}} = \frac{\mu_{\mathrm{B}} B_{\mathrm{rf}}}{2\sqrt{N_0}} \left[(g_S \hat{s}_+ + g_i \hat{i}_+)\hat{a}_-^\dagger + (g_S \hat{s}_- + g_i \hat{i}_-)\hat{a}_- \right], \tag{1.5.42}$$

where B_{rf} is the amplitude of the oscillating magnetic field, $\hat{s}_+$ and $\hat{s}_-$ are raising and lowering operators for the electron spin and $\hat{i}_+$ and $\hat{i}_-$ are the corresponding operators for the nuclear spin. For σ_+ polarization, $\hat{a}_+$ replaces $\hat{a}_-^\dagger$ and $\hat{a}_+^\dagger$ replaces $\hat{a}_-$ in Eq. (1.5.42). For σ_X radiation with rf field $\boldsymbol{B}(t) = B_{\mathrm{rf}} \cos 2\pi\nu t$, both σ_+ and σ_- coupling terms are present, renormalized by a factor of 1/2. The off-diagonal non-zero matrix elements from the rf field are given by the raising and lowering

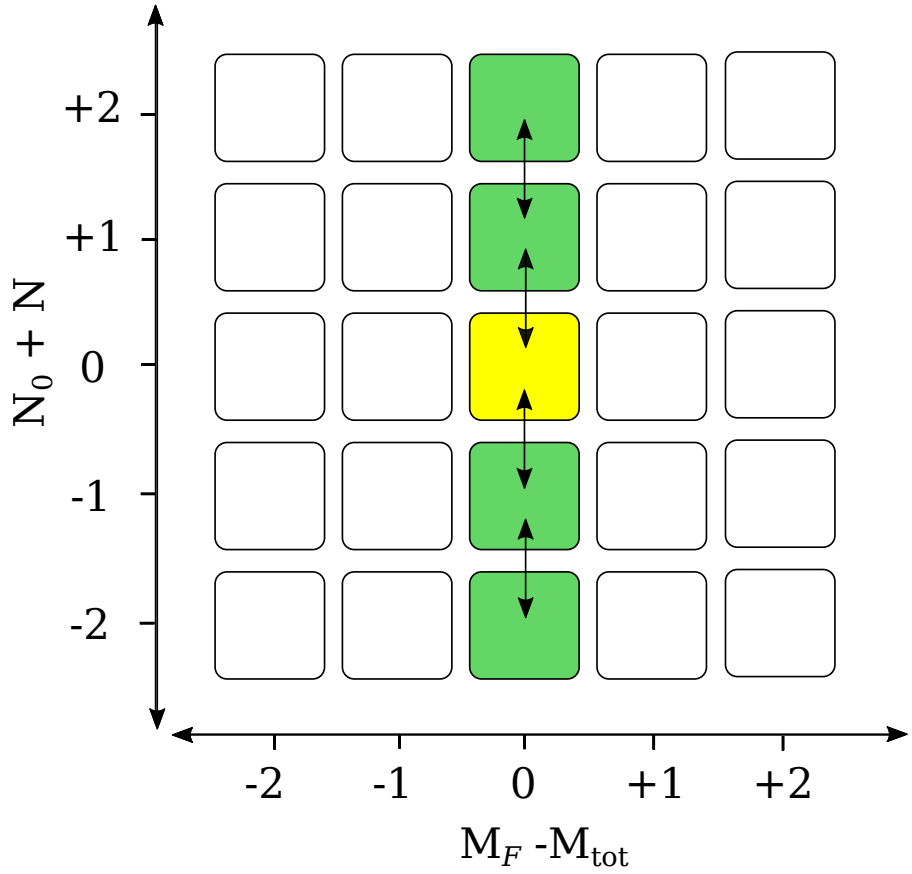

Figure 1.2: Photon-dressed basis scheme for π-polarised rf radiation. The yellow square is equivalent to the rf-free system. In π polarisation the system may follow only the verticle green arrows.

operators $\hat{s}_\pm$ and $\hat{i}_\pm$

$$\langle s, m_s \pm 1|\hat{s}_\pm|s, m_s\rangle = [s(s+1) - m_s(m_s \pm 1)]^{\frac{1}{2}} \tag{1.5.43}$$

$$\langle i, m_i \pm 1|\hat{i}_\pm|i, m_i\rangle = [i(i+1) - m_i(m_i \pm 1)]^{\frac{1}{2}} \tag{1.5.44}$$

and photon creation and annihilation operators with non-zero matrix elements

$$\langle N+1, M_N \pm 1|\hat{a}^\dagger_\pm|N, M_N\rangle = (N_0 + N + 1)^{\frac{1}{2}}; \tag{1.5.45}$$

$$\langle N-1, M_N \mp 1|\hat{a}_\pm|N, M_N\rangle = (N_0 + N)^{\frac{1}{2}}; \tag{1.5.46}$$

$$\langle N, M_N|\hat{a}^\dagger_\pm \hat{a}_\pm|N, M_N\rangle = N_0 + N. \tag{1.5.47}$$

We assume $N_0 \gg N$, so that the matrix elements of $\hat{a}^\dagger_\pm$ and $\hat{a}_\pm$ cancel with the factor $N_0^{1/2}$ in the denominator of Eq. (1.5.42). With this assumption Eq. 1.5.41 can

also be simplified to

$$\hat{h}_{\mathrm{rf}} = h\nu N \tag{1.5.48}$$

It is also worth noting that the rf radiation may be π-polarised, where the field is polarised along the z-axis and of the same form as a σ_{X} polarised field. In this case $\hat{s}_{\pm}$ and $\hat{i}_{\pm}$ in Eq. 1.5.42 are replaced with $\hat{s}_z$ and $\hat{i}_z$; a π-polarised rf field can only drive transitions between states with equal projected angular momentum.

Using Eq. 1.5.42 and knowing the matrix elements 1.5.43-1.5.46 we can visualse the rf-dressed basis set as shown in figure 1.1 which is recreated from reference [141]. The centre square represents the undressed basis set in the rf-free case and, depending on the polarisation of the rf field, one may move on a particular diagonal from the centre with σ_{X} polarisation being able to drive transitions along any diagonal. A similar diagram can be created for atoms dressed by π-polarised rf radiation, shown in Fig. 1.2, where one can only move vertically with no change in M_F.

1.6 Computer Programs

The work presented in this thesis used several programs for the different calculations required. The most used program was MOLSCAT [142], used for all scattering calculations throughout the work. The related programs BOUND and FIELD [143] were used in Chapter 2 for bound-state calculations and locating bound states as a function of magnetic field at a specified energy, respectively.

1.7 Publications Arising From This Work

- D. J. Owens, T. Xie, and J. M. Hutson, *Creating Feshbach resonances for ultracold molecule formation with radiofrequency fields*, Phys. Rev. A 94, 023619 (2016)

- D. J. Owens and J. M. Hutson, *Inelastic losses in radiofrequency-dressed traps for ultracold atoms*, Phys. Rev. A 96, 042707 (2017)

Chapter 2

Creating Feshbach Resonances for Ultracold Molecule Formation With Radio-Frequency Fields

Many of the applications of ultracold molecules mentioned in the previous chapter depend upon long-range dipole-dipole interactions. Polar molecules such as heteronuclear alkali-metal dimers are particularly attractive candidates for strong long-range interactions of this type because they tend to possess large electric dipole moments, meaning their interactions can be more easily tuned using an external electric field. Other factors influence the choice of molecule such as collisional stability; avoiding exchange reactions of the type

$$AB + AB \rightarrow A_2 + B_2$$

is an important consideration. Żuchowski *et al.* showed that many heteronuclear alkali-metal dimers are thermodynamically stable to such reactions [146], including KCs which possesses a large electric dipole moment of 1.92 Debye [147]. Potassium also has a stable fermionic isotope making ^{40}KCs one of two fermionic alkali-metal diatomic molecules (along with ^{23}Na^{40}K) stable against exchange reactions, as well as two stable bosonic isotpes (^{39}K and ^{41}K) which in total offers access to three possible isotopologues of KCs. For these reasons there has been considerable interest

in recent years in producing ultracold molecules of KCs. [67, 148, 149].

The work presented in this chapter was done in collaboration with Ting Xie, who contributed to the program used here and performed some calculations on which parts of Section 2.3 are based.

2.1 Feshbach Resonances and Magnetoassociation

Magnetoassociation has been a successful method for producing alkali-metal dimers, with the formation of ultracold ^{40}K^{87}Rb [69], ^{87}Rb^{133}Cs [61, 63], ^{23}Na^{40}K [71] and ^{23}Na^{87}Rb [150] molecules in their absolute ground states. A two-step process is required to form these molecules in their ground states; molecules are first formed in a vibrationally excited state by magnetoassociation, in which atom pairs are converted into weakly bound molecules by ramping a magnetic field across a magnetically tunable zero-energy Feshbach resonance. The resulting "Feshbach molecules" are then transferred to the polar ground state by Stimulated Raman Adiabatic Passage (STIRAP) [151], a two-photon process where the ground state is coupled to the bound state via an intermediate electronically excited state.

A Feshbach resonance [152] is an example of a scattering resonance which arises from the coupling of a bound state to the entrance channel. In particular, a Feshbach resonance occurs when a bound state of a *closed* channel is coincident in energy with the entrance channel. Another example of a scattering resonance is a shape resonance, which occurs when a bound state of the entrance channel exists at the energy of the colliding atoms behind a centrifugal barrier. If the collision energy is fixed at, or close to, the energy of the entrance channel, this kind of resonance is known as a zero-energy Feshbach resonance. Bound-state energies can be varied using an external magnetic field to create a magnetic zero-energy Feshbach resonance; the Zeeman interaction of some bound states differs from the entrance channel and so it is possible they can move across threshold. The avoided crossing formed between the threshold and bound state allows molecules to be formed adiabatically from the colliding atoms; in a Feshbach ramp [50, 51] the magnetic field starts at a magnitude greater than the resonance position and is swept down in strength across

the resonance to transfer the atoms to the molecular bound state.

Scattering properties show distinctive features in the vicinity of a resonance. For a system with a single open channel in a magnetic field, the effect of a zero-energy Feshbach resonance on the scattering length, a, can be quantified as [153, 154]

$$a(B) = a_{\mathrm{bg}}\left(1 - \frac{\Delta}{B - B_0}\right) \tag{2.1.1}$$

where the background scattering length, a_{bg}, is the scattering length outside the influence of the resonance, B is the magnetic field strength, B_0 is the resonance position in magnetic field and Δ denotes the resonance width in magnetic field. At the point where $B = B_0$ the bound state and entrance channel have equal energy and there is a pole in the scattering length. In principle this also offers some control over the interactions of colliding atoms as the magnetic field near a resonance can be varied to change the scattering length [155].

In the case of inelasticicty resulting from multiple open channels the scattering length must be complex, $a = \alpha - i\beta$. The variation of a across a Feshbach resonance in such a case is

$$a(B) = a_{\mathrm{bg}} + \frac{a_{\mathrm{res}}}{2(B - B_0)/\Gamma^B_{\mathrm{inel}} + \mathrm{i}} \tag{2.1.2}$$

where a_{res} is the resonant scattering length that is related to the strength of the resonance, and Γ^B_{inel} is a Breit-Wigner width that describes the decay of the resonant bound state to separate atoms [156]. The procedure by which MOLSCAT converges on a resonance is described in reference [157].

A major problem in producing molecules via magnetoassociation is that it is possible only if there is a Feshbach resonance of suitable width ($\geq$ 1 mG) at a magnetic field where there is a lucky combination of intraspecies and interspecies scattering lengths. Ideally, all three scattering lengths have moderate positive values to allow cooling, condensate formation and mixing of the two atomic clouds. For the intraspecies scattering lengths, negative values cause condensate collapse, whereas excessively positive values cause loss through fast 3-body recombination. For the interspecies scattering length, a large negative value can cause collapse of the mixed condensate, while a large positive value can make the condensates of the two species

immiscible. Although magnetoassociation can be carried out in low-temperature thermal gases that are not subject to condensate collapse, it is much less efficient than in condensates and does not produce high densities of molecules. This is the so-called *one-field problem*, because a single field must be chosen to satisfy several different criteria, and such a field may not (often does not) exist.

2.2 Magnetic Feshbach Resonances in ^{39}KCs

Patel *et al.* previously considered the possibilities for magnetoassociation to form molecules in mixtures of ^{39}K, ^{40}K and ^{41}K with ^{133}Cs [67] by performing coupled-channel calculations of the Feshbach resonance positions and widths, using interaction potentials obtained from extensive spectroscopic studies [158]. In all three systems, Feshbach resonances with widths suitable for magnetoassociation were identified. However, the background intraspecies and interspecies scattering lengths around the resonances present problems. In particular, the intraspecies scattering length for ^{133}Cs (see Figure 2.1) is very large and positive except in relatively narrow windows around 21 G, 559 G and 894 G [159], and for ^{39}KCs and ^{40}KCs there were no suitable interspecies Feshbach resonances that lie in these regions.

Gröbner *et al.* measured six Feshbach resonances for several spin mixtures of ^{39}K + ^{133}Cs, and the triplet interaction potential of Ref. [158] was modified to fit these observations [66]. This section presents coupled-channel calculations for ^{39}K + ^{133}Cs using the modified potential of Gröbner *et al.* Calculations were performed using the same uncoupled basis set as Patel *et al.* and Gröbner *et al.*

$$|s_{\mathrm{K}}, m_{s,\mathrm{K}}\rangle|i_{\mathrm{K}}, m_{i,\mathrm{K}}\rangle|s_{\mathrm{Cs}}, m_{s,\mathrm{Cs}}\rangle|i_{\mathrm{Cs}}, m_{i,\mathrm{Cs}}\rangle|L, M_L\rangle,$$

where s and i are the respective electronic and nuclear spins for each atom, and $m_{s/i}$ are the projections of these spins onto the quantisation axis. In a magnetic field the sum of the projections, M_{tot}, is a conserved quantity given by

$$M_{\mathrm{tot}} = m_{s,\mathrm{K}} + m_{i,\mathrm{K}} + m_{s,\mathrm{Cs}} + m_{i,\mathrm{Cs}} + M_L, \tag{2.2.3}$$

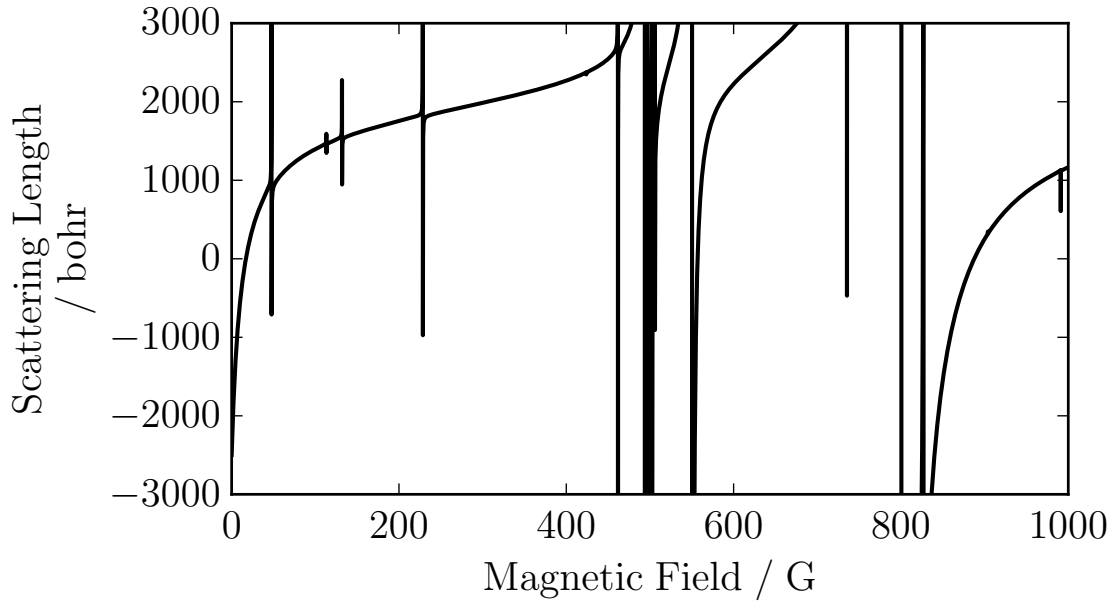

Figure 2.1: Intraspecies s-wave scattering length for caesium as a function of magnetic field with entrance channel $|f_{\mathrm{Cs}}, m_{f,\mathrm{Cs}}\rangle + |f_{\mathrm{Cs}}, m_{f,\mathrm{Cs}}\rangle = |3,3\rangle + |3,3\rangle$.

and in the case where $L = 0$, $M_{\mathrm{tot}} = M_F$ where $M_F = m_{s,\mathrm{K}} + m_{i,\mathrm{K}} + m_{s,\mathrm{Cs}} + m_{i,\mathrm{Cs}}$ is the sum of the projections of the atomic angular momentum.

The results of Gröbner *et al.* [66] were recreated, and Fig. 2.2 shows the calculated interspecies scattering length with entrance channel $|f_{\mathrm{K}}, m_{f,\mathrm{K}}\rangle + |f_{\mathrm{Cs}}, m_{f,\mathrm{Cs}}\rangle = |1,1\rangle + |3,3\rangle$, and bound-state energies relative to the lowest $M_{\mathrm{F}} = 4$ threshold, for $^{39}\mathrm{K} + ^{133}\mathrm{Cs}$ as a function of magnetic field up to 1000 G. A total of 33 bound states cross zero energy in figure 2.2 (b) below 1000 G, and Feshbach resonances identified by poles in the scattering length can be observed in the scattering length, the background value of which is approximately +64.5 bohr - ideal for magnetoassociation. The widths of these resonances vary from nG to several G (the effects of the narrowest resonances cannot be seen in figure 2.2 (a)); those over 1 mG in width, and thus suitable for magnetoassociation, are summarised in table 2.1. It can be seen that whilst resonances do exist with widths large enough for use in magnetoassociation, there are none present at the few magnetic field strengths where the intraspecies scattering length of caesium is positive and of moderate magnitude, presenting an obstacle to forming ultracold ^{39}KCs via magnetoassociation.

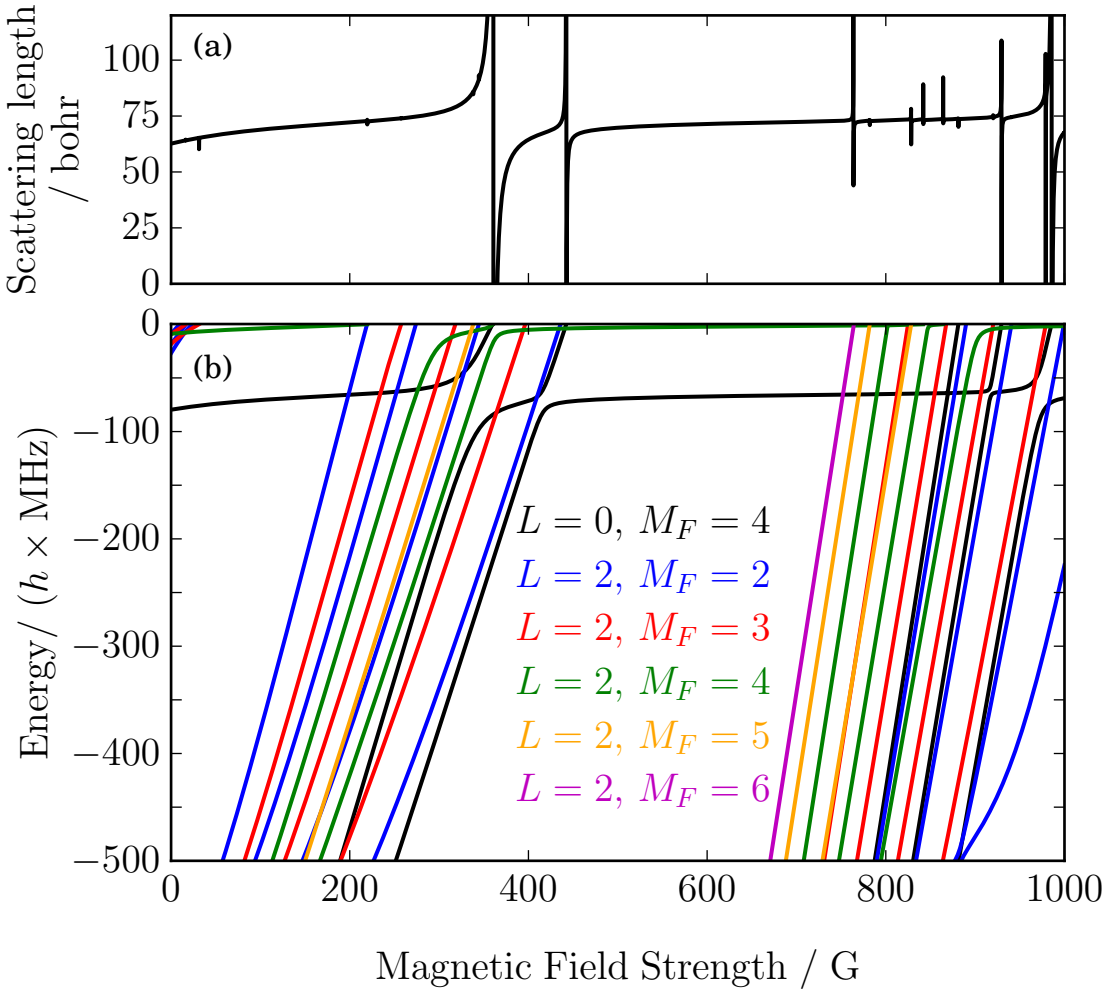

Figure 2.2: (a) Interspecies s-wave scattering length with entrance channel $|f_{\mathrm{K}}, m_{f,\mathrm{K}}\rangle + |f_{\mathrm{Cs}}, m_{f,\mathrm{Cs}}\rangle = |1,1\rangle + |3,3\rangle$, including d-wave functions.
(b) Energies of near-threshold bound states for all $M_{\mathrm{tot}} = 4$ states of ^{39}KCs with $L = 0, 2$ relative to the $|1,1\rangle + |3,3\rangle$ threshold.

2.3 rf-Induced Feshbach Resonances in ^{39}KCs

It is possible that rf fields can be used to produce new Feshbach resonances that offer additional possibilities for magnetoassociation, and may provide a solution to the one-field problem in heteronuclear systems. In particular, they may be used to produce resonances at magnetic fields where the scattering lengths have desired properties; for the magnetoassociation of ^{39}KCs it would be advantageous to create a resonance at a magnetic field where the intraspecies scattering length of caesium is of moderate magnitude. Formally similar resonances have been considered previously in homonuclear systems: Tscherbul *et al.* studied the rf-modification of magnetic

B_0 / G	Δ / G	L	M_F
359.87	0.011	2	5
360.74	4.326	0	4
442.43	0.372	0	4
763.72	0.031	2	6
828.37	0.005	2	4
841.91	0.002	2	4
864.21	0.002	0	4
929.60	0.045	0	4
978.99	0.019	2	3
985.67	1.065	0	4

Table 2.1: All calculated resonances over 1 mG in width for ^{39}KCs, including quantum numbers associated with the resonant bound state, recreated from Gröbner *et al.* [66].

Feshbach resonances and rf-induced resonances in the excited a+e channel of ^{87}Rb [160]; Hanna *et al.* looked at both rf-induced resonances and rf-dressed atomic states from an MQDT perspective in ^{6}Li, as well as the coupling of two bound states in ^{87}Rb [141]; Smith explored inducing resonances in ^{7}Li by modulating a magnetic field [161]; and Ding *et al.* investigated the modification of existing resonances in ^{87}Rb as well as inducing transitions between different hyperfine states [103]. Molecules such as $^{85}Rb_2$, ^{40}K^{87}Rb and $^{52}Cr_2$ have also been formed by direct rf association [104, 162, 163].

The coupled-channel calculations presented in this section use the decoupled basis set above, dressed with photons as described in Section 1.5

$$|s_{\mathrm{K}}, m_{s,\mathrm{K}}\rangle|i_{\mathrm{K}}, m_{i,\mathrm{K}}\rangle|s_{\mathrm{Cs}}, m_{s,\mathrm{Cs}}\rangle|i_{\mathrm{Cs}}, m_{i,\mathrm{Cs}}\rangle|L, m_L\rangle|N, M_N\rangle \tag{2.3.4}$$

The work presented in this section considers rf radiation polarised in the XY plane, specifically σ_+ (right-circularly polarised) and σ_X (plane polarised). In both these cases $M_{\mathrm{tot}} = M_F + M_L + M_N$ is a conserved quantity. The basis set used for the following calculations is also restricted to functions with $|N| \leq 2$, which we write as $N_{\mathrm{max}} = 2$, and the required M_{tot}. Figure 2.3 shows the near-threshold $L = 0$ bound states of ^{39}KCs, in the absence of rf radiation, for both $M_F = 4$, corresponding to ^{39}K and ^{133}Cs atoms in their absolute ground states, and $M_F = 3$. All levels are

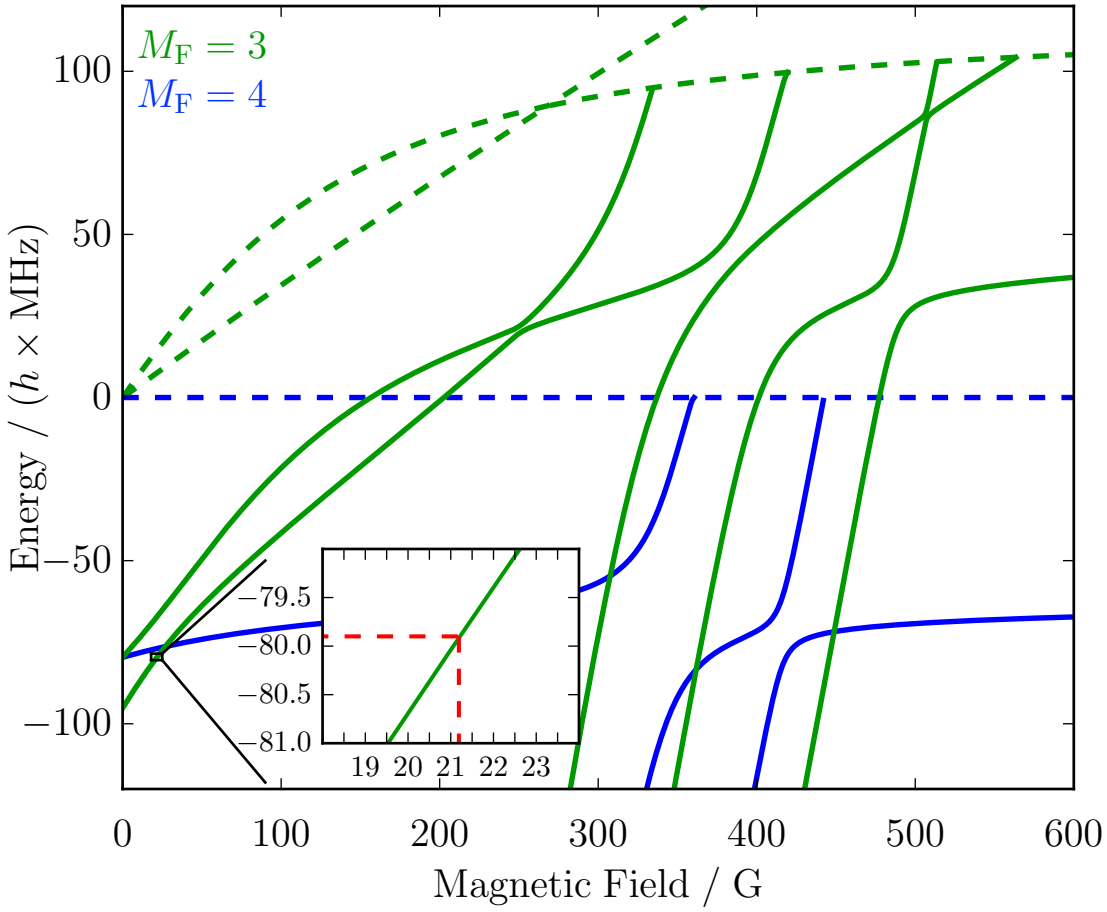

Figure 2.3: Thresholds (dashed lines) and near-threshold bound states (solid lines) for ^{39}KCs in the absence of RF radiation for $M_F = 4$ (blue) and $M_F = 3$ (green). The inset shows an expanded view of the region considered in detail. All energies are relative to the lowest $M_F = 4$ threshold.

shown relative to the lowest $M_F = 4$ threshold, and the two $M_F = 3$ thresholds, corresponding to $|f_K, m_{f,K}\rangle + |f_{Cs}, m_{f,Cs}\rangle = |1,0\rangle + |3,3\rangle$ and $|1,1\rangle + |3,2\rangle$, are shown as dashed green lines. At fields near 21 G, where the scattering length of Cs allows cooling to condensation, it may be seen that there are $M_F = 3$ bound states that lie about 67 and 80 MHz below the $M_F = 4$ threshold.

An rf frequency of 79.7 MHz is chosen to bring one of the $M_F = 3$ states into resonance with the $M_F = 4$ threshold near 21 G. We carry out scattering calculations in the field-dressed basis set for $M_{tot} = 4$ to identify Feshbach resonances. Fig. 2.4 shows the calculated interspecies scattering length for ^{39}K+^{133}Cs collisions in the region around 21 G for a variety of strengths of the rf field, B_{rf}, with σ_+ polarization and $L_{max} = 0$. It may be seen that a new resonance is induced, with a width that

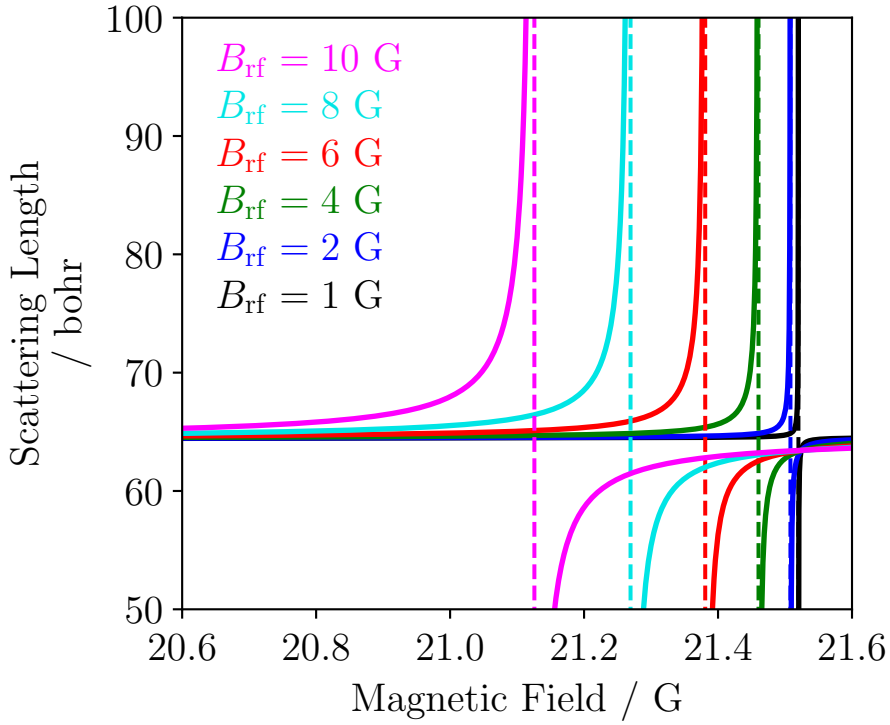

Figure 2.4: Calculated scattering length for ^{39}K+^{133}Cs, in the presence of a σ_+ rf field at a frequency of 79.7 MHz and $N_{\rm max} = 2$, with differing strengths $B_{\rm rf}$ (increasing from right to left). The dashed vertical lines indicate the position of a pole in magnetic field.

varies approximately quadratically with rf field. To a good approximation the width Δ is 6.8×10^{-5} $B_{\rm rf}^2$/G. The rf-induced resonance is also shifted significantly from its rf-free position, again nearly quadratically with field. An rf field with $B_{\rm rf} \approx 4$ G is required to induce a resonance with the required width on the mG scale needed for efficient magnetoassociation. The widths and positions for the resonances induced in Fig. 2.4 are detailed in Table 2.2.

The rf fields considered in this work are large, but comparable to those considered previously for rf frequencies of tens of MHz [141, 160]. For requencies below 10 MHz rf intensities up to a few G are typically possible, but in experiments amplitudes are limited to less than 1 G for the frequencies considered in this work [164]. However, rf fields up to 6 G with frequencies of around 20 MHz have been applied in experiments to involving ^{87}Rb on atom chips, and higher fields are achievable [107].

The resonances shown in Fig. 2.4 are lossless, so appear as true poles in the scattering length. This is because the incoming channel is the lowest that exists

$B_{\rm rf}$ / G	B_0 / G	Δ / G
1.0	21.52	6.74×10^{-5}
2.0	21.51	2.70×10^{-4}
4.0	21.46	1.08×10^{-3}
6.0	21.38	2.43×10^{-3}
8.0	21.27	4.33×10^{-3}
10.0	21.13	6.77×10^{-3}

Table 2.2: Calculated widths and positions in magnetic field for the rf-induced resonances shown in Fig. 2.4

for $M_{\rm tot} = 4$ and the molecular state that is coupled to it by rf radiation is a true bound state, below the lowest threshold. However, there are two decay mechanisms that can actually exist. First, if the rf radiation has σ_X rather than σ_+ polarization, it can couple to an $M_{\rm tot} = 4$ channel with $M_F = 3, L = 0, N = -1, M_N = 1$. Because $N = -1$, this lies below the incoming channel. The resonance is then characterized by a resonant scattering length $a_{\rm res}$ in addition to the width Δ: the real part of the scattering length exhibits an oscillation of amplitude $\pm a_{\rm res}/2$ instead of a pole, and the imaginary part exhibits a narrow peak of magnitude $a_{\rm res}$ [156]. The calculations of Fig. 2.4 were repeated for σ_X polarization, and found $a_{\rm res} = 1.6 \times 10^7 ({\rm G}/B_{\rm rf})^2$ bohr. These very large values of $a_{\rm res}$ correspond to very weakly decayed resonances, and should not cause problems in magnetoassociation. Secondly, even for σ_+ polarization, channels with $L > 0$ and $M_L \neq 0$ can cause collisionally assisted one-photon decay, mediated by the atomic spin dipolar (or second-order spin-orbit) interaction. In the present case, for example, there is a channel $M_F = 3, L = 2, M_L = 2, N = -1, M_N = -1$, and thus $M_{\rm F} + M_L = 5, M_{\rm tot} = 4$, that lies below the incoming channel. Such d-wave participation can in principle cause loss. However, this is a very weak process because of the weakness of the spin-dipolar coupling. The calculations of Fig. 2.4 were repeated with all $L = 2$ channels for $M_{\rm tot} = 4$ included; in this case the resonance is close to pole-like with $a_{\rm res} = 1.0 \times 10^7$ bohr for $B_{\rm rf} = 10$ G. Once again, therefore, this loss process should not cause problems in magnetoassociation.

The resonant scattering length $a_{\rm res}$ is given by [156]

$$a_{\rm res} = -2 a_{\rm bg} \Delta / \Gamma^B_{\rm inel}, \tag{2.3.5}$$

where $\Gamma^B_{\rm inel}$ is a Breit-Wigner width that describes decay of the field-dressed bound state to atoms. This may be converted into a lifetime for the field-dressed molecules,

$$\tau = \left| \frac{\hbar}{\Gamma^B_{\rm inel} \Delta\mu} \right| = \left| \frac{-\hbar a_{\rm res}}{2\Delta\mu a_{\rm bg} \Delta} \right|, \tag{2.3.6}$$

where $\Delta\mu$ is the difference in magnetic moments between the molecular state and the incoming channel, $\Delta\mu = \mu_{\rm molecule} - \mu_{\rm atoms}$. The value $a_{\rm res} = 1.7 \times 10^5$ bohr obtained for σ_X polarization with $B_{\rm rf} = 10$ G corresponds to a molecular lifetime of 188 ms for photon-assisted decay to the lower field-dressed threshold; the lifetime is approximately proportional to $B_{\rm rf}^{-4}$, as expected for a 2-photon decay pathway, so increases fast as the rf field is decreased. This decay of course persists only as long as the rf field is switched on.

A different type of decayed rf-induced resonance may be observed if the rf radiation couples the incoming state to a molecular state that is itself above a threshold to which it can decay. At least two such cases may be identified. Tscherbul *et al.* [160] and Hanna *et al.* [141] both considered rf-induced resonances due to bound states of $^{87}Rb_2$ near the a+e ($|1,1\rangle + |2,-1\rangle$) excited hyperfine threshold of ^{87}Rb; these bound states can decay to lower open channels with the same M_F through rf-independent mechanisms, so the resonances are strongly decayed and the molecules have a finite lifetime even after the rf field is switched off. Hanna *et al.* [141] also considered resonances due to bound states of $^6Li_2$ that lie above the lowest open channel, but have different M_F; these can decay to $L = 2$ open channels by rf-free spin-dipolar coupling, or through 2-photon rf coupling for σ_X polarization.

The coupled-channel approach adopted includes the effect of the rf field non-perturbatively. However, for the rf fields considered here, the resonance widths are clearly dominated by direct couplings from the incoming channel to the resonant bound state. Under these circumstances, the width of the resonance is proportional to the square of a bound-continuum matrix element I of the rf perturbation $\hat{h}^{\rm int}_{\rm rf} + \hat{h}_{\rm rf}$,

$$\Delta = \frac{\pi I^2}{k\Delta\mu a_{\rm bg}}, \tag{2.3.7}$$

where

$$I = \langle \psi_{\text{bound}} | \, \hat{h}_{\text{rf}}^{\text{int}} + \hat{h}_{\text{rf}} \, | \psi_{\text{incoming}} \rangle \, . \tag{2.3.8}$$

The incoming wave function is essentially a product of field-dressed atomic functions $|\alpha_{\text{K}} m_{f,\text{K}}\rangle$ and $|\alpha_{\text{Cs}} m_{f,\text{Cs}}\rangle$ and a radial function $\chi_k(r)$. At the low magnetic fields considered here, the atomic functions are approximately $|f, m_f\rangle = |1, 1\rangle$ for ^{39}K and $|3, 3\rangle$ for ^{133}Cs. The molecular wave functions are more complicated, but for the specific case of ^{39}KCs, Fig. 2.3 shows that the near-threshold bound states are mostly nearly parallel to the thresholds, indicating that they have similar spin character to the thresholds where this is true. If the scattering lengths for the $M_F = 3$ and 4 thresholds were identical, the incoming and bound-state radial functions would be orthogonal to one another, which would produce a very small matrix element I because the spin part of the rf coupling is almost independent of r. In general terms, therefore, the rf coupling is strongest for systems where the scattering lengths for the incoming and bound-state channels differ most, and thus where the singlet and triplet scattering lengths are very different. It is reasonably straightforward to construct a complete map of the near-threshold bound states for any specific system using BOUND and FIELD, but some experimentation is needed to establish which bound states produce rf-induced resonances with useful widths.

Although the resonance widths are dominated by direct couplings between the incoming channel and the resonant bound state, the shifts are not. Figure 2.5 shows the resonance positions as a function of B_{rf}^2 for both σ_+ and σ_X polarization, for basis sets with both $N_{\text{max}} = 2$ (essentially converged) and $N_{\text{max}} = 1$ (unconverged). The smaller basis sets give widths that are unchanged to 1 part in 10^3 compared to the larger ones, but the resonance positions shift substantially; they are still close to quadratic in B_{rf}, but with different coefficients. This arises because the $M_F = 3$, $N = 1$ bound state that causes the resonances is shifted by ac-Zeeman couplings to both $N = 0$ and $N = 2$ states, but the latter couplings are omitted for the smaller basis sets. The shifts are also significantly different for the two polarizations. The coupled-channel approach used here provides a straightforward way to capture such effects properly.

Resonances of the type described here will exist for all the alkali-metal dimers.

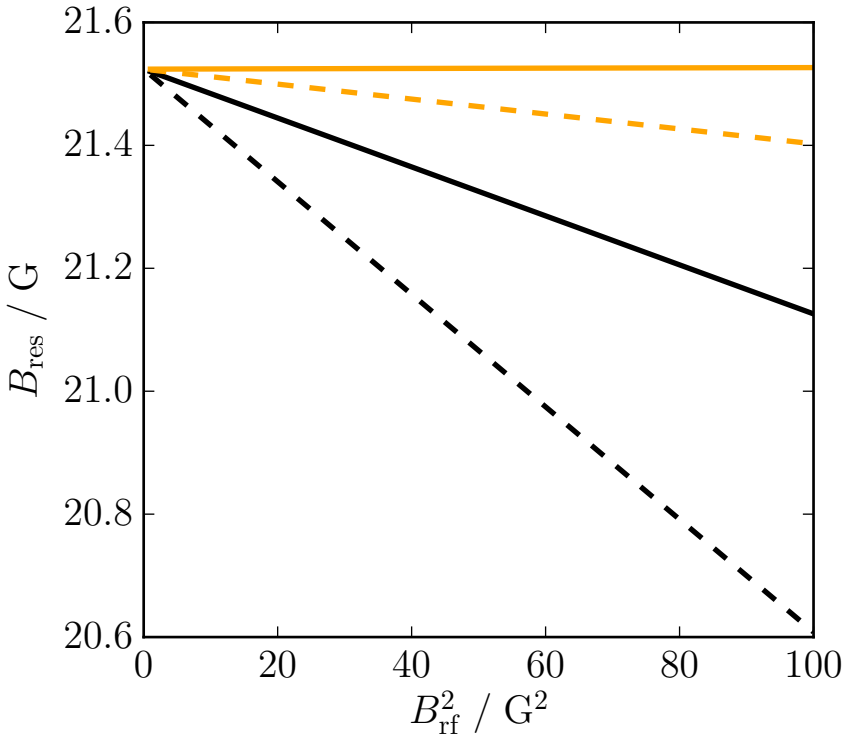

Figure 2.5: Calculated resonance positions as a function of B_{rf}^2 for σ_+ (black lines) and σ_X polarization (orange lines), for basis sets with $N_{\mathrm{max}} = 1$ (dashed lines) and $N_{\mathrm{max}} = 2$ (solid lines).

For all such dimers except those containing ^{40}K, the lowest threshold in a magnetic field has $M_{F,\mathrm{ground}} = i_a + i_b - 1$. For those containing ^{40}K, which has inverted hyperfine structure, $M_{F,\mathrm{ground}} = i_a + i_b$. In both cases, there are Zeeman-excited thresholds with $M_F < M_{F,\mathrm{ground}}$. However, the lowest thresholds with $M_F > M_{F,\mathrm{ground}}$ always correlate with excited hyperfine states and are substantially higher in energy. As for ^{39}KCs, resonances due to bound states with $M_F = M_{F,\mathrm{ground}} - 1$ are likely to be pole-like, with only weak decay as described above.

2.4 Conclusions

In this chapter it has been shown that radio-frequency fields can be used to engineer magnetically tunable Feshbach resonances in regions of magnetic field where they did not previously exist. This capability may allow the creation of resonances at magnetic fields where the intraspecies and interspecies scattering lengths have

values that are favorable for evaporative or sympathetic cooling, and where stable mixed condensates may be created. This in turn may allow magnetoassociation to form molecules from otherwise intractable pairs of ultracold atoms. The resonances considered are different from those of refs. [160], [141] and [103] both because the molecules that can be created at them are heteronuclear and because they are truly bound, so cannot decay to lower atomic thresholds after the rf radiation is switched off.

This chapter describes using an rf field to bring bring bound states into resonance with a threshold to create new Feshbach resonances. This is conceptually the simplest approach, but a similar effect could be achieved with the difference between two laser frequencies, with different (and potentially more versatile) selection rules governing which bound states can cause resonances.

Chapter 3

Inelastic Losses in Radio-frequency Dressed Magnetic Traps

Radio-frequency-dressed magnetic traps confine ultracold atoms in adiabatic potentials [116]. Since the technique was first proposed in 2001 [114] and experimentally realised in 2004 with atoms of ^{87}Rb [115], it has been used to create novel geometries such as shells [117] and rings [119–121]. The advantages of rf-dressing include low heating rates and smooth trapping potentials that can be easily altered by adjusting the parameters of the rf field. The technique has found uses in atom interferometry [122, 165–167] and as a way to modify interactions between lattice sites in optical potentials [127, 168, 169].

There are various sources of atom loss in rf-dressed traps. The rf-dressed state that is adiabatically trapped is not the lowest in energy that exists and so non-adiabatic loss mechanisms are an important consideration. Non-adiabatic one-body losses have been analysed previously [115, 119, 170], and such losses may be made acceptably small by avoiding very low rf coupling strengths.

Additional loss mechanisms exist beyond the one-body case. In an inelastic collision pairs of atoms collide and release kinetic energy if there is a lower energy state available, and the recoil can eject them from the trap. The rate coefficient for this two-body loss, k_2, is proportional to the imaginary part of the complex

scattering length, β, and is given by

$$k_2 = \frac{2hg_\alpha\beta}{\mu} \tag{3.0.1}$$

in the limit that $E \to 0$, where μ is the reduced mass and g_α is a symmetry factor equal to 2 for identical bosons and 1 for all other cases [153]. The rate of loss for a two-body collision is described by a second order rate equation given by

$$r = k_2\rho_{\mathrm{A}}\rho_{\mathrm{B}} \tag{3.0.2}$$

where $\rho_{\mathrm{A/B}}$ is the density of species A/B.

3.1 Radio-frequency Dressed Magnetic Traps

In an rf-dressed magnetic trap atoms are trapped using a combination of magnetic and rf fields, and are confined in an adiabatic potential obtained by diagonalizing a Hamiltonian in a basis set of rf-dressed atomic states. The uncoupled atomic basis set is written

$$|s, m_s\rangle|i, m_i\rangle|N, M_N\rangle. \tag{3.1.3}$$

To describe an rf-dressed trap for an $f = 1$ atom requires $N_{\max} = 1$, and in the absence of the couplings involving the photon annihilation and creation operators (Eq 1.5.42), states with different values of m_f and different N cross as a function of magnetic field at a point B_0. These states cross when the Zeeman splitting is equal to the rf photon energy, so B_0 can be estimated using the frequency of the rf field, ν, and the Landé g-factor, g_f, of the atom

$$B_0 = \frac{\nu\hbar}{|g_f|\mu_{\mathrm{B}}} \tag{3.1.4}$$

For ^{87}Rb, with $s = 1/2$, $i = 3/2$, and 3.0 MHz radiation, the $(f, m_f, N) = (1, +1, 1)$, $(1, 0, 0)$ and $(1, -1, -1)$ states all cross near $B = 4.27$ G, as shown in Fig. 3.1. If the radiation has σ_- polarization, these three states all have the same total projection quantum number $M_{\mathrm{tot}}^{\mathrm{atom}} = m_s + m_i + M_N$; each σ_- polarised photon carries an

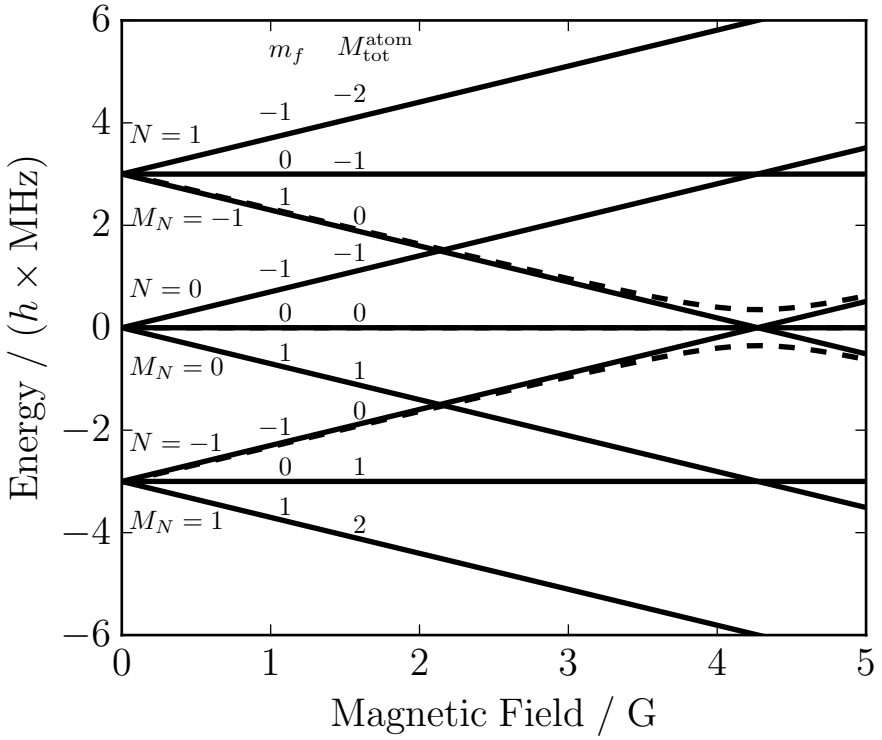

Figure 3.1: rf-dressed atomic levels of $f = 1$ states of ^{87}Rb for frequency 3.0 MHz and photon numbers $N = -1$, 0 and 1, shown with respect to the energy of the $f = 1$, $m_f = 0$ state for $N = 0$. Solid lines show levels for zero rf intensity and dashed curves show levels for $B_{\rm rf} = 0.5\,$G with σ_- polarisation and $M_{\rm tot}^{\rm atom} = 0$. Atoms can be trapped at the minimum in the upper dashed curve.

angular momentum projection of -1 so the relevant states can now be written as $(f, m_f, N, M_N) = (1, +1, 1, -1)$, $(1, 0, 0, 0)$ and $(1, -1, -1, 1)$, each giving $M_{\rm tot}^{\rm atom} = 0$. These states are then coupled by the interaction 1.5.42, so the triple crossing becomes a three-way avoided crossing. For $B_{\rm rf} = 0.5$ G the minimum separation between the states, ΔE, is $h \times 0.35$ MHz, which is given by

$$\Delta E = B_{\rm rf} |g_f| \mu_{\rm B} \tag{3.1.5}$$

Ultracold atoms in the uppermost state can be trapped in the vicinity of the avoided crossing. These atoms are in a state whose character is principally $(f, m_f, N) = (1, +1, 1)$ on the low-field side of the crossing, but is $(1, -1, -1)$ on the high-field side and a complicated superposition of all three states close to the crossing itself.

To describe an rf-dressed magnetic trap for a *pair* of $f = 1$ atoms, photon

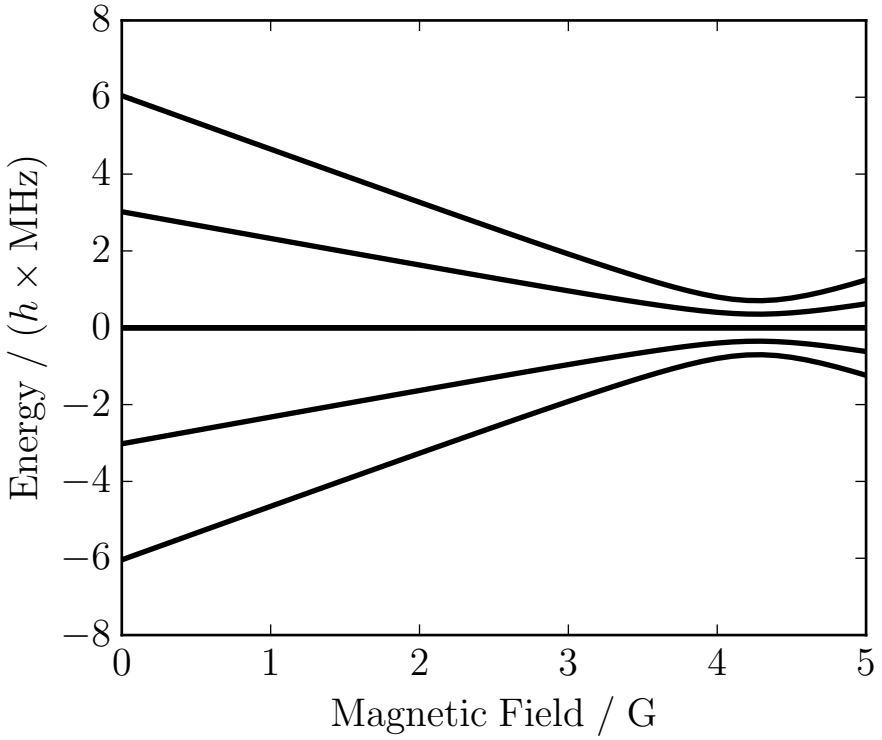

Figure 3.2: The rf-dressed atomic thresholds of ^{87}Rb+^{87}Rb for $f = 1$ and $M_{\rm tot} = 0$. The rf-induced collisions that cause trap loss are from the uppermost of these thresholds to all the lower ones. The thresholds are calculated for $\nu = 3.0$ MHz and $B_{\rm rf} = 0.5$ G with σ_- polarisation. Near zero magnetic field the thresholds can be labelled from top to bottom as $M_F = 2, 1, 0, -1, -2$ built from atomic states $(m_{f,1}, m_{f,2}) = (1,1), (1,0), (-1,+1) + (0,0), (-1,0), (-1,-1)$, with $N = 2, 1, 0, -1, -2$, respectively.

numbers N from -2 to 2 are required. For the rf field parameters described above, this produces atomic collision thresholds as shown for ^{87}Rb+^{87}Rb in Fig. 3.2. Pairs of atoms are trapped at the highest of the 6 thresholds shown which can be labelled with $M_F = m_{f,1} + m_{f,2} = 2$ on the low-field side of the avoided crossings, and can undergo inelastic collisions to produce atoms at the lower thresholds. Such inelastic collisions release kinetic energy of at least $h \times 0.25$ MHz $\approx k_{\rm B} \times 12.5$ μK, and the recoil will usually eject both collision partners from the trap. The rate coefficient for this inelastic loss is given by Eq. 3.0.1 in the limit $E \to 0$, but a more general expression for the loss rate in the s-wave regime is given by [171]

$$k_2(E,B) = \frac{2hg_\alpha \beta(E,B)}{\mu\left[1 + k^2|a(E,B)|^2 + 2k\beta(E,B)\right]}, \tag{3.1.6}$$

where k is the wavevector for the collision, and α and β are the real and imaginary parts of the scattering length, respectively. Resonant peaks are moderated by the $k^2|a|^2$ term in the denominator at the collision energy of $1\,\mu\mathrm{K} \times k_\mathrm{B}$ used in the following calculations.

3.2 Inelastic Collisions of Alkali Metal Atoms in rf-Dressed Magnetic Traps

This section presents the results of coupled-channel scattering calculations for rf-dressed states of alkali-metals ^{87}Rb, ^{85}Rb and ^{39}K. Since ^{87}Rb is a special case with highly atypical scattering properties, collisions of the more typical ^{39}K are first considered. Both ^{87}Rb and ^{39}K possess nuclear spin $i = 3/2$ and consequently have the same hyperfine ground state $f = 1$. Collisions of these atoms in their upper hyperfine state $f = 2$ are then considered and contrasted with ^{85}Rb which has nuclear spin $i = 5/2$ and therefore ground state and upper hyperfine states $f = 2$ and $f = 3$, respectively. Heteronuclear collisions are also considered by studying rf-dressed ^{87}Rb+^{85}Rb. Unless otherwise stated the rf field parameters are $\nu = 3.0$ MHz and $B_\mathrm{rf} = 0.5$ G with σ_- polarisation.

3.2.1 Inelastic collisions of rf-dressed ^{39}K

The rf-dressed thresholds for ^{39}K+^{39}K are similar to those for a pair of ^{87}Rb atoms (Fig. 3.2), but the centre of the trap is shifted slightly upfield to 4.33 G because of the smaller Landé g-factor of ^{39}K. The inelastic collision rates are shown in Fig. 3.3(a), as a function of magnetic field across the trap. The solid line shows the inelastic rate from calculations with $L_\mathrm{max} = 2$, while the dashed line shows the rate from simplified (and computationally far cheaper) calculations with $L_\mathrm{max} = 0$. Both calculations use photon numbers $-2 \leq N \leq 2$; adding additional values of N makes no further difference to the results as any new dressed thresholds introduced from the ground state hyperfine manifold cannot have $M_\mathrm{tot} = 0$ and are therefore not coupled.

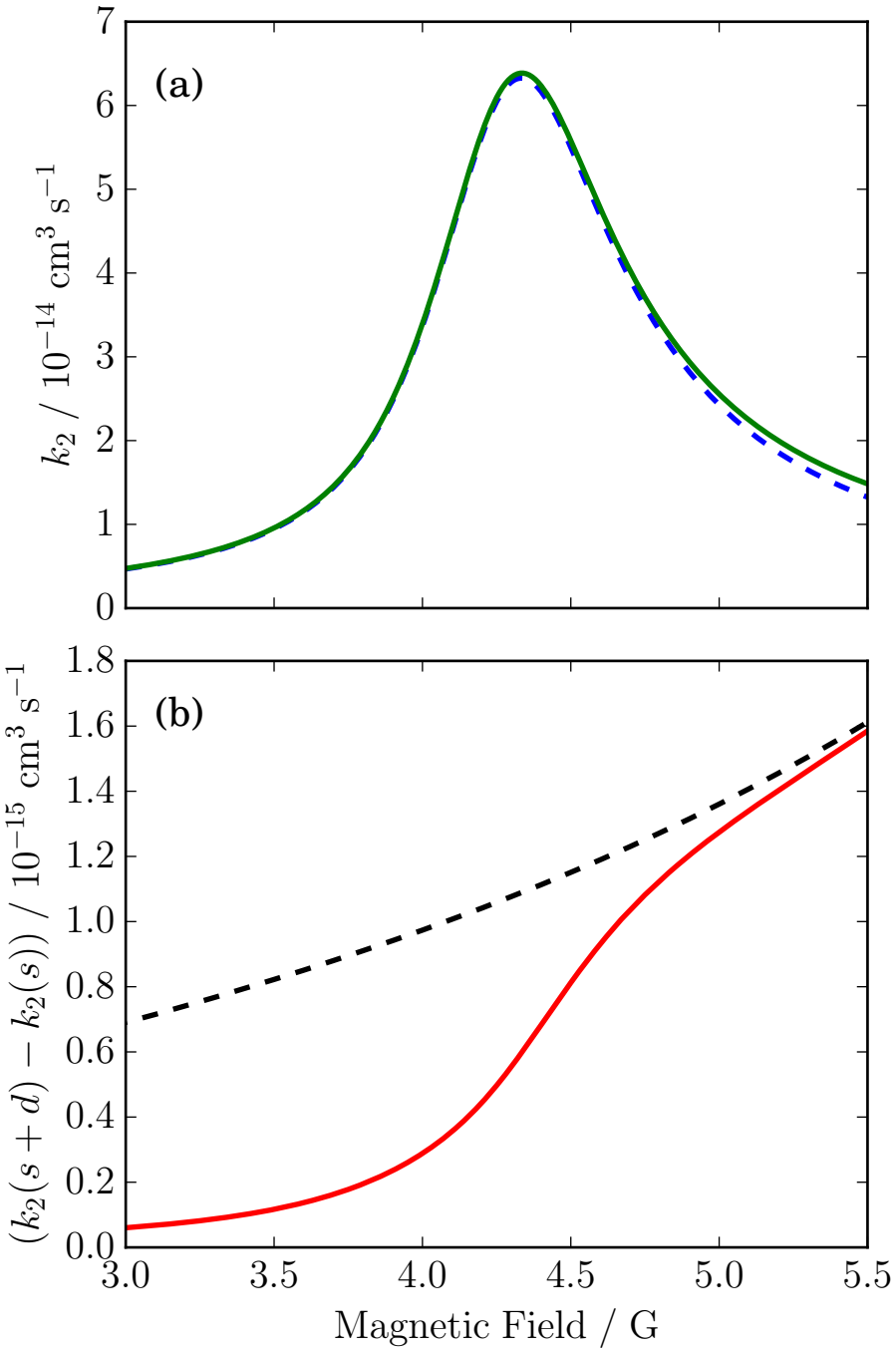

Figure 3.3: (a) Rate coefficient for inelastic loss of adiabatically trapped ^{39}K+^{39}K as a function of magnetic field, from calculations with $L_{\max} = 2$ (solid, green) and $L_{\max} = 0$ (dashed, blue). (b) Contribution from rf-modified spin-relaxation collisions, obtained from the difference between the $L_{\max} = 0$ and $L_{\max} = 2$ results (red, solid) compared with rf-free spin-relaxation for $(f, m_f) = (1, -1)$ atoms (black, dashed).

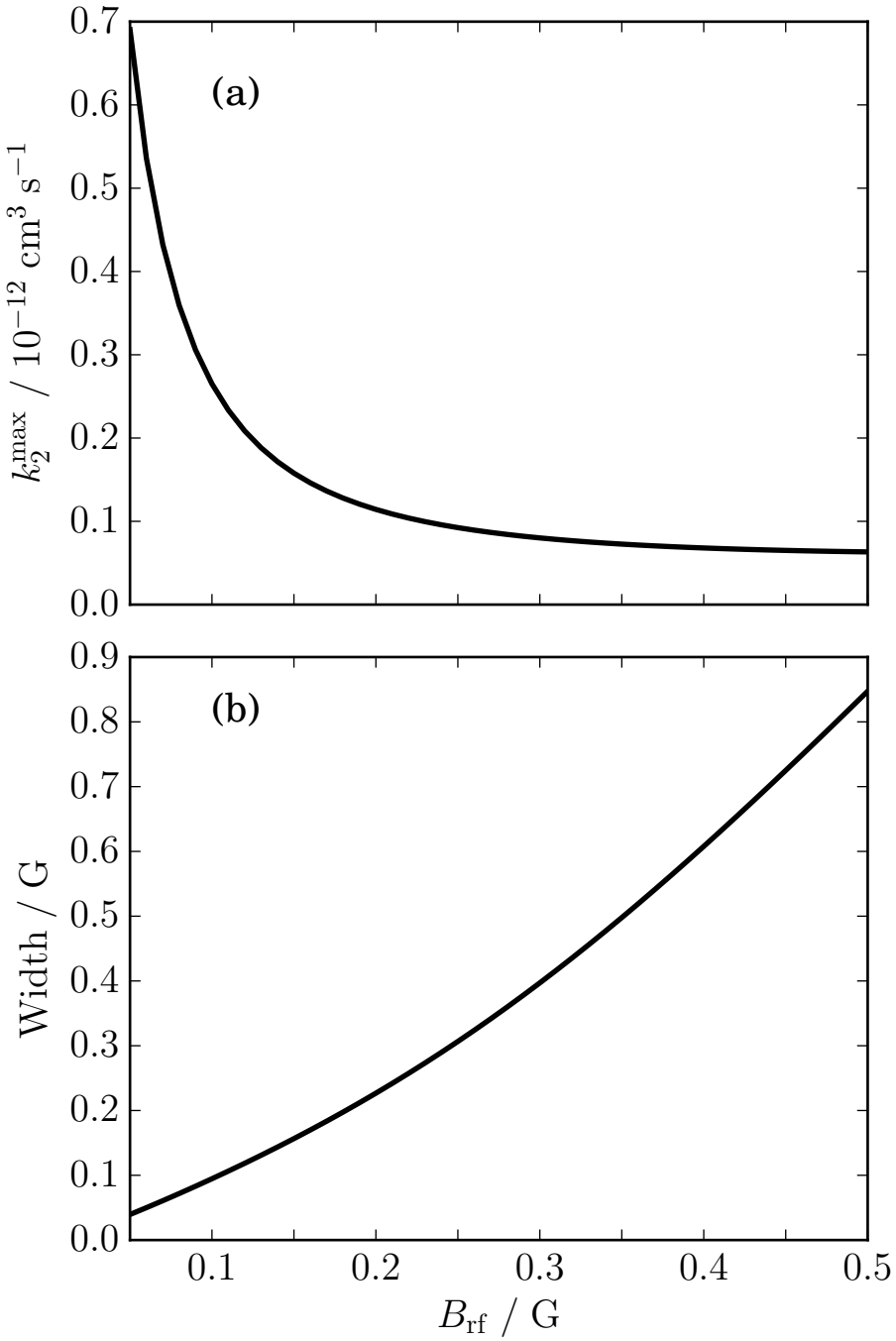

Figure 3.4: Height and FWHM width of the peak in inelastic rate coefficient for ^{39}K+^{39}K, as a function of rf amplitude $B_{\rm rf}$.

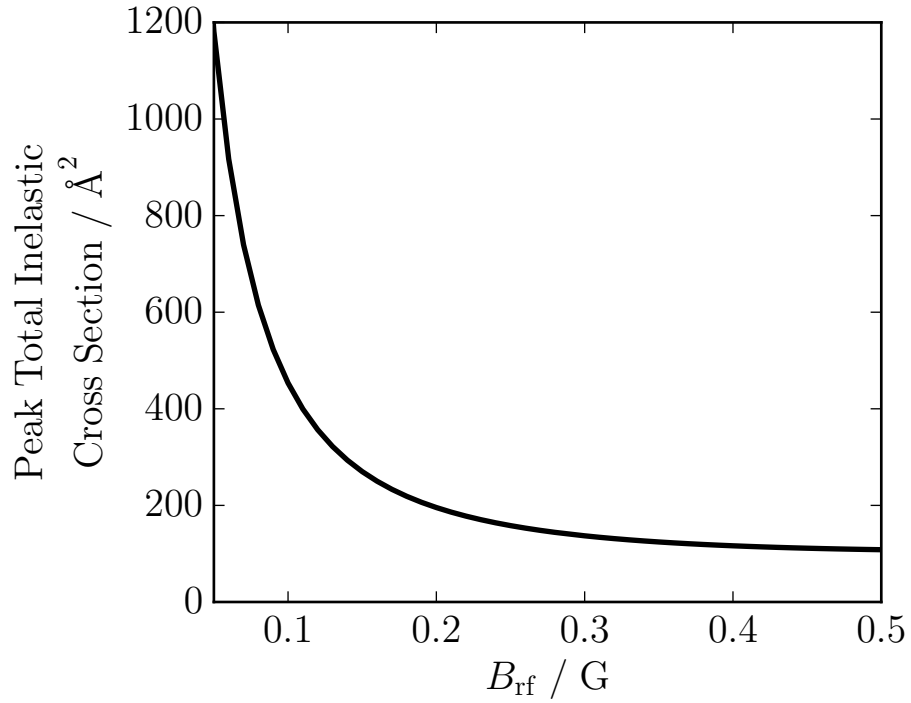

Figure 3.5: Peak total inelastic cross sections for ^{39}K + ^{39}K as a function of rf amplitude $B_{\rm rf}$.

The main source of inelasticity in ^{39}K+^{39}K collision exists even for $L_{\rm max} = 0$. It arises from collisions that conserve $m_{f1} + m_{f2} + M_N$ and thus do not change M_L; these will be referred to as rf-induced collisions. Since L does not need to change, there is no centrifugal barrier in the outgoing channel and no centrifugal suppression of the inelastic rate. For $B_{\rm rf} = 0.5\,$G, the loss rate peaks at $k_2^{\rm max} = 6.33 \times 10^{-14}$ cm^3 s^{-1} ($\beta = 0.015$ bohr) near the trap center and dies off on either side. However, the peak is a strong function of $B_{\rm rf}$. Figure 3.4 shows the height $k_2^{\rm max}$ and full width at half maximum (FWHM) of the peak as a function of $B_{\rm rf}$, obtained from calculations with $L_{\rm max} = 0$; the peak width increases as $B_{\rm rf}$ increases, but the peak height decreases. While the width of these rf-induced features decreases steadily towards 0 G, the height increases to a maximum of around 4×10^{-12} cm^3 s^{-1} with $B_{\rm rf}$ of the order of 10^{-7} G, and falls off. The width increases faster than linearly with $B_{\rm rf}$; although the range of B across which the atomic states are strongly mixed by rf dressing is linear in $B_{\rm rf}$, the kinetic energy released is proportional to $B_{\rm rf}$ and this affects the inelastic cross sections. The peak total inelastic cross section decreases as with $B_{\rm rf}$, and is shown in Fig. 3.5.

For ^{39}K+^{39}K, the inelastic rates are fairly similar for $L_{\max} = 2$ and $L_{\max} = 0$. The small difference arises because, even in the absence of rf radiation, atoms in $f = 1, m_f < 1$ may undergo spin-relaxation collisions to produce atoms in lower magnetic sublevels. Such collisions are driven only by the weak anisotropic part of the interaction, $V^{\mathrm{d}}(R)$ in Eq. (1.4.38). Since they change $M_F = m_{f1} + m_{f2}$, and $M_F + M_L$ must be conserved, they must also change M_L. For s-wave collisions, L is initially zero, so changing M_L requires a final state with $L > 0$, which must have $L \geq 2$ to conserve parity. The rates of spin-relaxation collisions are therefore suppressed because the products are trapped inside an $L = 2$ centrifugal barrier, which has height $k_{\mathrm{B}} \times 1.5$ mK for ^{39}K+^{39}K. Figure 3.3(b) shows the *difference* between the $L_{\max} = 2$ and $L_{\max} = 0$ results in Fig. 3.3(a) and compares it with the rate of spin-relaxation collisions from an rf-free calculation for two atoms initially in the $(f, m_f) = (1, -1)$ state. It may be seen that the difference approaches the rf-free spin-relaxation rate at high magnetic field, where the adiabatically trapped state is principally $(1, -1)$. However, it decreases to zero at low magnetic field, where the trapped state is principally $(1, 1)$, which is the rf-free ground state and cannot undergo inelastic collisions. At the trap center the rf-modified spin-relaxation rate is about half its rf-free value.

The effects of linearly polarised σ_{x} rf radiation were also investigated. M_{tot} is still conserved but each photon may carry angular momentum $M_N = \pm 1$ since σ_{x} polarisation is a linear comibination of σ_- and σ_+ circularly polarisations. A renormalisation factor of $1/2$ result in the rf matrix elements with a linearly polarised rf field of amplitude $B_{\mathrm{rf,x}}$ being equal to the rf matrix elements of a circularly polarised rf field of amplitude $B_{\mathrm{rf,x}}/2$. This translates into near-identical loss rate coefficients, illustrated in Fig. 3.6 with a σ_{x} polarised rf field with $B_{\mathrm{rf}} = 0.5$ G and a σ_- polarised rf field with $B_{\mathrm{rf}} = 0.25$ G. The peak difference is approximately 1 part in 1000 with respect to $k_2^{\max}$ (9.24×10^{-14} cm^3 s^{-1}) for σ_- polarisation with $B_{\mathrm{rf}} = 0.25$ G. These differences arise from slight shifts in collision thresholds due to extra states included as a result of the σ_+ component of the linearly polarised field.

Because perfect alignment of rf and static magnetic fields can be difficult to achieve experimentally, arbitrary angles between the rf and magnetic fields were

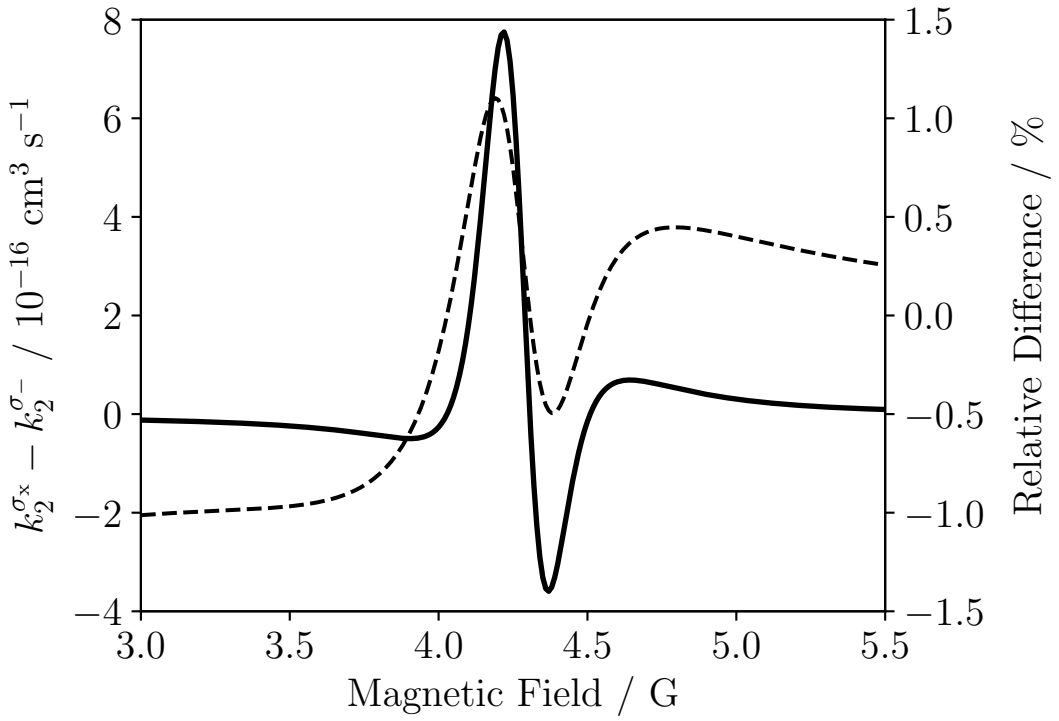

Figure 3.6: Difference in rf-induced loss between a linearly polarised rf field with $B_{\mathrm{rf}} = 0.5$ G and a circularly polarised rf field with $B_{\mathrm{rf}} = 0.25$ G for ^{39}K + ^{39}K. The left vertical axis shows the absolute difference indicated by the solid line, while the right vertical axis shows the difference as a percentage relative to the loss in the circularly polarised rf field shown by the dashed line.

also considered. In the case of non-perpendicular (or non-parallel) rf and magnetic fields M_{tot} is no longer conserved as orthogonality between axes other than the quantisation axis is no longer present. Within the structure of MOLSCAT this is achieved by tilting the magnetic field by an angle θ from the Z-axis towards the rf-field which is chosen to lie along the X-axis. Where previously the Hamiltonian was diagonal in M_{tot} with Zeeman matrix elements given by Eq. 1.4.35, we now have off-diagonal elements from the X-axis component of the magnetic field. The matrix elements for the tilted magnetic field are

$$\langle i\, m_i, s\, m_s | B_{\mathrm{Z}} \mu_{\mathrm{B}} (g_n \hat{i}_z + g_s \hat{s}_z) | i\, m_i, s\, m_s \rangle \tag{3.2.7}$$

$$\langle i\, m_i, s\, m_s | B_{\mathrm{X}} \mu_{\mathrm{B}} (g_n \hat{i}_\pm + g_s \hat{s}_\pm) | i\, m_i \pm 1, s\, m_s \pm 1 \rangle \tag{3.2.8}$$

respectively, where $B_{\mathrm{X}} = B \sin\theta$ and $B_{\mathrm{Z}} = B \cos\theta$. Because M_{tot} is not conserved, every possible m_f for each photon number must be included in the calculation. This

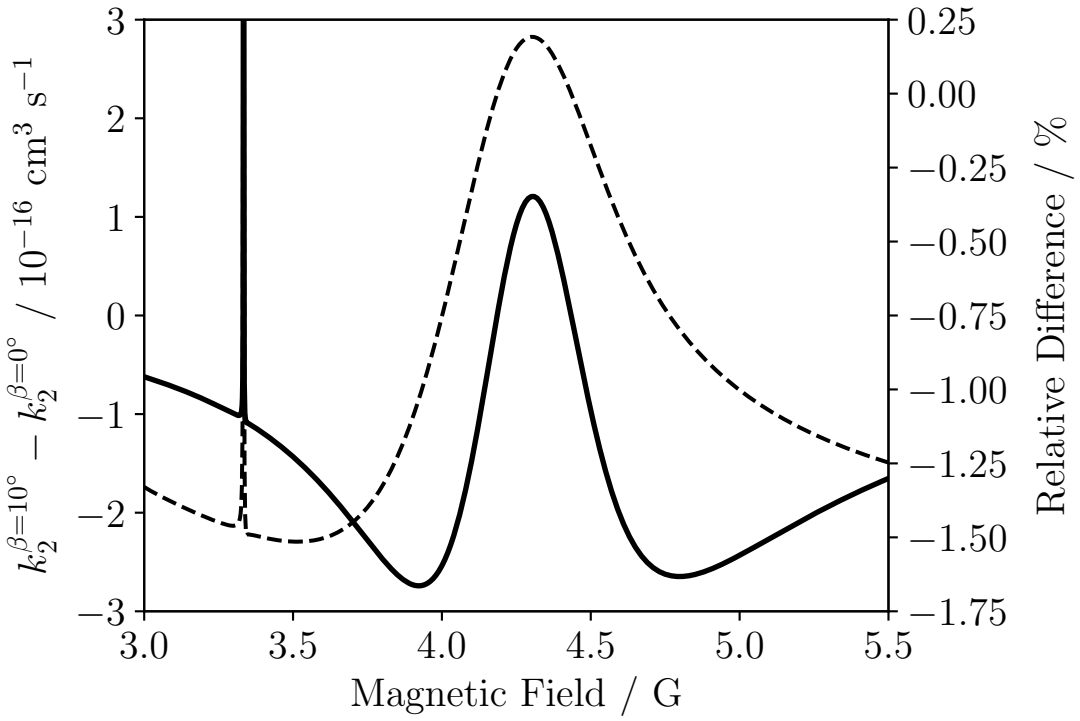

Figure 3.7: Difference in the rf-induced loss between $\theta = 10°$ and $\theta = 0°$ calculations for ^{39}K+^{39}K with all rf field parameters the same as Fig. 3.3. The left vertical axis shows the absolute difference indicated by the solid line, while the right vertical axis shows the difference as a percentage relative to the loss in the $\theta = 0°$ case shown by the dashed line.

increases the number of open channels from 6 to 26 here and significantly impacts the required computer time to complete a calculation. Fig. 3.7 shows the difference in k_2 between the calculation with $L_{\max} = 0$ and $\theta = 0°$ shown in Fig. 3.3 and a calculation with $\theta = 10°$. There is a difference of 1.20×10^{-16} cm^3 s^{-1} at the trap centre and a difference of around 2.75×10^{-16} cm^3 s^{-1} either side of the trap centre, less than 1 part in 200 with respect to $k_2^{\max} = 6.33 \times 10^{-14}$ cm^3 s^{-1} shown in Fig. 3.3. These differences are due to the slight shift in collision thresholds caused by the additional avoided crossings introduced by the extra m_F states. There is also a very sharp feature around 3.3 G caused by an avoided crossing between states which correspond to $(m_{f,1}, m_{f,2}, N) = (-1, -1, -1)$ and $(1, 1, 2)$ at low magnetic field. The small difference of 0.5% between the $\theta = 0°$ and $\theta = 10°$ calculations combined with the impact on computer time leads us to conclude that calculations with $\theta = 0°$ are sufficient to understand the rf-induced loss in a system.

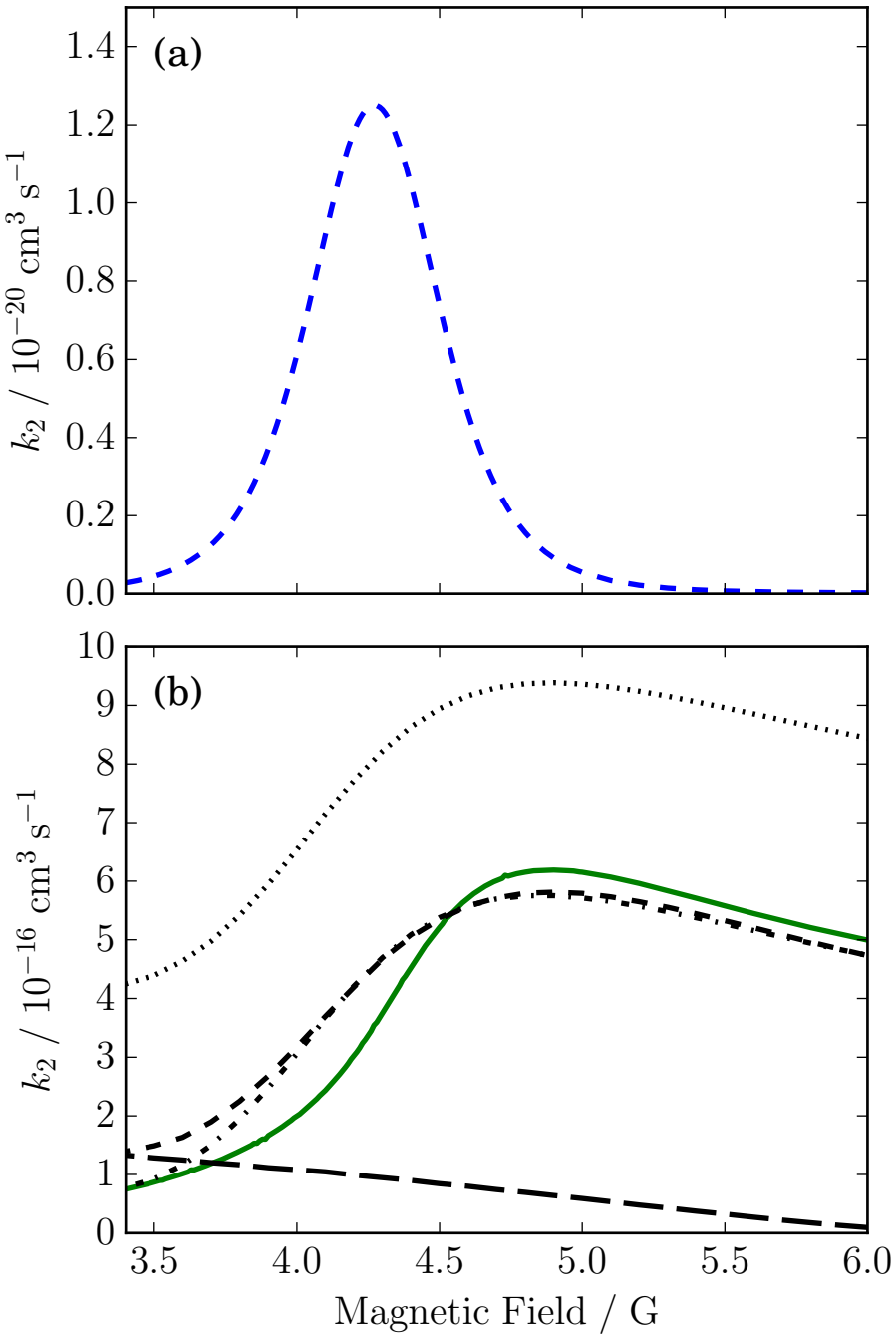

Figure 3.8: Rate coefficient for inelastic loss for adiabatically trapped ^{87}Rb in $f = 1$ as a function of magnetic field with $\nu = 3.0$ MHz, $B_{\mathrm{rf}} = 0.5$ G and σ_- polarisation. (a) Calculation using $L_{\mathrm{max}} = 0$. (b) Calculation including spin relaxation, using $L_{\mathrm{max}} = 2$ (solid green line). Rate coefficients for rf-free spin relaxation are shown as dashed lines for $(1,-1)$+$(1,-1)$, dashed-dotted lines for $(1,-1)$+$(1,0)$, dotted lines for$(1,0)$+$(1,0)$ and long dashed lines for $(1,0)$+$(1,1)$.

3.2.2 Inelastic collisions of rf-dressed ^{87}Rb

Figure 3.8 shows the calculated inelastic rate constant as a function of magnetic field for ^{87}Rb. Figures 3.8(a) and 3.8(b) show calculations with $L_{\max} = 0$ and 2, respectively. In this case the rate coefficient for rf-induced loss (with $L_{\max} = 0$) reaches a maximum of only $k_2^{\max} = 1.25 \times 10^{-20}$ cm^3 s^{-1} ($\beta = 6.47 \times 10^{-8}$ bohr) at $B = 4.2713$ G (the trap center). This is more than 6 orders of magnitude slower than for $^{39}K_2$, and 4 orders of magnitude lower than the rf-modified spin-relaxation rate at the trap center. Consequently Fig. 3.8(b) is totally dominated by spin relaxation. In this case, however, the spin relaxation itself shows more complicated structure as a function of B; the dashed lines in Fig. 3.3(b) show the rf-free spin relaxation rates for $(1,1)+(1,1)$, $(1,1)+(1,0)$, $(1,1)+(1,-1)$ and $(1,0)+(1,-1)$ collisions. As with ^{39}K, the losses for rf-dressed states approach those for rf-free $(1,1)+(1,1)$ at high magnetic field, but around the trap centre there are also contributions from other components of the wavefunction of the rf-dressed atomic states.

The rf-induced loss rate depends strongly on the singlet and triplet scattering lengths $a_{\rm s}$ and $a_{\rm t}$. In order to explore this, calculations were carried out with $L_{\max} = 0$ on a set of potentials modified at short range to allow adjustment of $a_{\rm s}$ and $a_{\rm t}$. The functional forms of the potential curves of Strauss *et al.* [172] were retained, but the short-range matching point, $R_{\rm SR}$, was changed to 3.5 Å for the singlet potential and to 5.6 Å for the triplet potential in order to provide sufficient flexibility to adjust the scattering lengths through a complete cycle from $+\infty$ to $-\infty$. The short-range power $N_{\rm SR}$ was then adjusted to obtain modified potentials with different scattering lengths, maintaining continuity of the potential and its derivative at $R_{\rm SR}$ as described in ref. [66]. Fig. 3.9 shows the variation of $a_{\rm s}$ and $a_{\rm t}$ as a function of $N_{\rm SR}$.

Contour plots of the resulting rf-induced peak loss rates $k_2^{\max}$ and the corresponding real part of the scattering length $a_{\rm rf}$ (for collisions of rf-dressed atoms) are shown in Figure 3.11, calculated at the trap center. Since the possible singlet and triplet scattering lengths range from $-\infty$ to $+\infty$, the loss rate is displayed as a function of two phases, defined as the fractional parts of the quantum numbers at dissociation $v_{\rm D,s}$ and $v_{\rm D,t}$ for the singlet and triplet states, respectively. These each

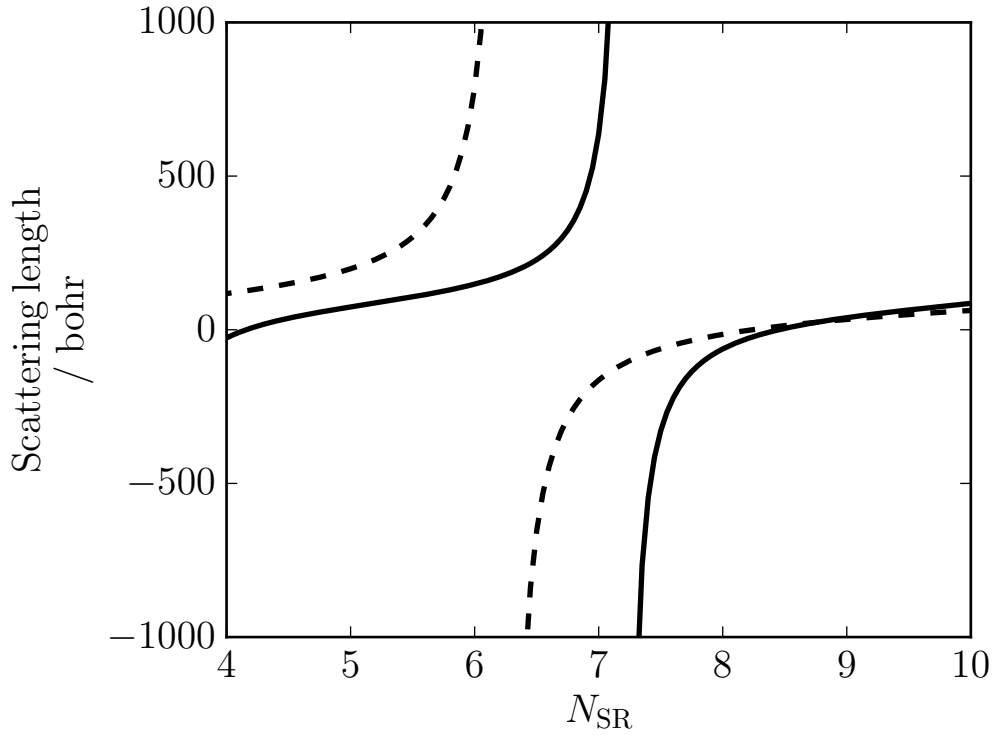

Figure 3.9: Variation of a_{s} (solid line) and a_{t} (dashed line) as a function of short-range power N_{SR} with short-range matching point $R_{\mathrm{SR}} = 3.5$ Å.

map onto the corresponding scattering length according to

$$a = \bar{a}\left[1 - \tan\left(v_{\mathrm{D}} + \tfrac{1}{2}\right)\pi\right], \tag{3.2.9}$$

where $\bar{a} = 0.477988\ldots(2\mu C_6/\hbar^2)^{-1/4}$ is the mean scattering length of Gribakin and Flambaum [173] and C_6 is the leading long-range dispersion coefficient. For ^{87}Rb, $\bar{a} = 78.95$ bohr. The mapping between scattering length and v_{D} is in Fig. 3.10.

Figure 3.11(b) shows that $k_2^{\max}$ varies by more than 10 orders of magnitude as a function of the singlet and triplet scattering lengths. Both $k_2^{\max}$ and a_{rf} depend only on the fractional parts of v_{D} for the singlet and triplet states (and hence on a_{s} and a_{t}), as indicated by the repeating patterns in Fig. 3.11. The most striking feature of Fig. 3.11(b) is a deep diagonal trough in the rf-induced loss rate when $v_{\mathrm{D,s}} \approx v_{\mathrm{D,t}}$ ($a_{\mathrm{s}} \approx a_{\mathrm{t}}$), with no corresponding feature in a_{rf}. Superimposed on this are peaks in $k_2^{\max}$ and poles in the corresponding a_{rf} shown in Fig. 3.11(a). These are of three different types. First, there are near-vertical bands near integer values

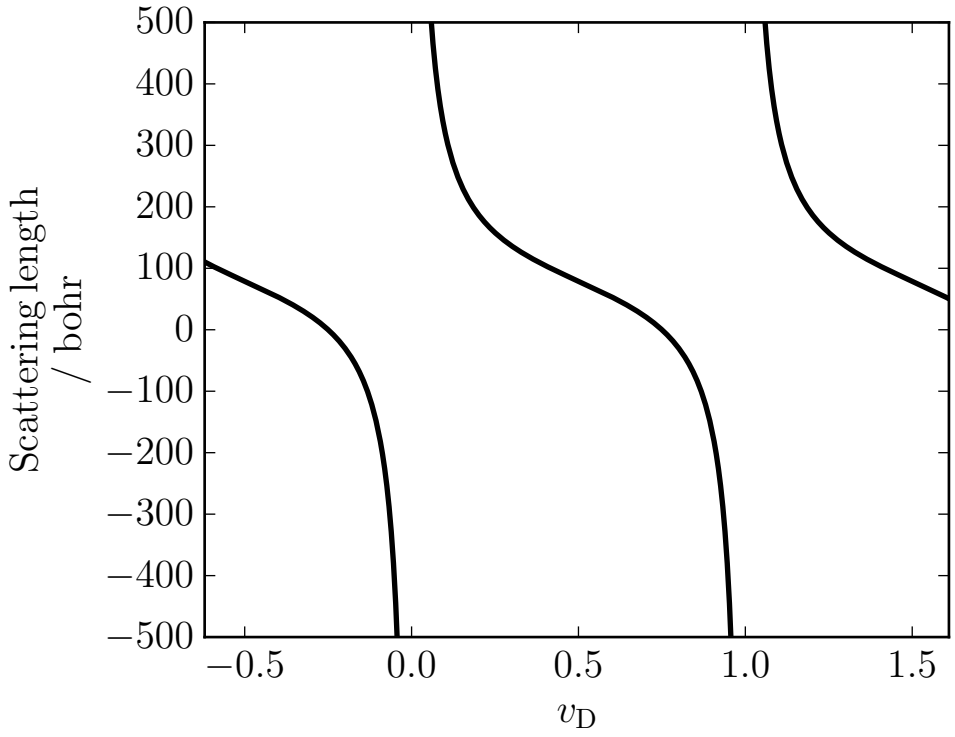

Figure 3.10: Mapping between v_{D} and the singlet and triplet scattering lengths according to Eq. 3.2.9.

of $v_{\mathrm{D,t}}$, corresponding to $|a_{\mathrm{t}}| = \infty$. These are entrance-channel resonances; they occur near integer values of $v_{\mathrm{D,t}}$ because the incoming channel is mostly triplet in character. Secondly, there is a Feshbach resonance due to a closed channel with excited hyperfine character ($f = 2$ here), which produces curving bands of peaks in $k_2^{\max}$ that cross the vertical bands near $v_{\mathrm{D,s}} = 0.1$. Lastly, there is an additional Feshbach resonance that produces very narrow vertical bands of peaks near $v_{\mathrm{D,t}} = 0.3$; these arise from pure triplet states that exist at the $(f_1, f_2) = (1, 2)$ threshold in the absence of rf and magnetic fields.

To explore the dependence of the pattern on hyperfine splitting, calculations were repeated for a series of artificial systems with the ^{87}Rb hyperfine splitting reduced from its real value, using the same set of interaction potentials. The results with the hyperfine splitting at 70% of its real value are shown in Fig. 3.12. The general form of the contour plot is unchanged, with a deep trough around $v_{\mathrm{D,s}} \approx v_{\mathrm{D,t}}$ ($a_{\mathrm{s}} \approx a_{\mathrm{t}}$) and peaks around vertical bands at integer values of $v_{\mathrm{D,t}}$. As expected, however, the Feshbach peaks have shifted. They now display distinct *avoided* crossings with the

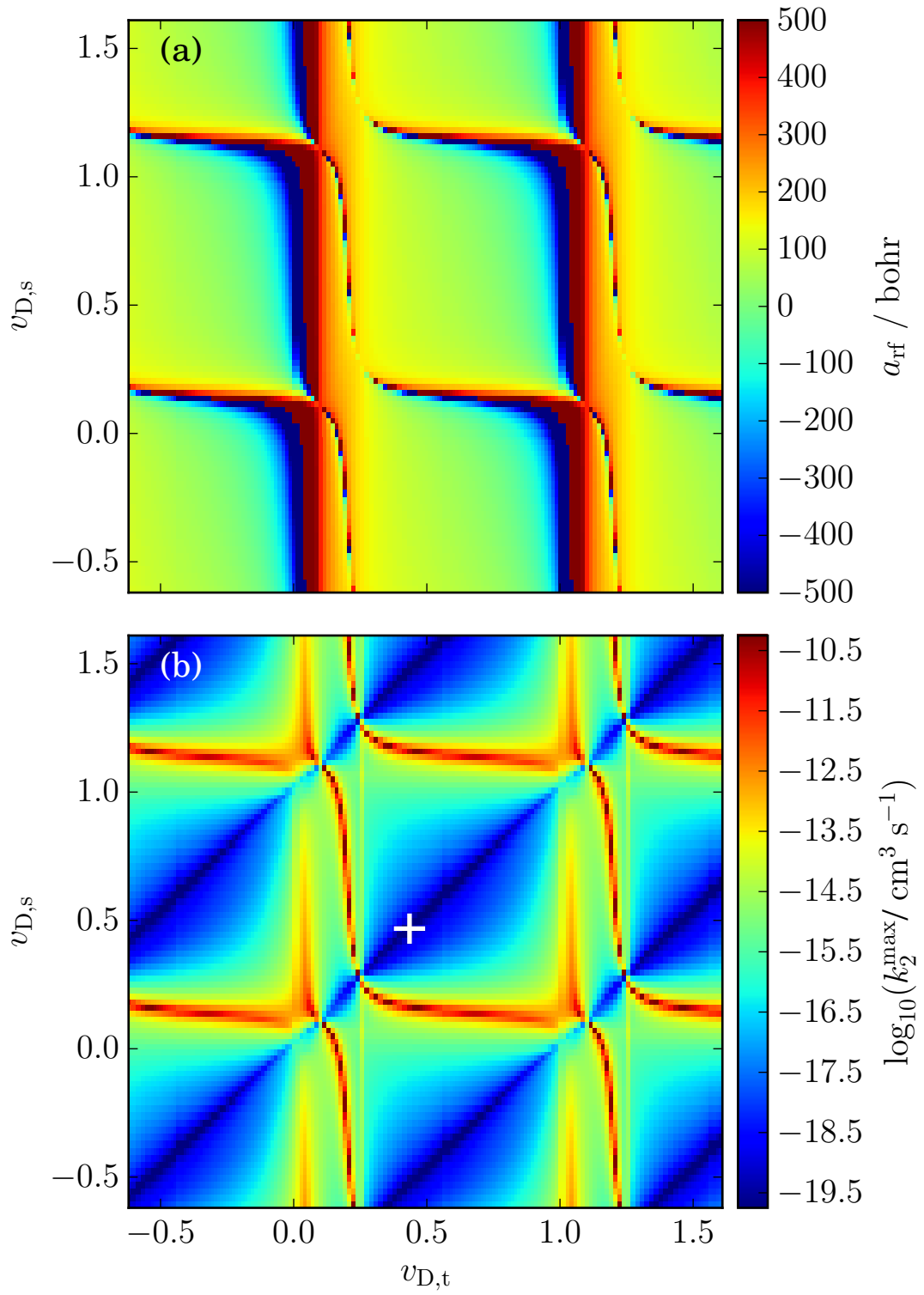

Figure 3.11: Contour plots of the dependence of collision properties on the fractional part of v_{D} for the singlet and triplet states, for adiabatically trapped ^{87}Rb in $f = 1$ with $\nu = 3.0$ MHz, $B_{\mathrm{rf}} = 0.5$ G and σ_- polarisation. (a) Real part of scattering length a_{rf}; (b) Rate coefficient for rf-induced loss at the trap center, k_2^{max}. The white cross indicates the position of the real values of a_{s} and a_{t} for ^{87}Rb.

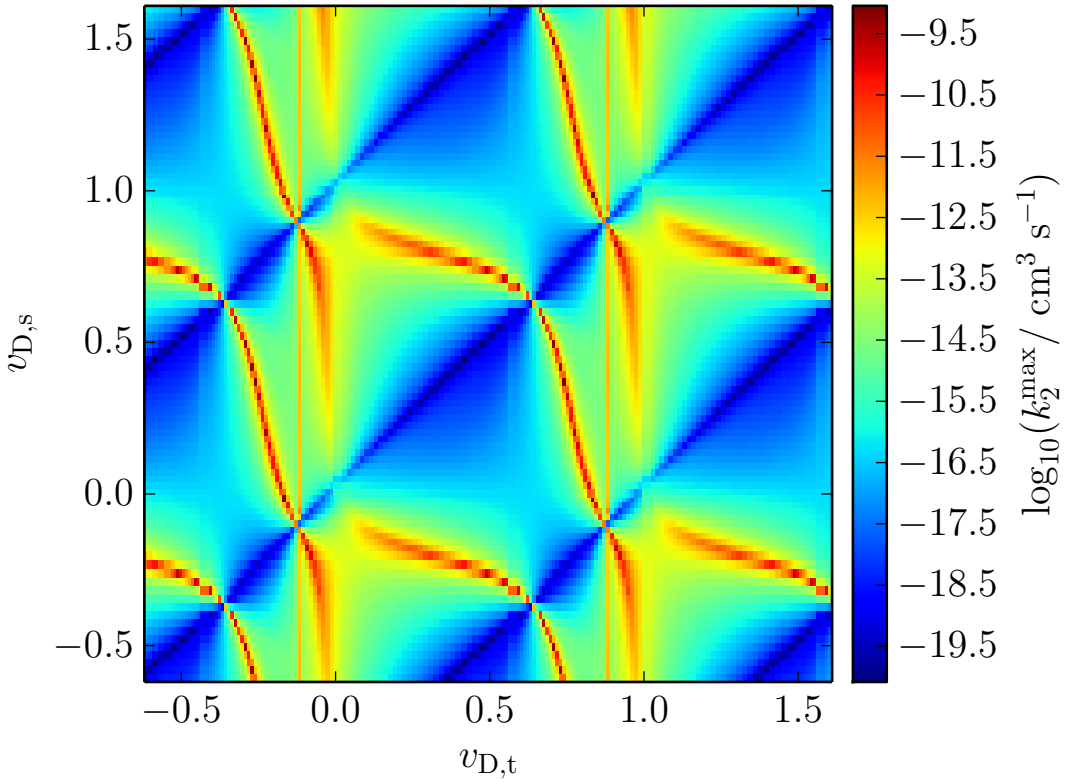

Figure 3.12: Contour plot of the rate coefficient for rf-induced loss at the trap center, for adiabatically trapped $f = 1$ states of an artificial atom with a hyperfine splitting 0.7 times that of ^{87}Rb. All other quantities are the same as for Fig. 3.11.

vertical bands of peaks. For some values of the hyperfine splitting, the crossings are so strongly avoided that the vertical bands near integer $v_{\mathrm{D,t}}$ are barely identifiable.

The actual singlet and triplet scattering lengths for ^{87}Rb are indicated by a cross on Fig. 3.11(b). This shows that ^{87}Rb is special in two different ways. Not only are its singlet and triplet scattering lengths quite similar, but their actual values correspond to $v_{\mathrm{D}} \approx 0.5$ and lie well away from the peaks due to Feshbach resonances. The value of $k_2^{\max}$ at the deepest point in the trough in Fig. 3.11(a) is about $k_2^{\max} = 3.6 \times 10^{-20}\ \mathrm{cm}^3\,\mathrm{s}^{-1}$, which is not far from the value of $1.25 \times 10^{-20}\ \mathrm{cm}^3\,\mathrm{s}^{-1}$ obtained for ^{87}Rb on the potentials of ref. [172].

Figure 3.13 shows a contour plot similar to Fig. 3.12 but with the hyperfine splitting of ^{39}K (462 MHz). The structure is similar, with a Feshbach resonance avoided-crossing with vertical bands of peaks at integer $v_{\mathrm{D,t}}$, though the resonances are distinctly wider than in Figs. 3.11(b) and 3.12. The actual scattering lengths of ^{39}K are shown as a black cross; the value of $k_2^{\max}$ at this point is $5.3 \times 10^{-14}\ \mathrm{cm}^3\,\mathrm{s}^{-1}$,

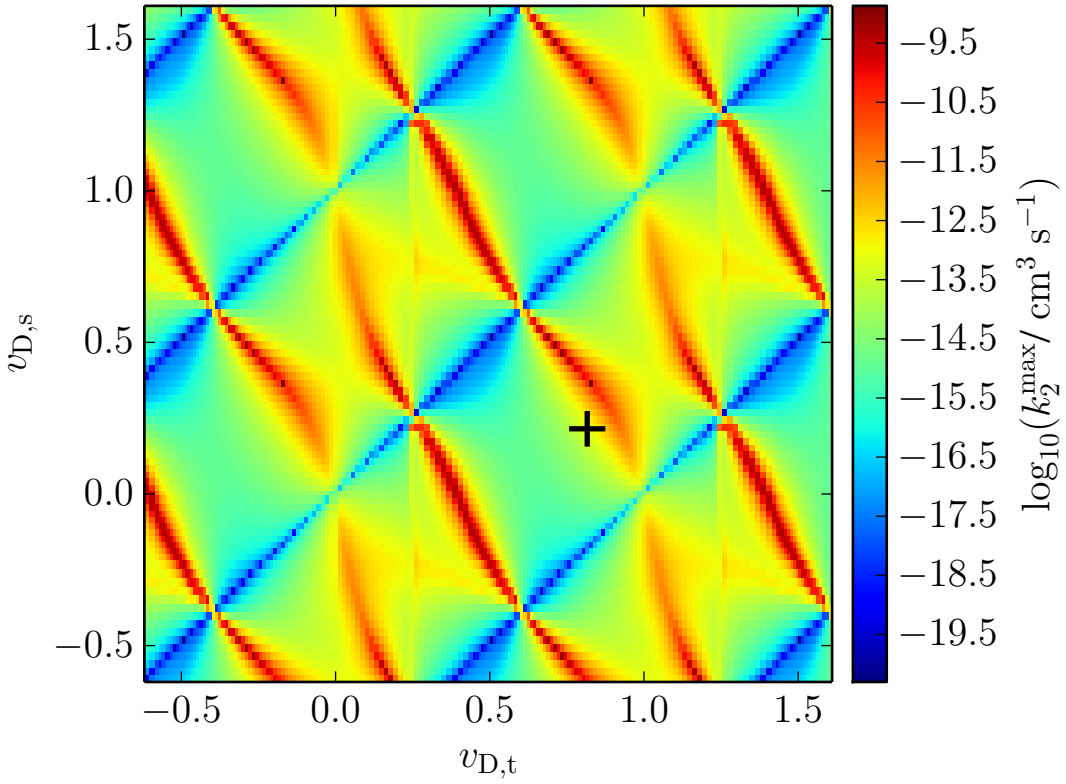

Figure 3.13: Contour plot of the rate coefficient for rf-induced loss at the trap center, for adiabatically trapped $f = 1$ states of an artificial atom with the mass of ^{87}Rb with the hyperfine splitting of ^{39}K. All other quantities are the same as for Fig. 3.11. The black cross indicates the position of the real values of a_{s} and a_{t} for ^{39}K.

which may be compared with $k_2^{\max} = 6.33 \times 10^{-14}$ cm^3 s^{-1} from the calculation with the mass and interaction potentials for ^{39}K in section 3.2.1. The difference in these numbers arises from the fact that Fig. 3.13 was obtained using Rb interaction potentials and reduced mass.

3.2.3 Inelastic collisions of rf-dressed $f = 2$ states of ^{87}Rb+^{87}Rb and ^{39}K+^{39}K

A somewhat different case occurs for atoms in $f = 2$ states. Here there are 5 photon-dressed atomic states that cross as a function of magnetic field, as shown for ^{87}Rb in Fig. 3.14. It requires a minimum of 5 rf-free states with photon numbers N from -2 to 2 to describe a single trapped atom. Because in this case the atom is in its upper hyperfine state, σ_+ polarisation is required to couple the relevant rf-dressed

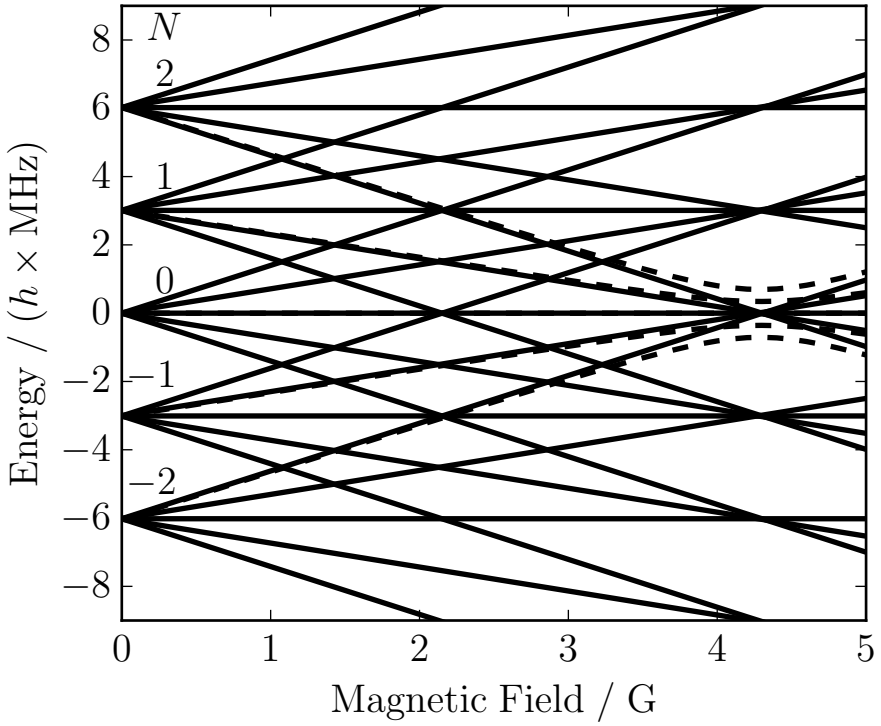

Figure 3.14: rf-dressed atomic levels of $f = 2$ states of ^{87}Rb for frequency 3.0 MHz and photon numbers $N = -2$, -1, 0, 1 and 2, shown with respect to the energy of the $f = 2$, $m_f = 0$ state for $N = 0$. Solid lines show levels for zero rf intensity and dashed lines show levels for $B_{\rm rf} = 0.5\,$G and σ_+ polarisation with $M_{\rm tot} = 0$. Atoms can be trapped at the minimum in the uppermost dashed curve.

states. Describing two such atoms requires photon numbers from -4 to 4. The coupled-channel calculation is thus computationally considerably more expensive. Nevertheless, the principles are exactly the same and rate coefficients for inelastic loss can again be obtained from the imaginary part of the complex scattering length, for atoms initially at the highest rf-dressed threshold.

Figure 3.15 shows the rate coefficient for inelastic loss for ^{87}Rb in $f = 2$, as a function of magnetic field near the trap center. As before, Fig. 3.15(a) shows the rf-induced loss, from a calculation with $L_{\rm max} = 0$, while Fig. 3.15(b) shows the loss including spin relaxation, from a calculation with $L_{\rm max} = 2$. The rf-induced loss rate is about a factor of 400 larger than for ^{87}Rb in $f = 1$ with $k_2^{\rm max} = 5.47 \times 10^{-18}$ cm^3 s^{-1}, but it is still much lower than the loss rate due to spin relaxation. Once again this illustrates the special properties of ^{87}Rb.

The dependence of $k_2^{\rm max}$ for the $f = 2$ states of ^{87}Rb$_2$ on the singlet and triplet

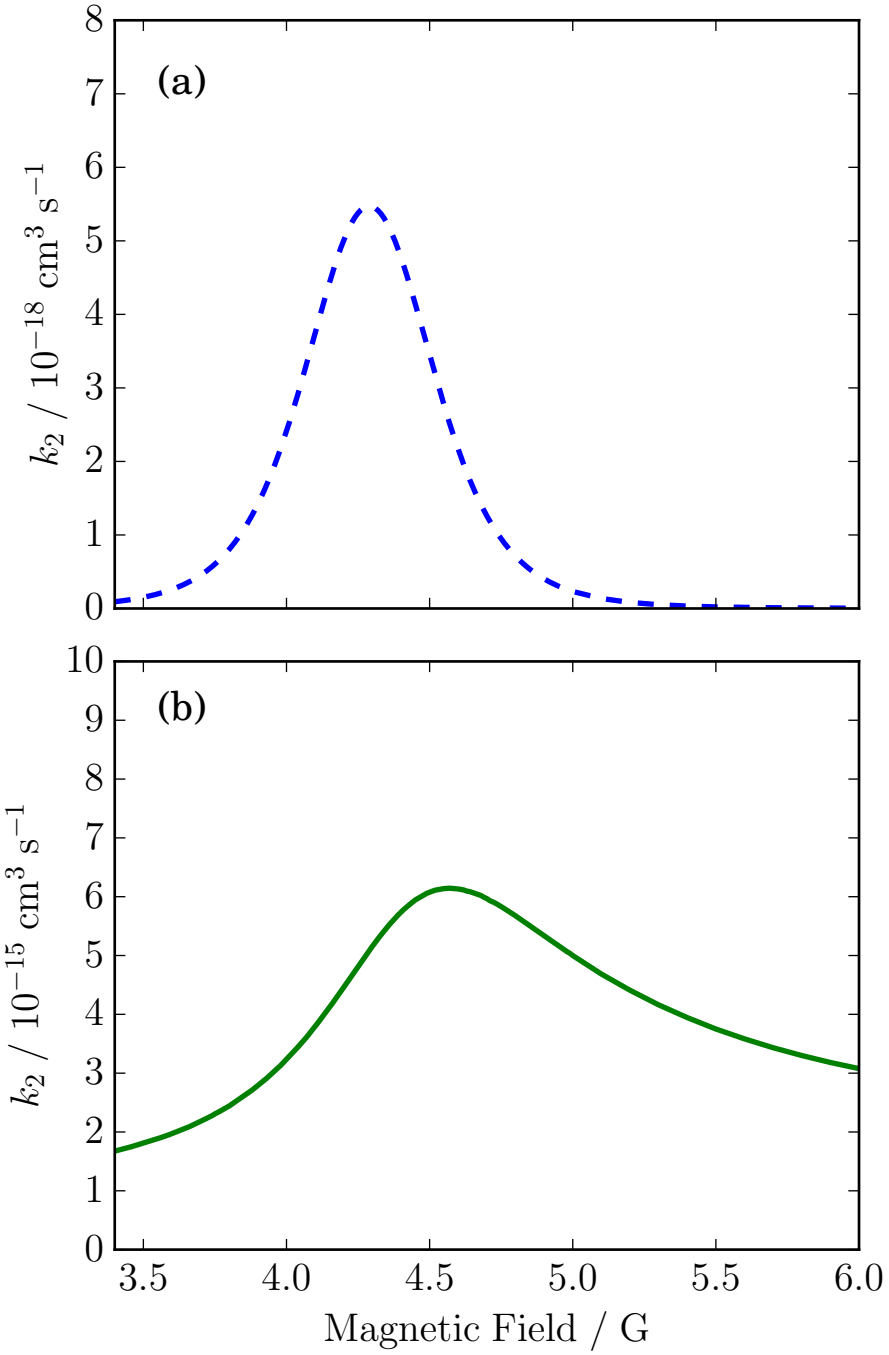

Figure 3.15: Rate coefficient for inelastic loss of adiabatically trapped ^{87}Rb in $f = 2$ as a function of magnetic field with $\nu = 3.0$ MHz and $B_{\mathrm{rf}} = 0.5$ G. (a) Calculation of rf-induced loss, using $L_{\mathrm{max}} = 0$. (b) Calculation including spin relaxation, using $L_{\mathrm{max}} = 2$.

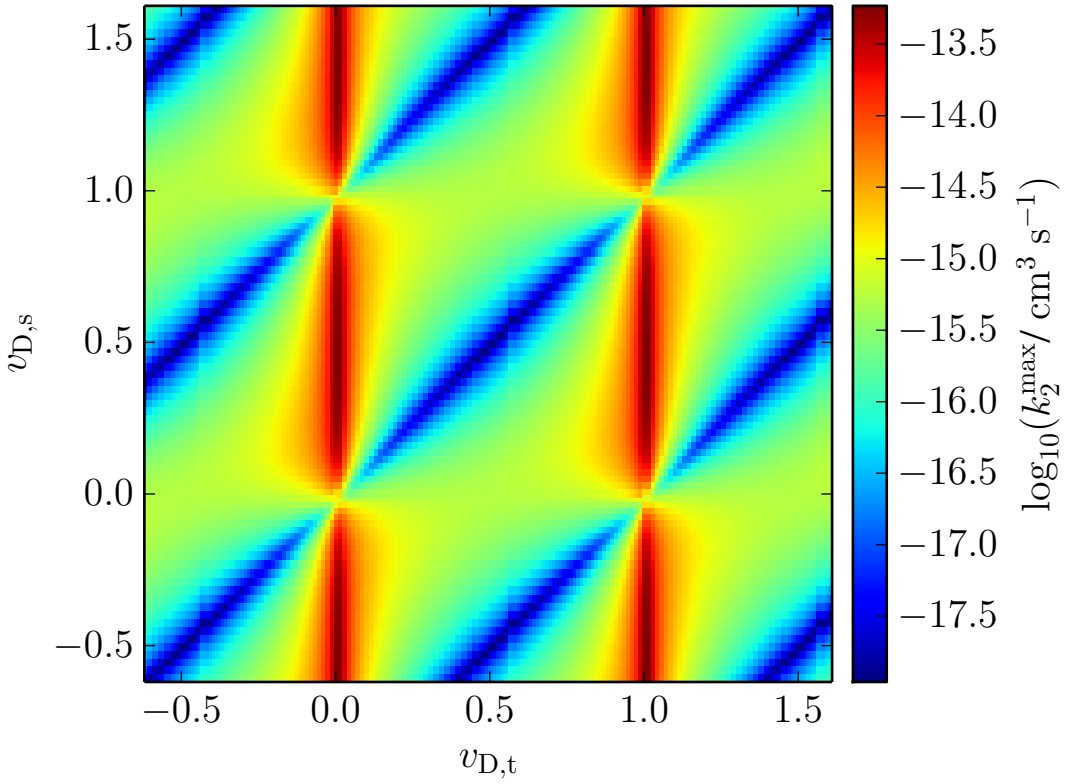

Figure 3.16: Contour plot of the rate coefficient for rf-induced loss at the trap center, for adiabatically trapped $f = 2$ states of ^{87}Rb. All other quantities are the same as for Fig. 3.11.

scattering lengths is shown in Fig. 3.16. It has a considerably simpler structure than Figs. 3.11, 3.12 and 3.13, because the atoms are both in their upper hyperfine state and there are no closed channels that can cause Feshbach resonances. The only features are a diagonal trough for $v_{\mathrm{D,s}} \approx v_{\mathrm{D,t}}$ ($a_{\mathrm{s}} \approx a_{\mathrm{t}}$) and a near-vertical band of maxima where $v_{\mathrm{D,t}}$ is close to an integer. These have the same causes as discussed for $f = 1$ above.

For atoms trapped in their upper hyperfine state, with no Feshbach resonances, the dependence of k_2^{max} on a_{s} and a_{t} may be expected to resemble Fig. 3.16 qualitatively for all atoms. However, there is a strong overall dependence on the hyperfine coupling constant. To illustrate this, the calculations shown in Fig. 3.16 were repeated with the hyperfine coupling constant set to the value for ^{39}K but the reduced mass retained at the value for ^{87}Rb. The results are shown in Fig. 3.17. It may be seen that the general structure of peaks and troughs is unchanged, but the peaks are about a factor of 200 higher for the smaller hyperfine splitting of ^{39}K (462 MHz)

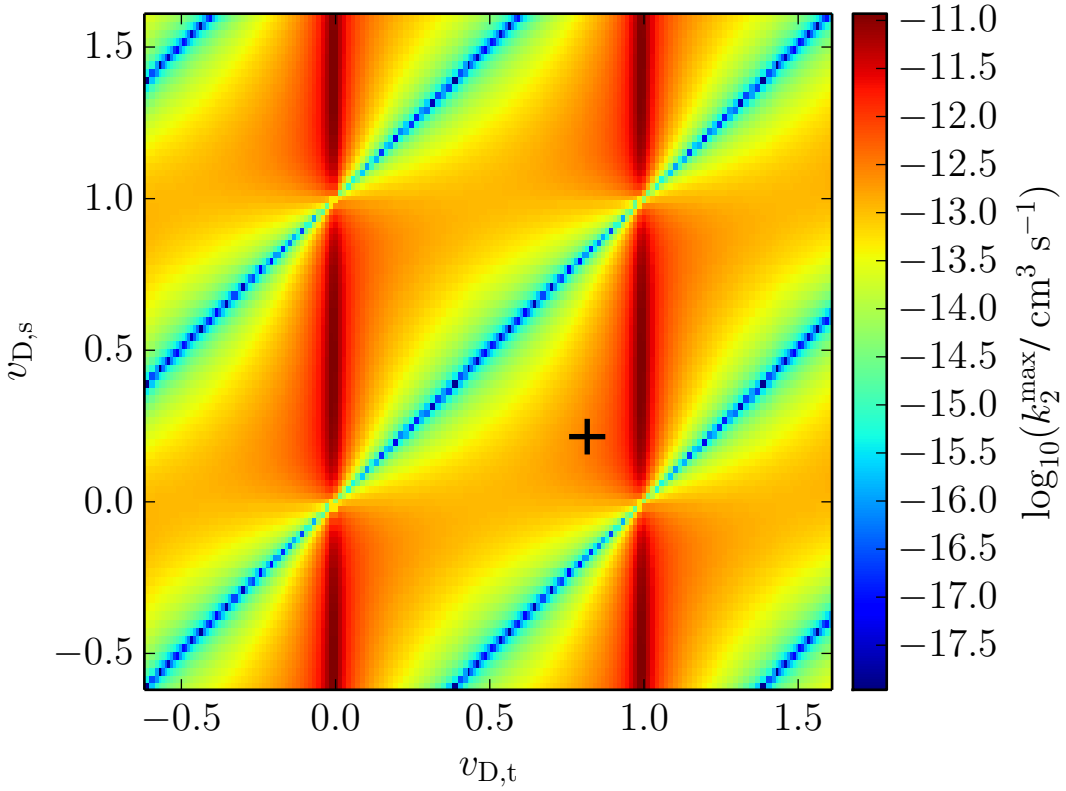

Figure 3.17: Contour plot of the rate coefficient for rf-induced loss at the trap center, for adiabatically trapped $f = 2$ states of an artificial atom with the mass of ^{87}Rb but the hyperfine splitting of ^{39}K. All other quantities are the same as for Fig. 3.11. The black cross indicates the position of the real values of a_{s} and a_{t} for ^{39}K.

than for that of ^{87}Rb (6,834 MHz).

The specific case of ^{39}K in rf-dressed $f = 2$ states is of interest. Figure 3.18 shows k_2 as a function of magnetic field from calculations with $L_{\mathrm{max}} = 0$ and 2, using the potentials of ref. [174]. It may be seen that, as for ^{39}K in $f = 1$, the rf-induced loss dominates the loss due to rf-modified spin relaxation. The rate coefficient peaks at $k_2^{\mathrm{max}} = 5.38 \times 10^{-13}\ \mathrm{cm}^3\,\mathrm{s}^{-1}$. The rf-induced loss is about 5 orders of magnitude faster than for ^{87}Rb, and again more typical. The value is comparable to the one from Fig. 3.17 at the values of $v_{\mathrm{D,s}}$ and $v_{\mathrm{D,t}}$ for ^{39}K, shown with a black cross, which is $k_2^{\mathrm{max}} = 2.34 \times 10^{-13}\ \mathrm{cm}^3\,\mathrm{s}^{-1}$. Again, the difference between these two values arise because the calculations in Fig. 3.17 used the reduced mass and interaction potentials for ^{87}Rb rather than ^{39}K.

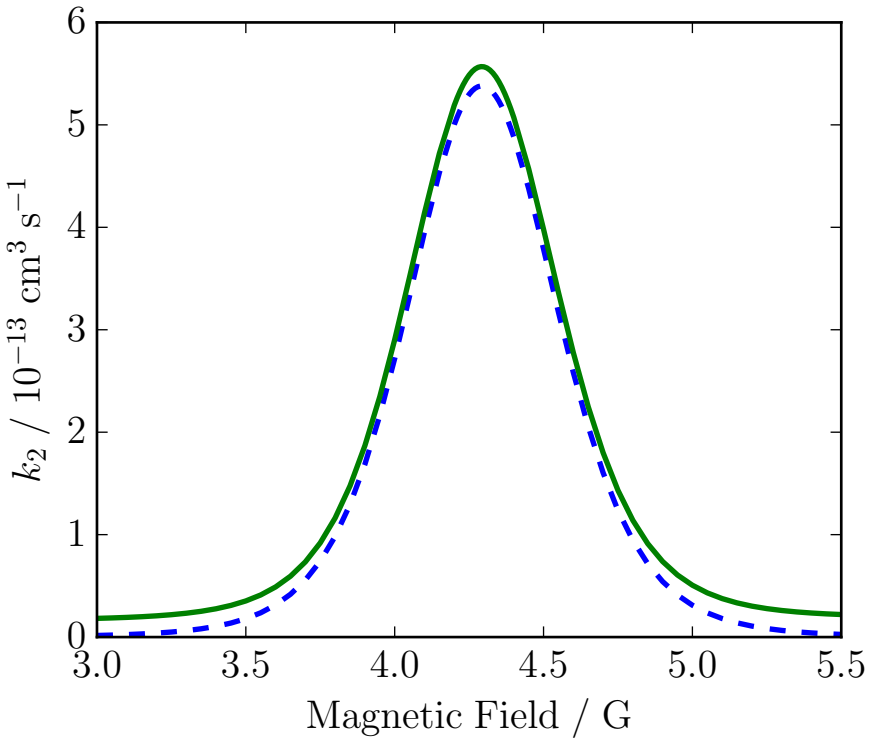

Figure 3.18: Rate coefficient for inelastic loss of adiabatically trapped ^{39}K in $f = 2$ as a function of magnetic field with $\nu = 3.0$ MHz and $B_{\rm rf} = 0.5$ G. Results are shown including spin relaxation, using $L_{\rm max} = 2$ (solid, green) and for rf-induced loss alone, using $L_{\rm max} = 0$ (dashed, blue).

3.2.4 Inelastic collisions of rf-dressed ^{85}Rb

Another case of interest is atoms for which $f = 2$ is not the highest state, such as ^{85}Rb. The rf-dressed thresholds for ^{85}Rb in $f = 2$ require the same photon numbers as ^{87}Rb and ^{39}K in $f = 2$ (but with σ_- polarisation), and are similar to those in Fig. 3.14 but the trap centre is shifted upfield to 6.42 G due to the smaller Landé g-factor of ^{85}Rb. The rf-induced loss rate is shown as a function of magnetic field in Fig. 3.19. The loss with $L_{\rm max} = 0$ shows a similar profile to ^{87}Rb but the maximum loss is 3 orders of magnitude larger, with $k_2^{\rm max} = 3.34 \times 10^{-15}$ cm^3 s^{-1}. Like ^{87}Rb, the rf-induced loss is dominated by rf-modified spin relaxation but the differences in the respective loss rates is only one order of magnitude, compared to a difference of 4 orders of magnitude beween the rf-induced loss and rf-modified spin relaxation loss in ^{87}Rb. Including spin relaxation, the loss in the presence of an rf field approaches the rf-free spin relaxation loss as a function of magnetic field for two colliding ^{85}Rb

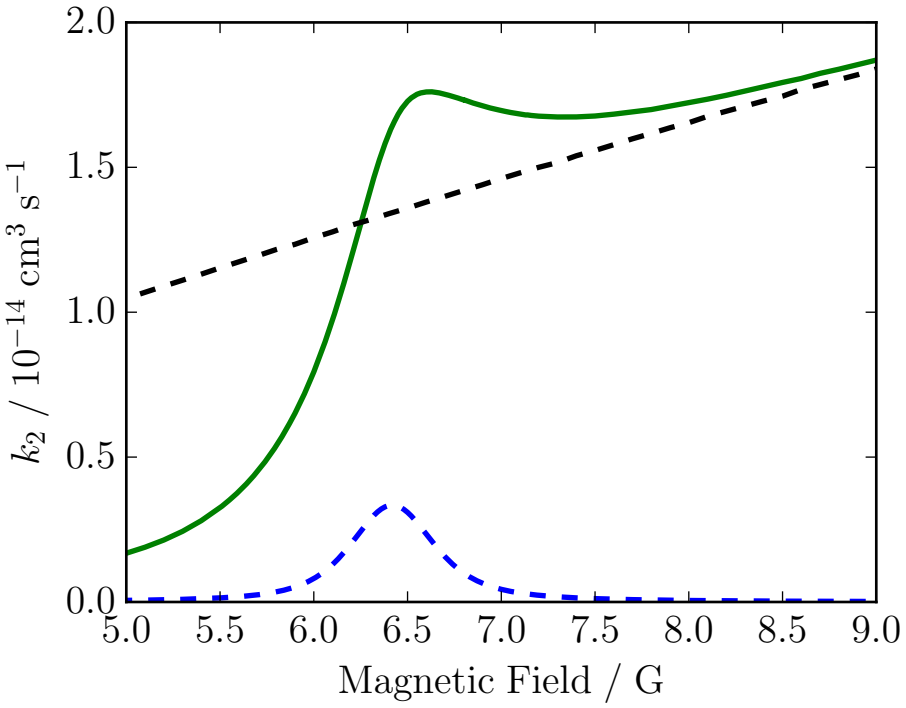

Figure 3.19: Rate coefficient for inelastic loss of adiabatically trapped ^{85}Rb in $f = 2$ as a function of magnetic field with $\nu = 3.0$ MHz and $B_{\mathrm{rf}} = 0.5$ G and σ_- polarisation. Results are shown including spin relaxation, using $L_{\mathrm{max}} = 2$ (solid, green) and for rf-induced loss alone, using $L_{\mathrm{max}} = 0$ (dashed, blue). The dashed black line shows the rf-free spin relaxation for ^{85}Rb atoms in $(f, m_f) = (2, -2)$.

atoms in $(f, m_f) = (2, -2)$, shown by the dashed black line in Fig. 3.19.

Given that $a_{\mathrm{s}} \neq a_{\mathrm{t}}$ in ^{85}Rb ($a_{\mathrm{s}} \approx 2560$ bohr and $a_{\mathrm{t}} \approx -380$ bohr), it is somewhat unexpected that the rf-induced loss is dominated by spin relaxation. The dependence of k_2^{max} on a_{s} and a_{t} is shown by the contour plot Fig. 3.20. k_2^{max} varies by over 10 orders of magnitude and, as expected for an atom not in its highest hyperfine state, there is a curving Feshbach structure originating from closed $f = 3$ channels. There is also a pure triplet Feshbach resonance indicated by the faint vertical band at around $v_{\mathrm{D}} = 0.4$. The black cross indicates where the real values of a_{s} and a_{t} for ^{85}Rb lie, and it highlights an interesting coincidence; the cross lies very close to a trough, but the loss is enhanced by the proximity of a Feshbach resonance. This enhancement closes the gap in magnitude between the rf-induced loss and rf-modified spin relaxation loss.

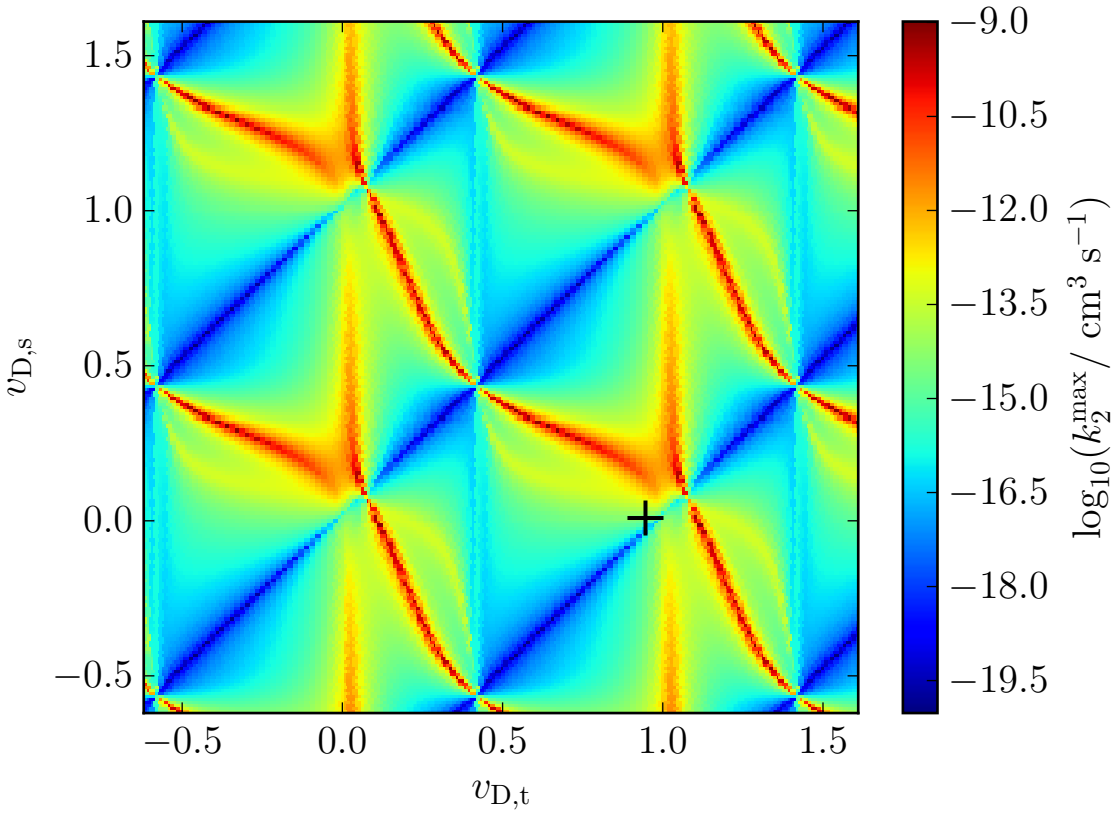

Figure 3.20: Contour plot of the rate coefficient for rf-induced loss at the trap center, for adiabatically trapped $f = 2$ states of ^{85}Rb. All other quantities are the same as for Fig. 3.11. The black cross indicates the position of the real values of a_{s} and a_{t} for ^{85}Rb.

Collisions of a pair of rf-dressed ^{85}Rb atoms in $f = 3$ require photon numbers $N = 6$ to -6 (and σ_+ polarisation). As with ^{87}Rb, the inelastic loss is greater at the higher hyperfine manifold but with an increase of 1 order of magnitude compared to 2 orders in ^{87}Rb; Fig. 3.21 shows that the rf-induced loss rate coefficient has a maximum of 2.27×10^{-14} cm^3 s^{-1}, about 2.4×10^4 larger than for ^{87}Rb in $f = 2$. The rf-modified spin relaxation is only about four times greater than the rf-induced loss, compared to the order of magnitude for the $f = 2$ case, and approaches the rf-free spin relaxation loss rates for $(m_{f,1}, m_{f,2}) = (3, 3)$ and $(-3, -3)$ on the left and right hand sides of $k_2^{\max}$, respectively. The contour plot of Fig. 3.22 shows the expected structure for colliding alkali-metal atoms in their upper hyperfine states, qualitatively resembling Fig. 3.16 but with resonant peaks in $k_2^{\max}$ an order of magnitude higher compared to ^{87}Rb in its upper hyperfine state. The position of the cross in Fig. 3.22 also

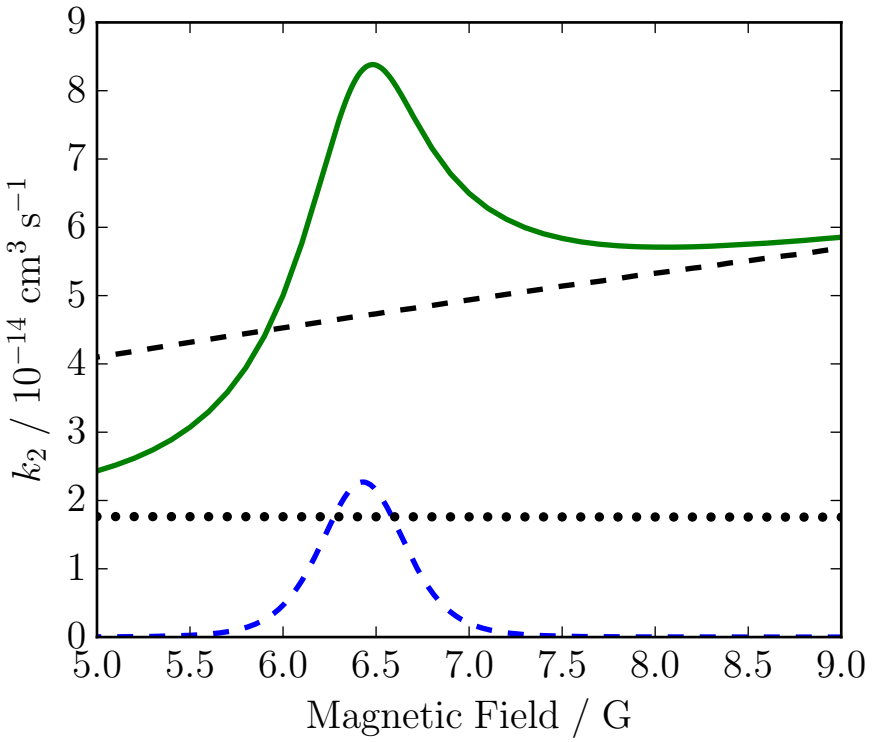

Figure 3.21: Rate coefficient for inelastic loss of adiabatically trapped ^{85}Rb in $f = 3$ as a function of magnetic field with $\nu = 3.0$ MHz and $B_{\rm rf} = 0.5$ G and σ_+ polarisation. Results are shown including spin relaxation, using $L_{\rm max} = 2$ (solid, green) and for rf-induced loss alone, using $L_{\rm max} = 0$ (dashed, blue). The dashed black lines indicate the rf-free spin relaxation for $m_{f,1}, m_{f,2}) = (3, 3)$, and the dotted black lines for $(-3, -3)$.

shows that the rf-induced loss is enhanced by the entrance channel resonance at $v_{\rm D,t} = 1.0$, resulting in the reduced difference between the rf-induced and rf-modified spin relaxation losses.

3.2.5 Inelastic collisions of rf-dressed ^{87}Rb+^{85}Rb

Collisions in heteronuclear mixtures are also of interest. Dressed with one rf field, the different Landé g-factors of the atoms will result in two sets of avoided crossings in the collision thresholds separated in magnetic field. This is illustrated in Fig. 3.23 with ^{87}Rb+^{85}Rb in their respective hyperfine ground states of $f = 1$ and $f = 2$. The separation of the avoided crossings in magnetic field, ΔB, can be written

$$\Delta B = |B_{0,\rm a} - B_{0,\rm b}| = |\frac{\nu\hbar}{\mu_{\rm B}} \left(|g_{f,1}|^{-1} - |g_{f,2}|^{-1} \right)| \qquad (3.2.10)$$

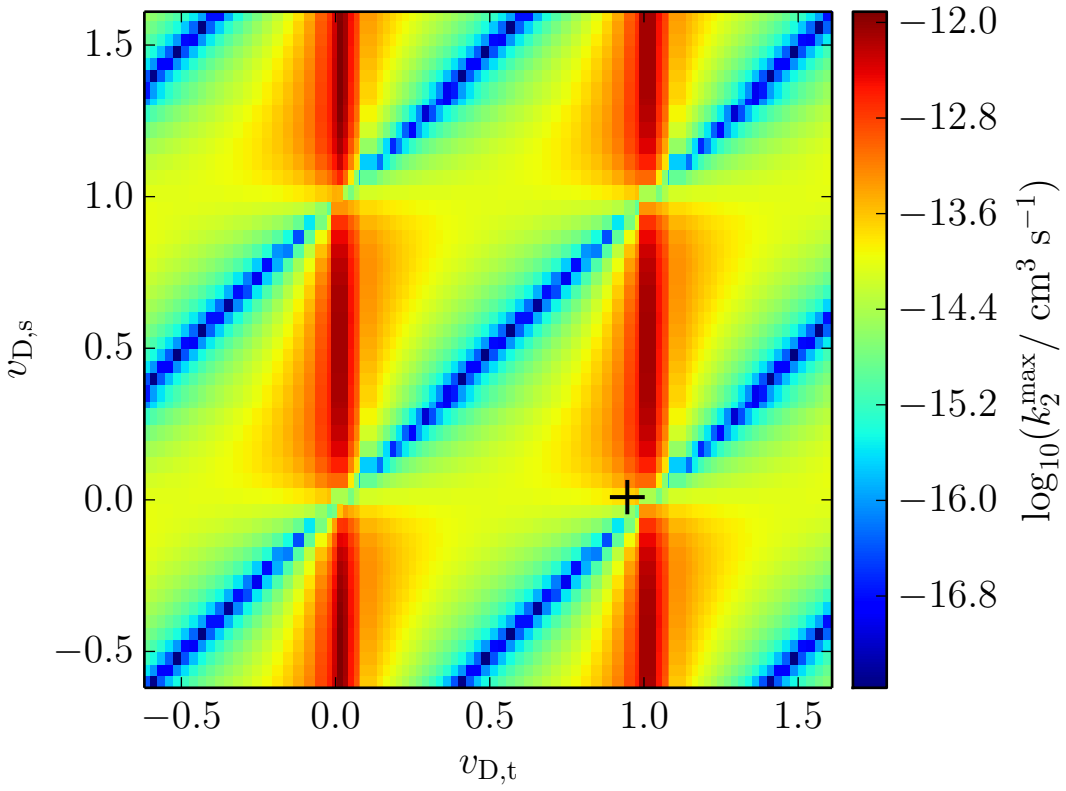

Figure 3.22: Contour plot of the rate coefficient for rf-induced loss at the trap center, for adiabatically trapped $f = 3$ states of ^{85}Rb. All other quantities are the same as for Fig. 3.21. The black cross indicates the position of the real values of a_{s} and a_{t} for ^{85}Rb.

where $B_{0,\mathrm{a/b}}$ is the position in magnetic field where the Zeeman splitting equals the rf photon energy for atom a/b given by Eq. 3.1.4. For ^{87}Rb+^{85}Rb with $(f_{87}, f_{85}) = (1, 2)$ $\Delta B = 2.2$ G. A complete set of thresholds is obtained using $N_{\max} = 3$, with one photon needed to describe ^{87}Rb in $f = 1$, and two required for ^{85}Rb in $f = 2$. The thresholds are influenced by both atoms with each leaving a distinctive mark; the set of avoided crossings around 4.2 G and 6.4 G are due to ^{87}Rb and ^{85}Rb, respectively. Both ^{87}Rb and ^{85}Rb are trapped in the top threshold of Fig. 3.23 which has $(m_{f,87}, m_{f,85}, N) = (1, 2, 3)$ character on the low-field side of the crossings. We choose this threshold as the entrance channel in the following calculations.

The two-body loss as a function of magnetic field is shown in Fig. 3.24. In this case the loss rate peaks in a region between between the two sets of avoided crossings around 5.4 G. The magnitude of the loss in this case is much larger than in any homonuclear system previously considered, with a difference of three orders

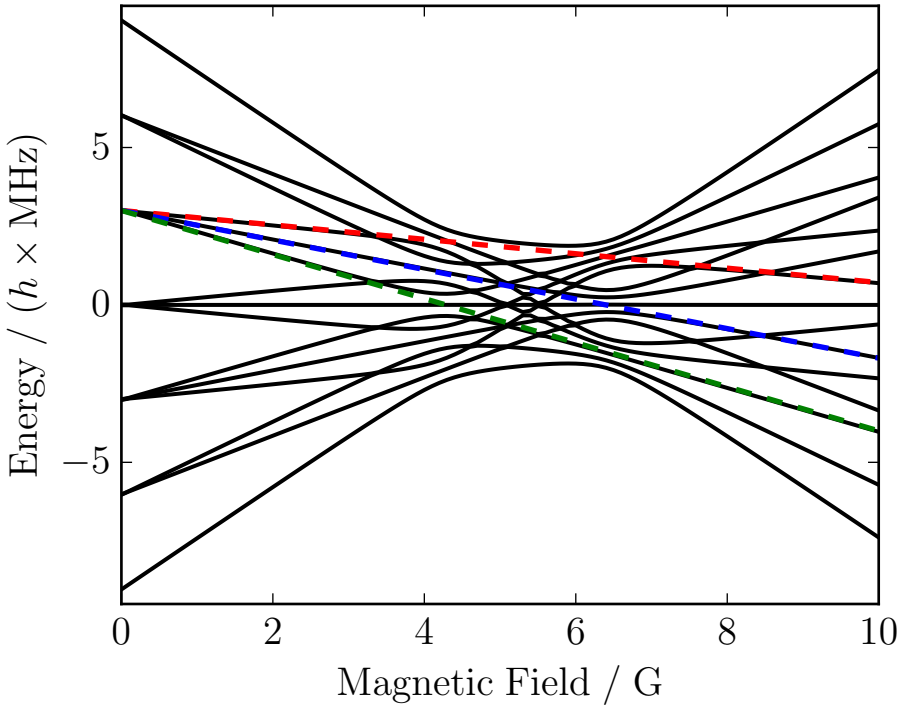

Figure 3.23: Rf-dressed thresholds for ^{87}Rb+^{85}Rb in their hyperfine ground states and $M_{\rm tot} = 0$, in an rf field with parameters $\nu = 3.0$ MHz and $B_{\rm rf} = 0.5$ G with σ_- polarisation.

of magnitude between this and the loss rate for ^{39}K in $f = 2$. The rf-induced loss is on the same order of magnitude as the rf-free spin exchange for $(m_{f,87}, m_{f,85}) = (-1, 2)$ which shown by the dashed black line in Fig. 3.24, and converges on it with decreasing $B_{\rm rf}$. Spin exchange is relevant because ΔB is non-zero, leading to regions in magnetic field which the rf-dressed atoms may adiabatically transfer into a well defined state and undergo rf-free spin exchange; in homonuclear cases rf-free spin exchange was not possible as the rf-dressed atoms transfered between two spin-stretched states via a single region of strong rf coupling at the trap centre.

At magnetic fields around 4.5 G to 6.5 G the entrance channel has well defined character $(m_{f,87}, m_{f,85}, N) = (-1, 2, 1)$. This can be understood by following the $(-1, 2, 1)$ state diabatically from low field, as indicated by the dashed red line in Fig. 3.23. The blue and green dashed lines diabatically follow the $(0, 1, 1)$ or $(1, 0, 1)$ states, to which $(-1, 2, 1)$ may decay via spin exchange. As $B_{\rm rf}$ is decreased the $(-1, 2, 1)$ character of the entrance channel increases in the region between the two sets of avoided crossings. This is demonstrated in Fig. 3.25 which reconstructs the

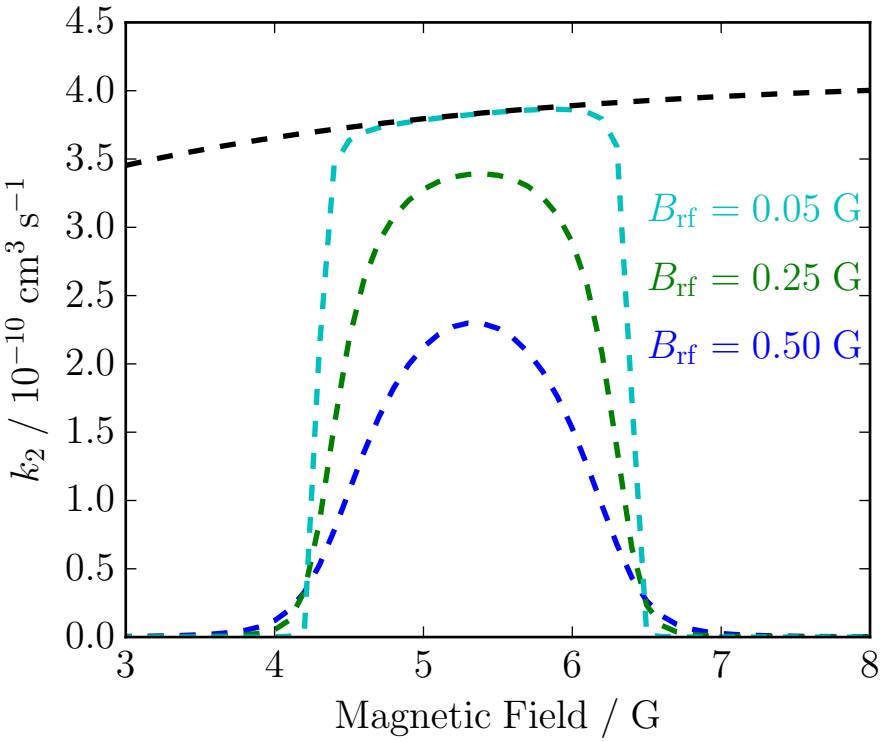

Figure 3.24: Rate coefficient for inelastic loss of adiabatically trapped ^{87}Rb+^{85}Rb in their hyperfine ground states as a function of magnetic field with the same rf field parameters as Fig. 3.23. Results are shown for several values of $B_{\rm rf}$ with $L_{\rm max} = 0$ using dashed blue, green and cyan lines for $B_{rmrf} = 0.5,\ 0.25$ and 0.05 G, respectively. The dashed black line shows the rf-free spin exchange loss rate for $(m_{f,87}, m_{f,85}) = (-1, 2)$.

rf-free spin exchange loss in the rf-dressed case by using $B_{\rm rf} = 0.05$ G and chooses the entrance channel for a value of magnetic field that corresponds to the dashed red diabat of 3.23. When $B_{\rm rf}$ is increased the couplings between rf-dressed states increase and the avoided crossings become more pronounced, shrinking the region in which the entrance channel has $(-1, 2, 1)$ character; the mixing of lower rf-dressed states that cannot undergo spin exchange leads to a less well defined state and so suppresses the spin exchange mechanism.

3.3 Conclusions

Cold atoms in rf-dressed traps may undergo inelastic collisions by mechanisms that do not occur in the absence of an rf field. These inelastic collisions may lead to trap

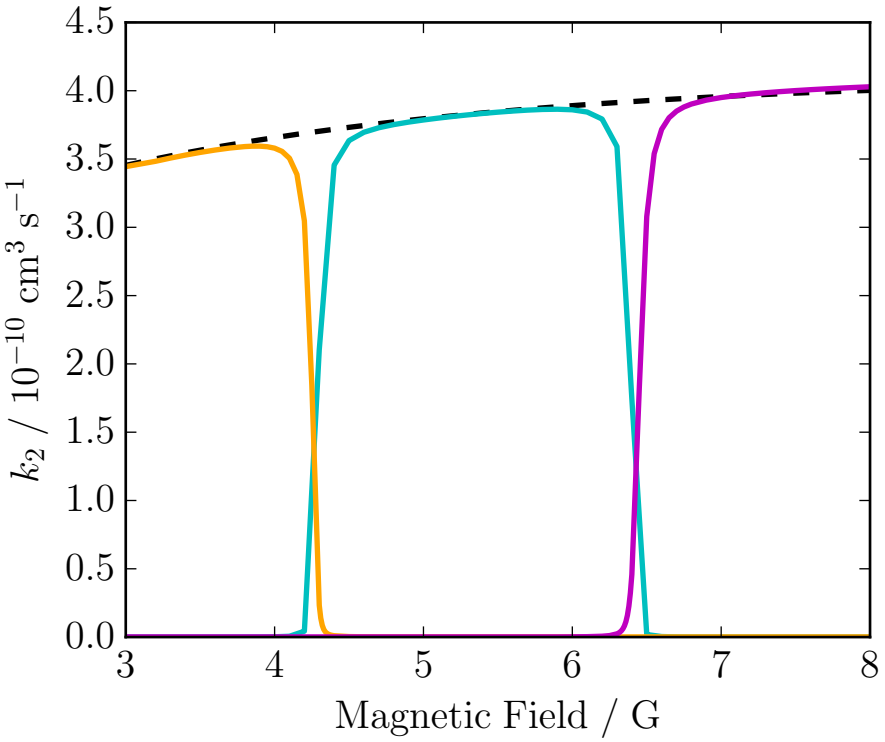

Figure 3.25: Rate coefficient for inelastic loss for ^{87}Rb+^{85}Rb for several incoming channels which correspond to the $(m_{f,87}, m_{f,85}, N) = (-1, 2, 1)$ channel in certain regions in magnetic field, as indicated by the dashed red line in Fig. 3.23: red for left of the avoided crossings, cyan for between the sets of avoided crossings and magenta for the right of the avoided crossings. The dashed black line shows the rf-free spin-exchange loss rate for $(m_{f,87}, m_{f,85}) = (-1, 2)$.

loss. There are two components of inelastic loss in the rf-dressed case. One is due to spin-relaxation collisions, driven by the dipolar interaction between the electron spins of the two atoms. This component exists even in the absence of rf dressing, but is generally fairly small, both because the dipolar interaction is weak and because there is a centrifugal barrier in the outgoing channel. It is modified in an rf field near the trap center because the rf-dressed states are mixtures of different spin states, and drops to zero on the low-field side of the trap, where the adiabatically trapped state correlates with lowest state in the magnetic field. The second component, which is referred to as rf-induced loss, is potentially stronger; the inelastic collisions are driven by the difference between the singlet and triplet interaction potentials, and there is no centrifugal barrier in the outgoing channel.

For ^{87}Rb in $f = 1$ states, the calculated rate coefficient for rf-induced loss is very

small with $k_2^{\max} = 1.25 \times 10^{-20}$ cm^3 s^{-1} at the trap center for an rf field strength $B_{\rm rf} = 0.5$ G with σ_- polarisation. This is 4 orders of magnitude smaller than the rf-modified spin-relaxation loss rate coefficient in this system.

The rf-induced loss rate is dependent on the singlet and triplet scattering lengths $a_{\rm s}$ and $a_{\rm t}$, and it can change by 10 orders of magnitude as the scattering lengths are varied. It is generally small when $a_{\rm s} \approx a_{\rm t}$, but may be enhanced by resonances of two different types. ^{87}Rb is a very special case: not only is $a_{\rm s}$ very similar to $a_{\rm t}$, but their actual values are such that there is no enhancement by any type of resonance. For ^{39}K, which is a more typical case, the $k_2^{\max} = 6.33 \times 10^{-14}$ cm^3 s^{-1} for $B_{\rm rf} = 0.5$ G with σ_- polarisation. This is an order of magnitude larger than the rf-modified spin-relaxation loss rate, and 6 orders of magnitude larger than the rf-induced loss rate for ^{87}Rb. The reason for the suppression of rf-induced loss when $a_{\rm s} \approx a_{\rm t}$ will be explored using an adiabatic model of the collision dynamics in the next chapter.

The effects of rf-induced loss using a $\sigma_{\rm x}$ polarised rf field was explored in collisions between ^{39}K. The rf-induced loss is similar to that for a circularly polarised field of half the intensity of the linearly polarised field, with small differences as a result of the states introduced by the σ_+ component of the linear combination, which shift collision thresholds slightly. A similar effect occurs when the rf and magnetic fields are not perpendicular to one another; $M_{\rm tot}$ is no longer conserved in this case and so all possible atomic m_f states must be included leading to further crossings.

Inelastic loss of rf-dressed alkali-metal atoms in their upper hyperfine states was also investigated, $f = 2$ for ^{87}Rb and ^{39}K. These losses are also small when $a_{\rm s} \approx a_{\rm t}$. In this case there are no Feshbach resonances, but the loss rates may still be enhanced by entrance-channel effects when $|a_{\rm t}|$ is large. The rf-induced loss rates also depend strongly on the atomic hyperfine splitting, increasing as the hyperfine splitting decreases because of mixing of atomic f states by the magnetic field.

Atoms for which $f = 2$ is not the highest hyperfine state such as ^{85}Rb, which has hyperfine ground state with $f = 2$, have an rf-induced loss dependent on $a_{\rm s}$ and $a_{\rm t}$ similar to those for $f = 1$ ground state atoms, with a variation in $k_2^{\max}$ of over 10 orders of magnitude. Because $f = 2$ is not the highest hyperfine state there are

Alkali-Metal Atom	Trap Centre / G	$k_2^{\max}$ / cm^3 s^{-1}
^{7}Li	4.26	7.96×10^{-15}
^{39}K	4.33	6.33×10^{-14}
^{41}K	4.27	1.72×10^{-16}
^{85}Rb	6.42	3.34×10^{-15}
^{87}Rb	4.27	1.25×10^{-20}
^{133}Cs	8.44	6.24×10^{-11}

Table 3.1: Trap centres and two-body loss rate coefficients, rf-induced loss at the trap centres, $k_2^{\max}$ (cm^3 s^{-1}), for bosonic alkali metal isotopes in their hyperfine grounstates with $\nu = 3.0$ MHz and $B_{\rm rf} = 0.5$ G

closed channels that give rise to Feshbach structure in the contour plots. For ^{85}Rb, whilst $a_{\rm s} \neq a_{\rm t}$, their values place the real system in near a trough of the contour plot suppressing the rf-induced loss. A nearby Feshbach resonance counteracts this suppression, resulting in an rf-induced loss that is still suppressed, but only one order of magnitude less than the rf-modified spin relaxation loss; this may be compared to a difference of four orders of magnitude in ^{87}Rb. The rf-induced loss is still large compared to ^{87}Rb, with $k_2^{\max} = 3.34 \times 10^{-15}$ cm^3 s^{-1}. In its upper hyperfine state with $f = 3$, the rf-induced loss for ^{85}Rb is less than one order of magnitude smaller than the rf-modified spin relaxation, and its relationship to $a_{\rm s}$ and $a_{\rm t}$ qualitatively resembles that of ^{87}Rb and ^{39}K in $f = 2$.

In general other alkali-metal atoms in their hyperfine ground states are expected to have much larger rf-induced loss rates than ^{87}Rb, as was shown for ^{39}K and ^{85}Rb,; Table 3.1 summarises the rf-induced losses at the trap centre for the cases studied above as well as some other bosonic alkali-metal atoms.

The heteronuclear system ^{87}Rb+^{85}Rb dressed by rf radiation shows asymmetric trapping potentials due to the differing Landé g-factors of the two atoms. This leads to an inelastic loss which is enhanced in regions of avoided crossings, but is suppressed from an rf-free spin exchange loss in between the avoided crossings for the two different atoms. This suppression results from the coupling of additional states which cannot decay to lower states via spin exchange; for $B_{\rm rf} = 0.5\,G$, $k_2^{\max}$ is a factor of 1.7 lower than the rf-free loss rate of ^{87}Rb+^{85}Rb in $(f, m_f) = (1, 1)+(2, -2)$. This rapid spin-exchange loss is expected for atomic mixtures where there is a difference in the Landé g-factors.

This chapter has focused on the rf-dressing of alkali-metal atoms using a single frequency. Dressing of magnetic traps using multiple rf fields [130, 175–177] may have advantages for avoiding the spin-exchange losses demonstrated in ^{87}Rb+^{85}Rb. Multiple frequencies of rf radiation could allow one to overlap the traps of two heteronuclear atoms; the trap position is determined by the Landé g-factor and rf photon frequency (Eq. 3.1.4), so the traps for heteronuclear atoms could be engineered to overlap if the frequency for each field is chosen carefully in relation to the Landé g-factor [178]. This is equivalent to setting $\Delta B = 0$ in Eq. 3.2.10. Although the rf field of frequency for atom a will interact with atom b and vice versa, each rf frequency should be detuned far enough from resonance from one atom to avoid unwanted loss.

Chapter 4

Adiabatic Model of Radio-frequency-Dressed Collision Dynamics

The previous chapter analysed rf-induced loss as a function of singlet and triplet scattering lengths, a_{s} and a_{t}, respectively. When $a_{\mathrm{s}} = a_{\mathrm{t}}$ the rf-induced loss is at a minimum, highlighted by a deep trough in contour plots showing the peak loss at the rf-dressed trap centre as a function of a_{s} and a_{t}. A similarly slow inelastic loss rate due to spin-exchange collisions exists for rf-free scattering of ^{87}Rb, as measured by Myatt *et al.* [179] in dual BECs of ^{87}Rb in $(f, m_f) = (1, -1)$ and $(2, 2)$ states. Julienne *et al.* [180] explained this suppression using an adiabatic model of the collision dynamics [181]. The origins of the suppression of the rf-induced loss has a similar origin to that described by Julienne *et al.* for spin exchange. This chapter explores this origin by adopting the adiabatic picture used by Julienne *et al.* [180] to recreate their results for ^{87}Rb, and applies the model to rf-dressed collisions.

4.1 Adiabatic model of rf-Free Collisions

In the adiabatic model a Hamiltonian is diagonalised over a grid of internuclear distances, R, to obtain a set of adiabats. In the case of rf-free collisions between

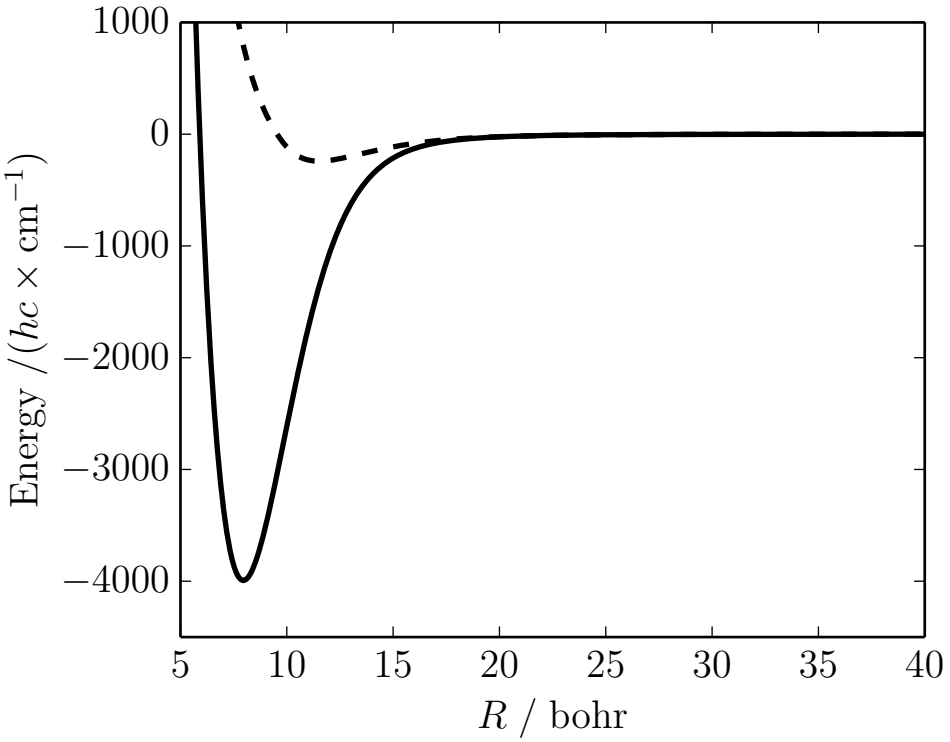

Figure 4.1: Singlet (black) and triplet (blue) potential curves provided by Strauss *et al.* [172]

alkali-metal atoms the Hamiltonian is written

$$\frac{\hbar^2}{2\mu}\left[R^{-1}\frac{d^2}{dR^2}R + \frac{\hat{L}}{R^2}\right] + \hat{V}(R) + \hat{h}_1 + \hat{h}_2. \tag{4.1.1}$$

The resulting adiabats are dependent upon the singlet and triplet potential curves contained within $\hat{V}(R)$, which for rubidium were provided by Strauss *et al.* [172]. These curves, shown in Fig. 4.1, are parallel at large R, but at distance $R_{\mathrm{X}}^{\mathrm{hf}} \approx 22$ bohr the exchange splitting between the singlet and triplet curves becomes comparable to the hyperfine splitting of ^{87}Rb (6.83 GHz) and the curves become separate when $R < R_{\mathrm{X}}^{\mathrm{hf}}$. Outside $R_{\mathrm{X}}^{\mathrm{hf}}$ the adiabats obtained from diagonalising Eq. 4.1.1 are well defined by atomic quantum numbers (f, m_f), and inside this distance they have the character of pure singlet or triplet states described by electronic spin $s = 0$ or 1, respectively.

Julienne *et al.* [180] considered collisions of ^{87}Rb atoms occupying different hyperfine states in the absence of external fields; a coupled basis set where f_1 and f_2

are coupled to give a resultant F was used. For $(f_1, f_2) = (1, 2)$, F may take a value of 1, 2 or 3. Of these $F = 2$ is the most important for considering non-adiabatic couplings as both $F = 1$ and $F = 3$ are forbidden by boson symmetry for $(1, 1)$ and $(2, 2)$. With $F = 2$ in zero magnetic field there are three adiabats to consider, described asymptotically with quantum numbers $(f_1, f_1, F) = (1, 1, 2)$, $(1, 2, 2)$ and $(2, 2, 2)$; these are shown Fig. 4.2 (a) relative to the energy of the pure triplet curve of Fig. 4.1. It can be seen that all three curves go through a transition around $R = R_{\mathrm{X}}^{\mathrm{hf}} = 22$ bohr, with the adiabats that asymptotically correspond to (1,2,2) and (2,2,2) becoming essentially pure triplet states at short range, whilst (1,1,2) becomes pure singlet in character at short range.

Nonadiabatic couplings between the adiabats shown in Fig. 4.2(a) control the inelastic loss rate. The nonadiabatic matrix elements

$$\left\langle i \left| \frac{d}{dR} \right| j \right\rangle \tag{4.1.2}$$

between the states (1,1,2), (1,2,2) and (2,2,2) are shown in Fig. 4.2(b). All three couplings peak around $R_{\mathrm{X}}^{\mathrm{hf}}$. The largest nonadiabatic coupling peaks at 0.41 bohr^{-1} between the states $(1, 2, 2) \leftrightarrow (1, 1, 2)$. The overall magnitude is more usefully characterized by the integral

$$D_{ij} = \int \left\langle i \left| \frac{d}{dR} \right| j \right\rangle dR, \tag{4.1.3}$$

which is $\pi/2$ for a complete avoided crossing, and 1.05, 0.55 and 0.49 for the couplings between $(1, 2, 2) \leftrightarrow (1, 1, 2)$, $(1, 2, 2) \leftrightarrow (2, 2, 2)$ and $(1, 1, 2) \leftrightarrow (2, 2, 2)$, respectively.

The adiabats and nonadiabatic couplings are independent of the singlet and triplet scattering lengths. However, Julienne *et al.* [180] argued that, when $a_{\mathrm{s}} \approx a_{\mathrm{t}}$, the radial wavefunctions $R^{-1}\chi_i(R)$ and $R^{-1}\chi_j(R)$ in the incoming (1,2,2) and inelastic outgoing (1,1,2) channels are in phase around $R_{\mathrm{X}}^{\mathrm{hf}}$. This minimises the matrix element that controls inelastic scattering,

$$-\frac{\hbar^2}{2\mu} \int \chi_i(R)^* \left\langle i \left| \frac{d}{dR} \right| j \right\rangle \frac{d}{dR} \chi_j(R)\, dR. \tag{4.1.4}$$

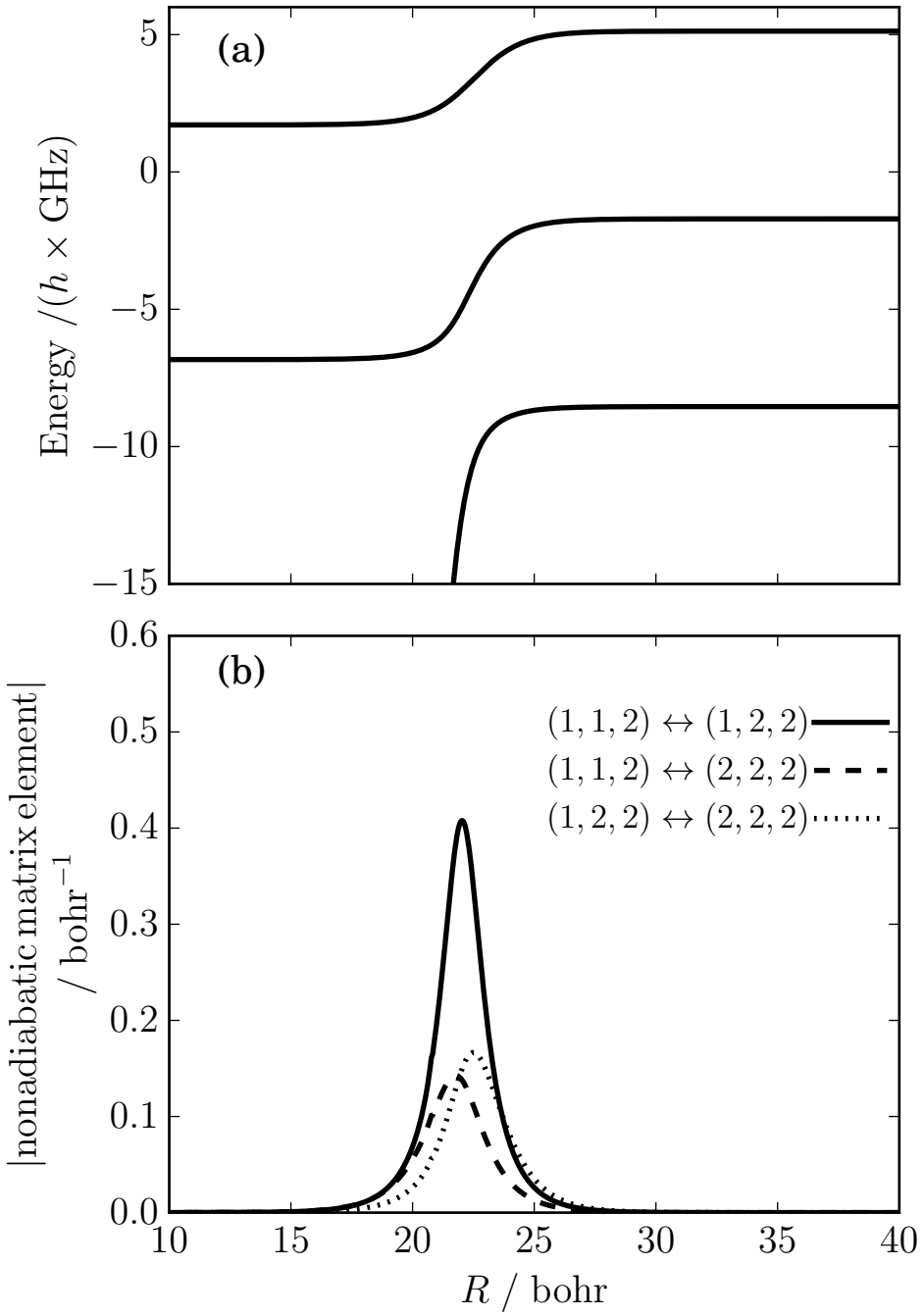

Figure 4.2: (a) Adiabats (eigenvalues of the Hamiltonian of Eq. 4.1.1 at fixed R) with respect to a pure triplet curve for field-free collisions with $(f_1, f_2, F = 2)$; (b) nonadiabatic matrix elements between (1,1,2), (1,2,2) and (2,2,2) in (a).

The singlet and triplet scattering lengths are near identical in ^{87}Rb ($a_{\rm s} \approx 90$ bohr, $a_{\rm t} \approx 99$ bohr), and the inelastic spin-exchange loss rate is supressed by this minimisation. Since rf-induced inelastic loss is also subject to the overlap of these radial wavefunctions this adiabatic approach will be adopted in the rf-dressed case.

4.2 Adiabatic Model of rf-Dressed Collisions

4.2.1 Collision of ^{87}Rb

To capture the effects of the rf dressing, terms for the rf field and atom-rf interactions are added to Hamiltonian 4.1.1 to give the rf-dressed Hamiltonian

$$\frac{\hbar^2}{2\mu}\left[R^{-1}\frac{d^2}{dR^2}R + \frac{\hat{L}}{R^2}\right] + \hat{V}(R) + \hat{h}_1 + \hat{h}_2 + \hat{h}^{\rm int}_{\rm rf,a} + \hat{h}^{\rm int}_{\rm rf,b} + \hat{h}_{\rm rf}, \tag{4.2.5}$$

where $\hat{h}^{\rm int}_{\rm rf,a/b}$ and $\hat{h}_{\rm rf}$ are the atom-rf field interaction hamiltonians and rf field hamiltonian given by Eqs 1.5.41 and 1.5.42, respectively. The adiabats for a pair of $f = 1$ ^{87}Rb atoms with $M_{\rm tot} = 0$ in an rf-dressed trap, obtained from diagonalising Eq. 4.2.5 at the trap centre (4.27 G) using a σ_- polarised rf field with $\nu = 3.0$ MHz, $B_{\rm rf} = 0.5$ G and $|N_{\rm max}| = 2$, are shown in Fig. 4.3(a). Comparing the two sets of adiabats in Figs. 4.2(a) and 4.3(a), it can be seen that for each rf-free adiabat in Fig. 4.2(a), a *set* of adiabats exists in the rf-dressed case, split by energy $h \times B_{\rm rf} g_F \mu_{\rm B} = 0.35$ MHz at $R > R_{\rm X}$. The lowest set of rf-dressed adiabats that are similar in character to the $(f_1, f_2, F) = (1, 1, 2)$ rf-free adiabat at $R > R^{\rm hf}_{\rm X}$ is comprised of 6 rf-dressed adiabats. At $R >> R^{\rm hf}_{\rm X}$ these are essentially the rf-dressed collision thresholds described in the previous chapter. Fig. 4.4 shows this set of adiabats in more detail.

The nonadiabatic matrix elements 4.1.2 between the two uppermost adiabats of the six $(f_1, f_2, M_{\rm tot}) = (1, 1, 0)$ states for rf-dressed ^{87}Rb are shown in Fig. 4.3(b). Comparing these to the rf-free matrix elements shown in Fig. 4.2(b), the nonadiabatic matrix element again peaks near 22 bohr, but has a larger integral $D_{ij} = 1.571$. The slight shift in energy due to the rf dressing means the positions of the peaks with and without rf do not line up exactly. The matrix element in the rf-dressed

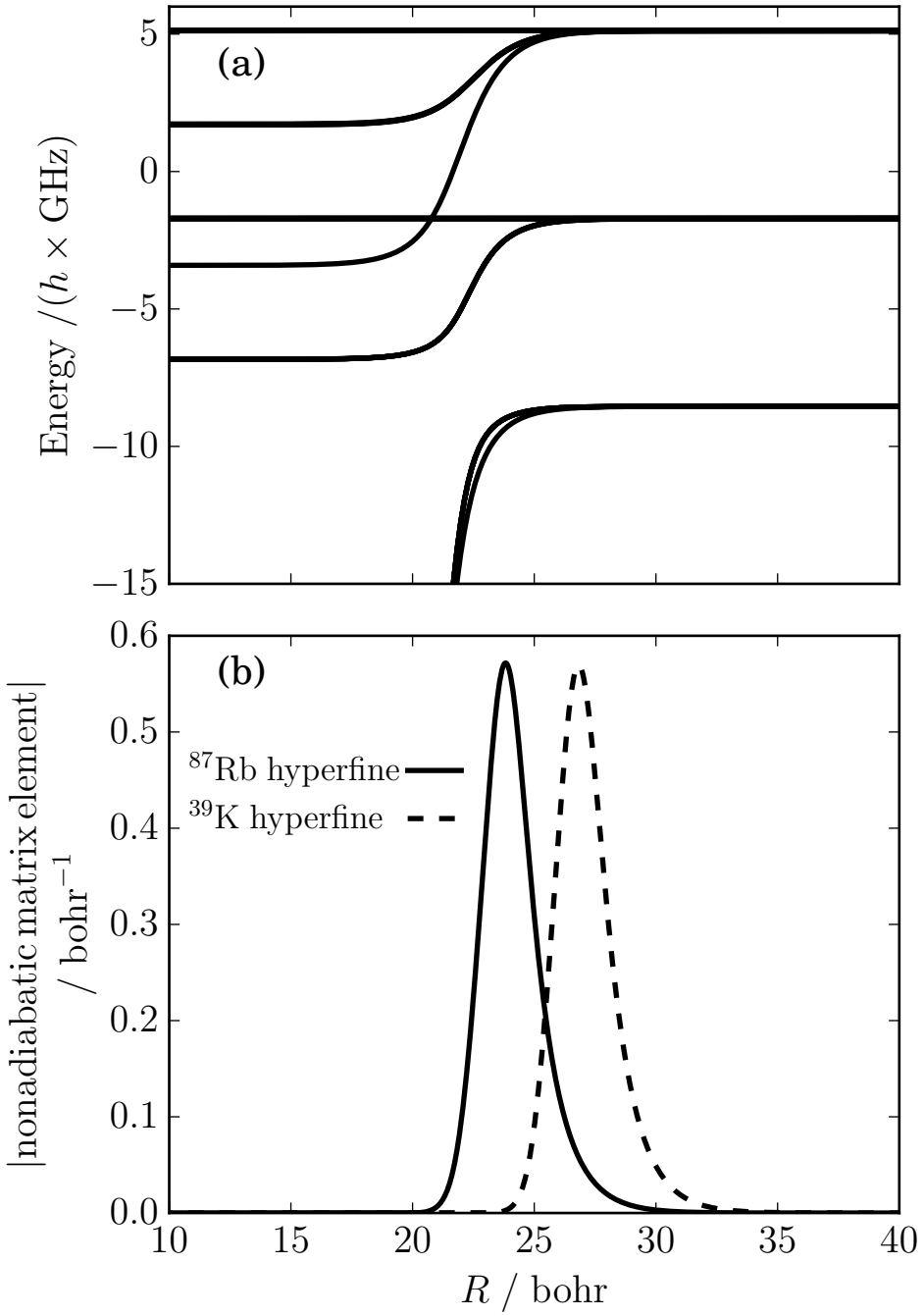

Figure 4.3: (a) Adiabats with respect to a pure triplet curve for collisions of rf-dressed atoms with $f = 1$, at the trap center with rf field frequency 3 MHz and strength $B_{\mathrm{rf}} = 0.5\,\mathrm{G}$, for $M_{\mathrm{tot}} = 0$; (b) nonadiabatic matrix element between the uppermost of the six $(f_1, f_2, M_{\mathrm{tot}}) = (1, 1, 0)$ rf-dressed states and the next-highest state.

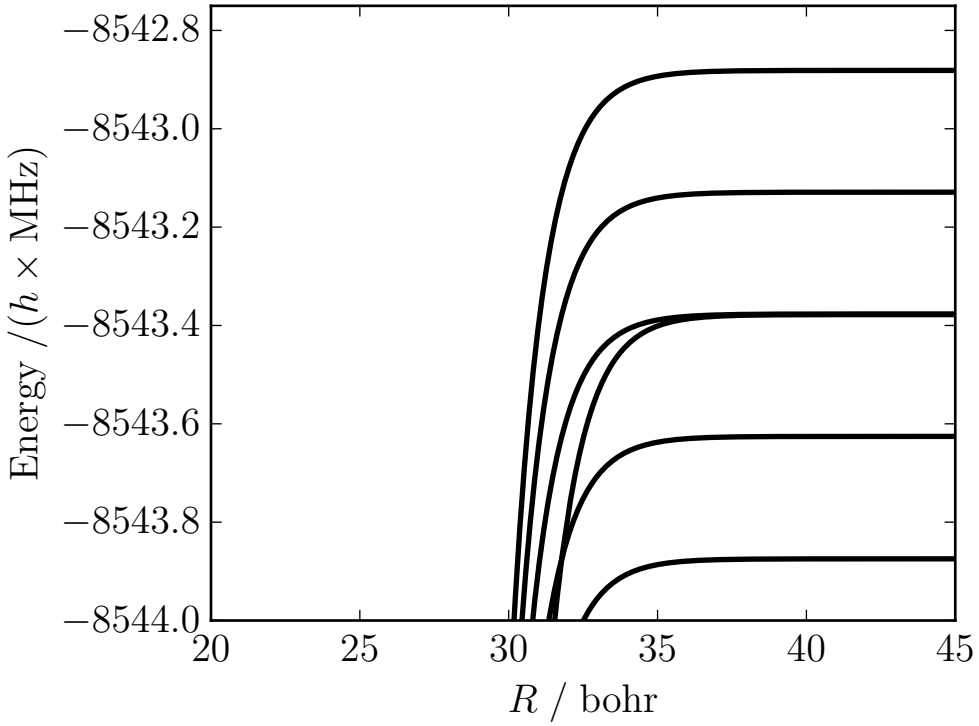

Figure 4.4: Zoomed in picture of the lowest set of adiabats in Fig. 4.3(a).

case is also not symmetric, showing a small tail on the right-hand side due to the influence of adiabats that go to higher hyperfine states at large R. Because the rf-dressed nonadiabatic matrix element peaks near $R_{\rm X}^{\rm hf}$, the rf-induced inelastic loss rate is minimised in a similar fasion to spin exchange; the overall inelastic coupling is minimised when $a_{\rm s} = a_{\rm t}$, producing the diagonal troughs seen in the contour plots of the previous chapter. Fig. 4.3(b) also shows matrix elements for ^{87}Rb atoms modified to have the hyperfine splitting of ^{39}K. The peak shifts to 27 bohr, reflecting the smaller hyperfine splitting of ^{39}K, with similar integral D_{ij} =1.563. Since $a_{\rm s} \neq a_{\rm t}$ in this case, the overall matrix element 4.1.4 is not minimised as the radial wavefunctions are not in phase at $R_{\rm X}^{\rm hf}$.

For collisions between two ^{87}Rb atoms in their upper hyperfine state with $f = 2$, inelasticity is again dominated by $F = 2$; the adiabats corresponding to $(f_1, f_2, F) = (2, 2, 2)$ are shown by the highest-energy adiabat in Fig. 4.2 (a). For two rf-dressed atoms with $f = 2$, $|N_{\rm max}| = 4$ is required to capture the effects of all possible $M_{\rm tot} = 0$ states. This leads to the set of 15 rf-dressed adiabats displayed in Fig. 4.5(a) at the trap centre. The rf field used here has the same parameters as the

$f = 1$ case, but σ_+ polarisation is required.

It is notable that the rf-induced loss rate for $f = 2$ (3.34×10^{-15} cm^3 s^{-1}) is about two orders of magnitude lower than the rf-free spin-exchange rates for $(f_1, m_{f,1}) + (f_2, m_{f,2}) = (2, 0) + (2, 0)$ and (2,1)+(2,−1) collisions, which are 1.73×10^{-13} and 1.25×10^{-13} cm^3 s^{-1} respectively. This is true even though the wavefunction for the rf-dressed atomic state includes substantial amounts of (2,0) and (2,1) near the trap center. This can be rationalized by considering the adiabatic curves of Fig. 4.5(a). Fig. 4.5(b) shows the corresponding nonadiabatic matrix elements between the uppermost and next-highest state. The nonadiabatic coupling is quite different from the previous cases: there is no feature around 22 bohr, and instead the matrix element peaks around a value $R_{\rm X}^{\rm rf} = 32$ bohr, where the difference between the singlet and triplet curves is comparable with the splittings $\Delta_{\rm rf}$ due to the rf dressing. The coupling is far weaker than in the cases shown in Fig. 4.2. The integral D_{ij} over the nonadiabatic coupling is only 1.96×10^{-6}, compared to 1.57 between the top two states in the rf-dressed $f = 1$ case and $\pi/2$ for a completed avoided crossing. This difference in D_{ij} due to the different coupling mechanism is reflected in the heights of the resonant peaks of the $f = 1$ and $f = 2$ contour plots of the previous chapter. The maximum peak heights were about 10^{-10} and 10^{-13} cm^3 s^{-1} for the rf-dressed $f = 1$ and $f = 2$ atoms, respectively.

More insight into the effect of the hyperfine splitting can be gained by considering the nonadiabatic transitions in ^{39}K with $f = 2$. The adiabats for ^{39}K are similar to those shown for ^{87}Rb in Fig. 4.5(a). However, the nonadiabatic matrix element, shown in Fig. 4.5(c), is approximately a factor of 200 larger than for ^{87}Rb, with integral $D_{ij} = 3.8 \times 10^{-4}$. The nonadiabatic matrix element reflects the amount of singlet character in the wavefunction of the rf-dressed atomic pair at long range; this in turn depends on the degree of mixing of $f = 1$ and $f = 2$ states in the magnetic field, which increases as the hyperfine splitting decreases.

4.2.2 Collisions of ^{85}Rb

The rf-induced loss rate of ^{85}Rb in its hyperfine ground state with $f = 2$ is 3.34×10^{-15} cm^3 s^{-1}, five orders of magnitude larger than that for ^{87}Rb in its hyperfine

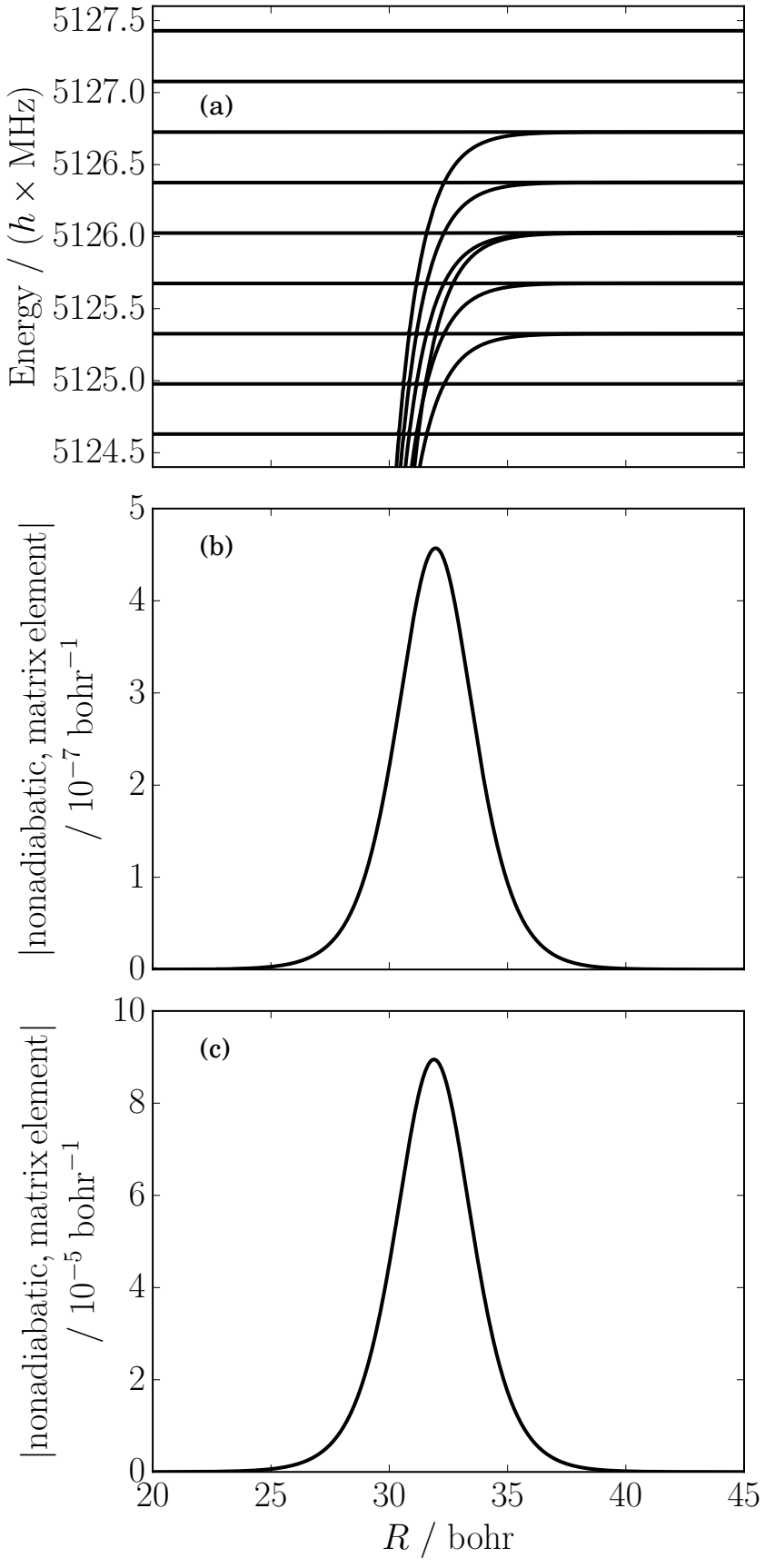

Figure 4.5: (a) Adiabats for collisions of field-dressed ^{87}Rb atoms in $f = 2$ states, with respect to a pure triplet curve, for $M_{\mathrm{tot}} = 0$. (b) nonadiabatic matrix elements between the top two adiabatic states for ^{87}Rb. (c) nonadiabatic matrix elements between the top two adiabatic states with the hyperfine splitting reduced to the value for ^{39}K.

ground state with $f = 1$ (1.25×10^{-20} cm^3 s^{-1}); since $a_s \neq a_t$ for ^{85}Rb ($a_s \approx 2560$ bohr, $a_t \approx -380$ bohr) there is no suppression of inelastic loss. The mechanism for rf-induced loss is the same for the two cases, and so a peak in the nonadiabatic matrix element between the two highest adiabats for rf-dressed collisions of $(f_1, f_2) = (2, 2)$ is expected near R_X^{hf}, which is larger due to the smaller hyperfine splitting of ^{85}Rb (3.04 GHz). The shift in R_X^{hf} can be seen in rf-free collisions, the adiabats associated nonadiabatic matrix elements can be seen in Fig. 4.6(a) and (b), respectively. Because f may take values of 2 or 3 for ^{85}Rb, there is an increase in the number of adiabats to consider. The values of $F = f_1 + f_2$ that are most important to inelastic loss are $F = 2$ and 4. All the nonadiabatic matrix elements peak near $R = 23$ bohr with integrals ranging from 1.15 for $(f_1, f_2, F) = (2, 2, 4) \leftrightarrow (2, 3, 4)$ to 0.38 for $(2, 2, 4) \leftrightarrow (3, 3, 4)$.

Fig. 4.7(a) shows the adiabats for a pair of ^{85}Rb atoms at the centre of an rf-dressed trap with σ_+ polarisation, $\nu = 3.0$ MHz, $B_{rf} = 0.5$ G and $|N_{max}| = 4$. As with ^{87}Rb we obtain three distinct sets of rf-dressed adiabats at long range; Fig. 4.8 shows the lowest set which correspond to $(f_1, f_2) = (2, 2)$ in more detail. The nonadiabatic matrix element between the top adiabat and the next highest of this set peaks at $R = 25$ bohr, and is shown in Fig. 4.7(b). As for ^{87}Rb this is close to the value of R_X^{hf}, but the integral 4.1.3 has a greater magnitude with $D_{ij} = 2.23$ due to the contributions from an additional value of F. The integral is also larger than $\pi/2$ for a complete avoided crossing but, as with ^{87}Rb, this also incorporates the influence of adiabats that go to higher hyperfine states at large R.

The rf-dressed adiabats and nonadiabatic matrix elements for rf-dressed ^{85}Rb in its upper hyperfine state with $f = 3$ are shown in Fig. 4.9. The nonadiabatic matrix element peaks around $R_X^{rf} = 32$ bohr as with ^{87}Rb in its upper hyperfine state, where the exchange splitting is equal to the splittings induced by the rf field, Δ_{rf}. Since the rf field parameters are unchanged this happens around the same value of R. The integral $D_{ij} = 2.96 \times 10^{-5}$ is about 15 times larger than for ^{87}Rb in its upper hyperfine state, again highlighting the influence of the hyperfine splitting on the rf-dressed loss from upper hyperfine states; the hyperfine splitting of ^{85}Rb (3.04 GHz) lies closer to ^{87}Rb (6.83 GHz) than ^{39}K (461.72 MHz). The difference in D_{ij}

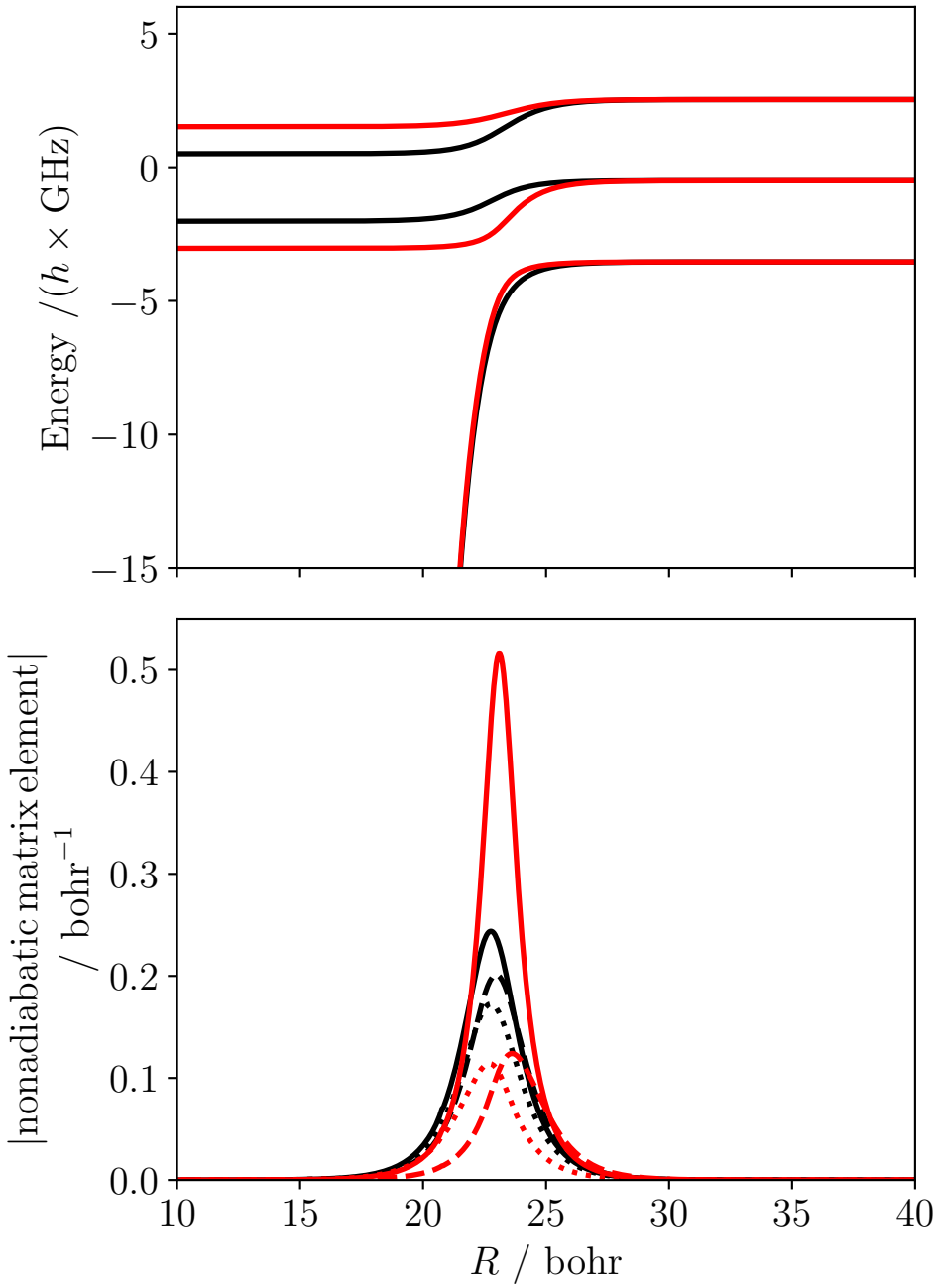

Figure 4.6: (a) Adiabats for a pair of ^{85}Rb atoms with respect to a pure triplet curve for field-free collisions with $F = 2$ (black) and $F = 4$ (red); (b) nonadiabatic matrix elements $(f_1, f_2) = (2, 2) \leftrightarrow (2, 3)$ (solid), $(2, 2) \leftrightarrow (3, 3)$ (dotted) and $(2, 3) \leftrightarrow (3, 3)$ (dashed) for both values of F in (a).

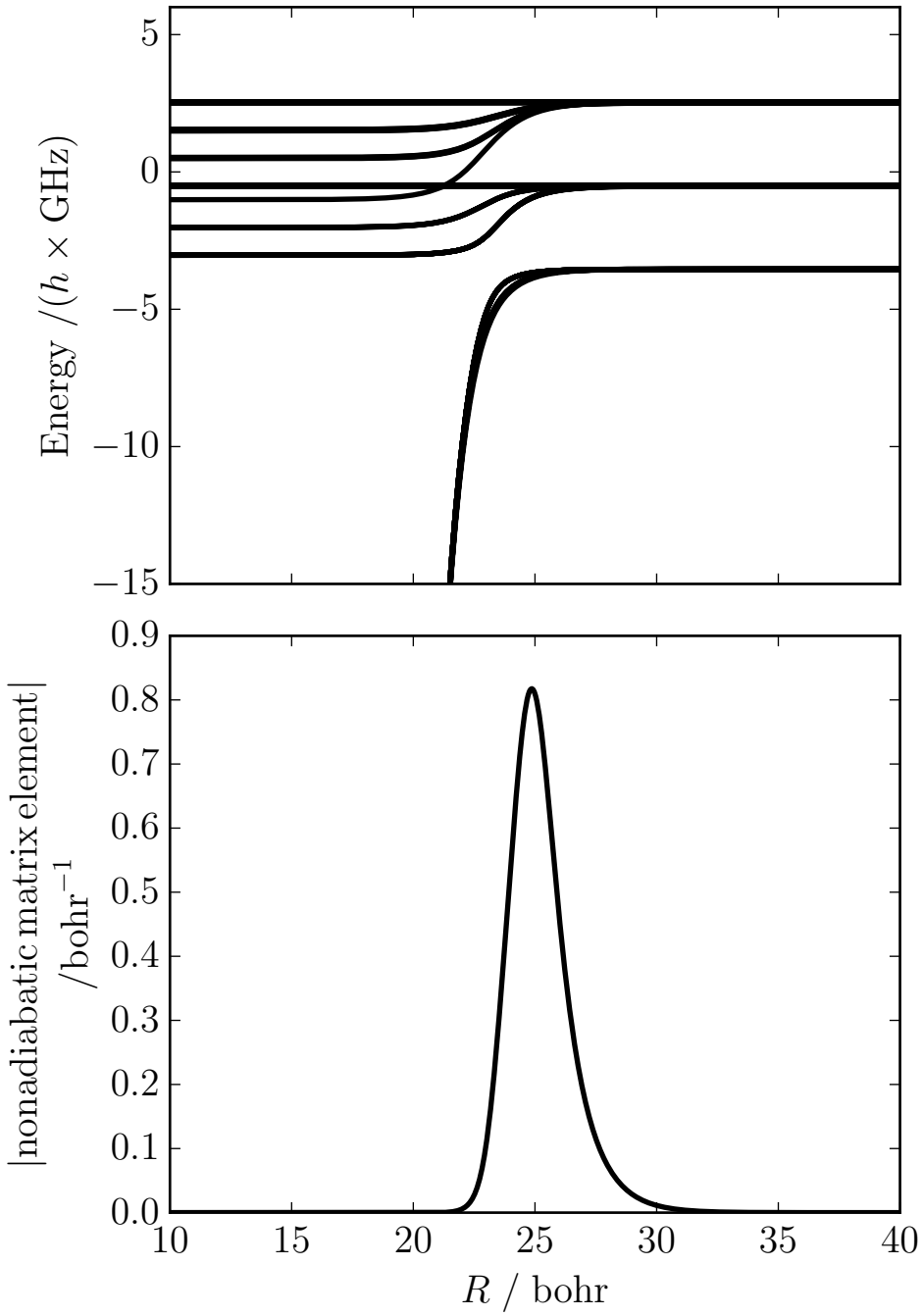

Figure 4.7: (a) Adiabats for collisions of field-dressed ^{85}Rb atoms in $f = 2$ states, with respect to a pure triplet curve, for $M_{\text{tot}} = 0$ at the trap centre with $B = 6.42$ G. (b) nonadiabatic matrix elements between the top two adiabatic states for ^{85}Rb.

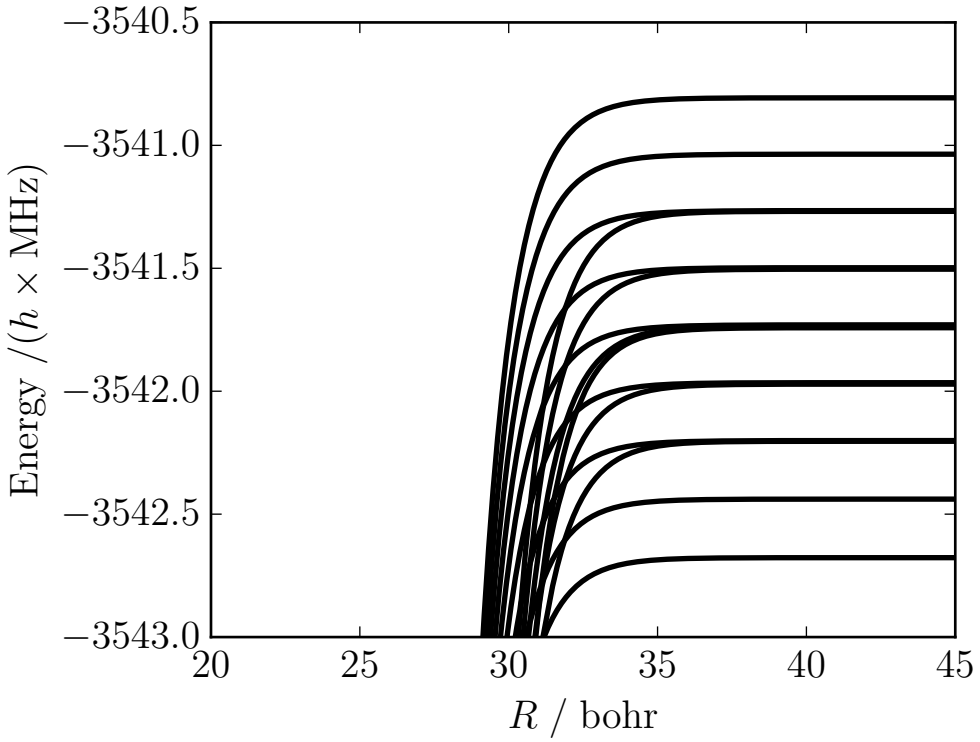

Figure 4.8: Zoomed in picture of the lowest set of adiabats in Fig. 4.7(a).

between ^{85}Rb and ^{87}Rb here is reflected in the resonant peak heights in the contour plots of the previous chapter; in the ^{85}Rb case the peaks are an order of magnitude higher.

4.2.3 Collisions of ^{87}Rb + ^{85}Rb

The previous chapter identified a spin-exchange-dominated inelastic loss for rf-dressed ^{87}Rb + ^{85}Rb that was three orders of magnitude faster than the quickest rf-induced loss in previously considered homonuclear systems with the same rf field parameters. There are two trap centres in the rf-dressed heteronuclear case (one for each atom); the nonadiabatic couplings between the top two adiabats at these respective magnetic fields may exhibit differences from previous cases as the untrapped atom is in a well defined state.

For rf-free collisions between ^{87}Rb and ^{85}Rb there are more values of F that can contribute to inelasticity compared to previous cases due to the lack of boson symmetry. $F = 2$ and 3 will contribute most to inelastic collisions, and are shown in

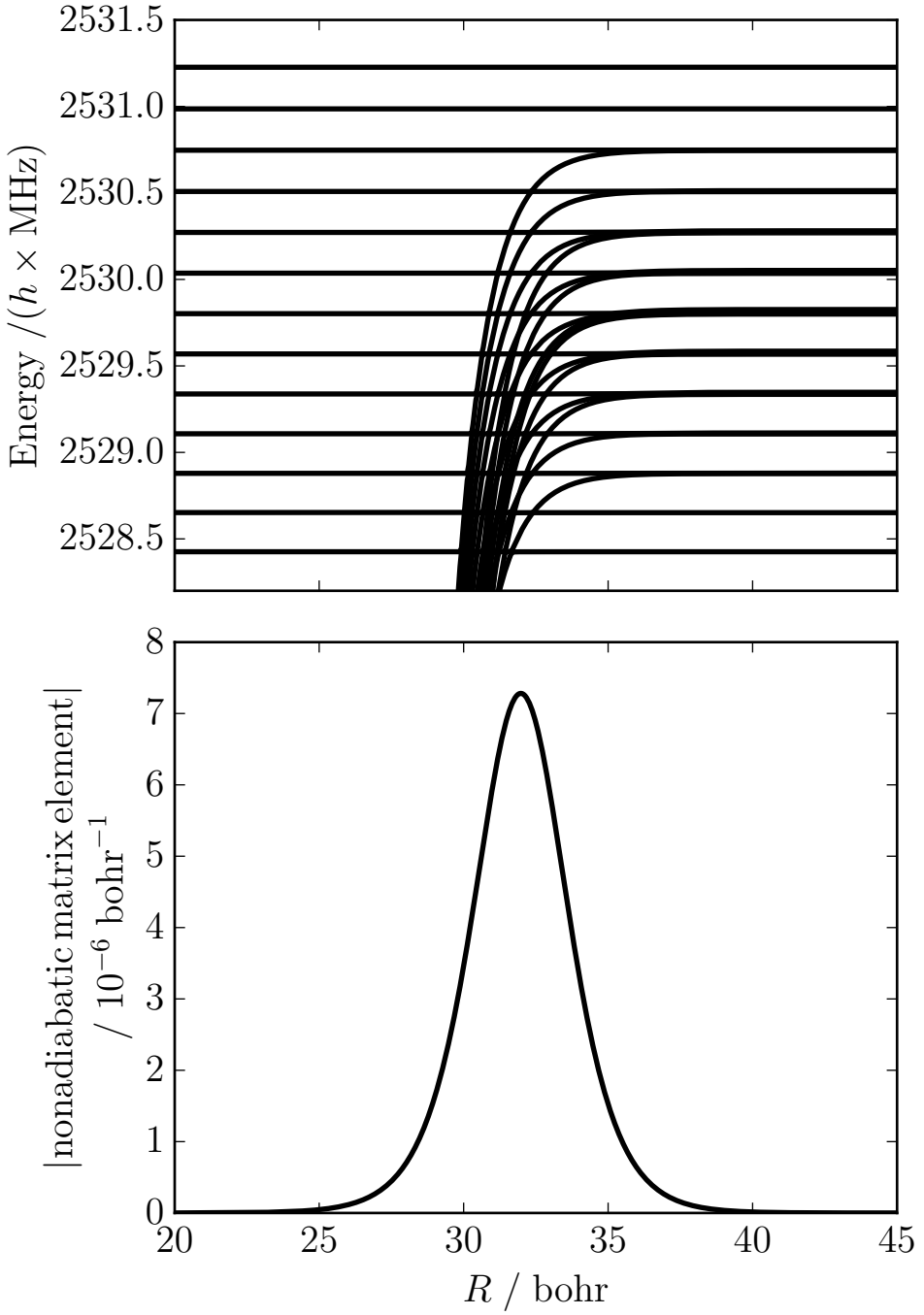

Figure 4.9: (a) Adiabats for collisions of field-dressed ^{85}Rb atoms in $f = 3$ states, with respect to a pure triplet curve, for $M_{\rm tot} = 0$ at the trap centre with $B = 6.42$ G. (b) nonadiabatic matrix elements between the top two adiabatic states for ^{85}Rb.

Fig. 4.10(a). The nonadiabatic matrix elements depicted in Fig. 4.10(b) are between the two lowest adiabats for $F = 2$ and 3, and peak near 22.5 bohr, in between the values of $R_{\rm X}^{\rm hf} = 22$ and 23 bohr for ^{87}Rb and ^{85}Rb, respectively. The magnitudes of D_{ij} of these matrix elements are comparable to those between the equivalent matrix elements in ^{87}Rb and ^{85}Rb, with $D_{ij} = 0.65$ and 0.98 for $F = 2$ and 3, respectively. Overall the mechanism for inelastic loss is unchanged in the rf-free heteronuclear case, and as with ^{85}Rb there is no suppression of spin-exchange as $a_{\rm s} \neq a_{\rm t}$.

Fig. 4.11 shows the rf-dressed adiabats and nonadiabatic matrix elements between the top two adiabats of rf-dressed $(f_{87}, f_{85}) = (1, 2)$ at a magnetic field strength of 4.27 G, where ^{87}Rb is trapped. There are two distinct peaks in the nonadiabatic matrix element at 23.5 bohr and 31 bohr where the exchange splitting is equal to the hyperfine splitting of ^{87}Rb and rf-dressed splitting, respectively. A similar pattern in the nonadaibatic matrix element is apparent at a magnetic field of 6.24 G, shown in Fig. 4.12, where the left peak is shifted to 24 bohr, closer to $R_{\rm X,85}^{\rm hf}$, and the position of the right peak is unchanged. The spacing of the adiabats in Fig. 4.12(a) is also more apparent, with three distinct sets of adiabats corresponding to $m_{f,87} = 1$, 0 and -1 from top to bottom; there are five sets of adiabats that are difficult to distinguish in Fig. 4.11(a) corresponding to $m_{f,85} = 2$, 1, 0, -1 and -2 from top to bottom.

The matrix elements of Fig. 4.11 and 4.12 further highlight the differences between the nonadiabatic couplings of the two atoms in their respective traps. The right-hand peak has the same origin as those of ^{87}Rb and ^{85}Rb in their upper hyperfine states. The integrals of these rf-induced peaks at 30.5 bohr are of similar magnitude with D_{ij}= 0.71 and 0.94 for Fig. 4.11 and Fig. 4.12, respectively, which indicates this coupling is similar for each atom; only the magnetic field strength is changed between the two matrix elements and the rf coupling is controlled by the dipoles of the atoms. These integrals are 5 and 6 orders of magnitude larger than for ^{85}Rb and ^{87}Rb in their upper hyperfine states, respectively, indicating that this coupling is playing a greater role here.

The left-hand peaks show nonadiabatic couplings similar to the collisions of rf-dressed ground state atoms, where the matrix element peaks near $R_{\rm X}^{\rm hf}$. There

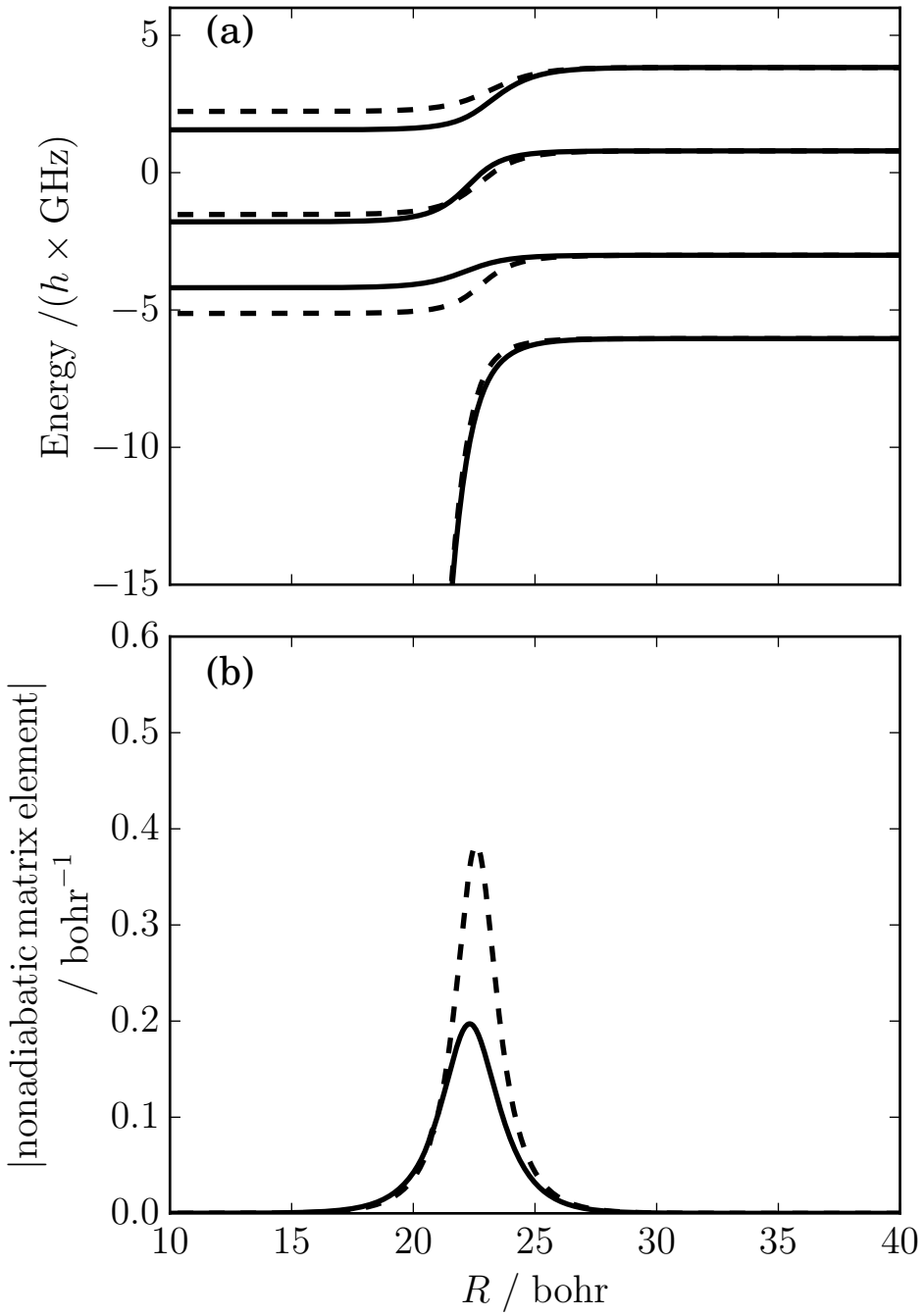

Figure 4.10: (a) Adiabats with $F = 2$ (solid black) and 3 (dashed black) for collisions of ^{85}Rb and ^{87}Rb atoms with respect to a pure triplet curve. (b) Nonadiabatic matrix elements between the two lowest adiabats for $F = 2$ (solid black) and $F = 3$ (dashed black) in panel (a)

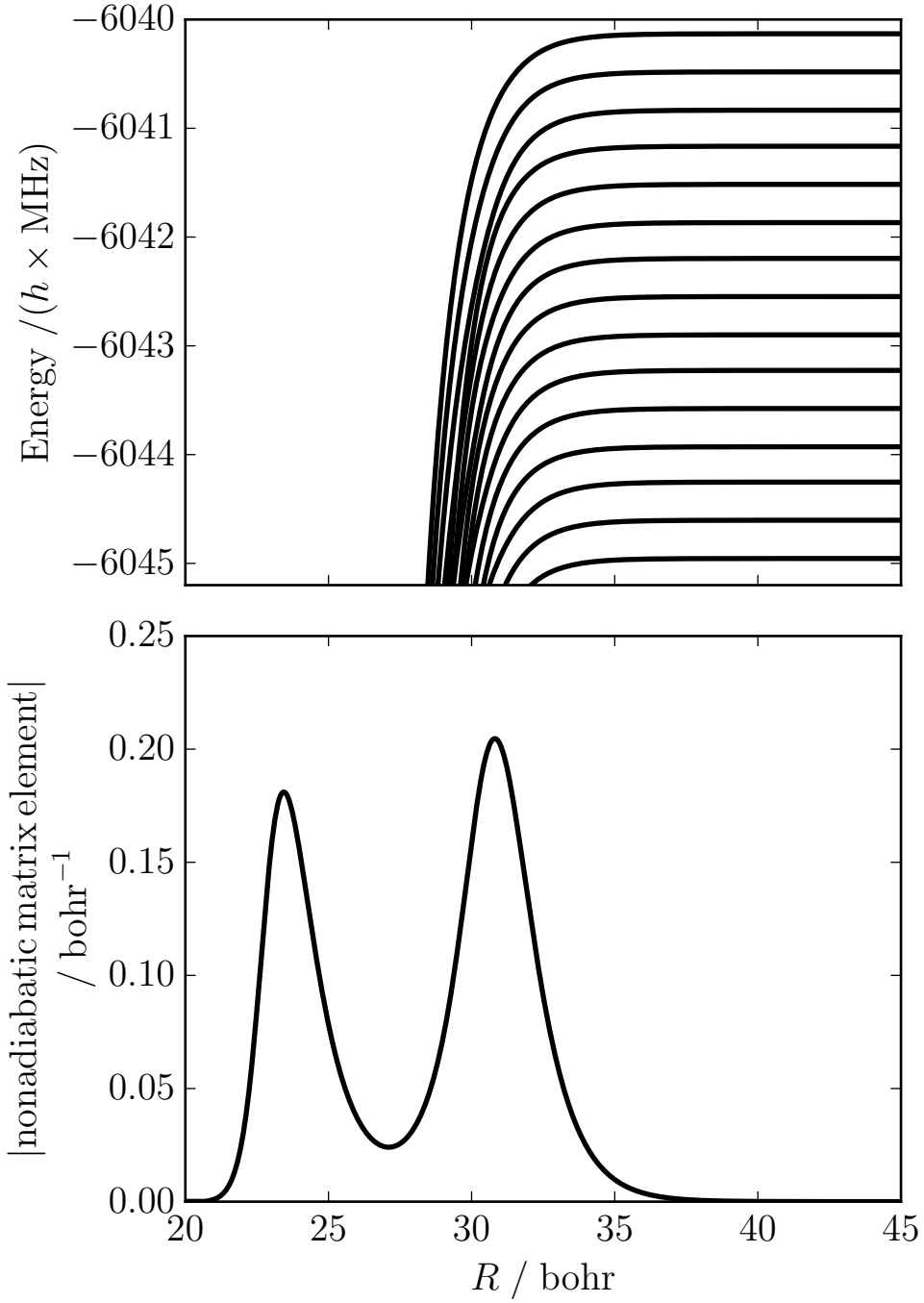

Figure 4.11: (a) Adiabats for rf-dressed collisions of ^{85}Rb and ^{87}Rb atoms with $(f_{87}, f_{85}) = (1, 2)$ at the trap centre for ^{87}Rb (4.27 G) with respect to a pure triplet curve. (b) Nonadiabatic matrix elements between the two highest adiabats in panel (a)

is a large difference in the integrals of these two peaks at each trap centre, with $D_{ij} = 0.47$ and 3.19 for Fig. 4.11 and Fig. 4.12, respectively, indicating that the nonadiabatic couplings in the collision when ^{85}Rb is trapped are dominated by this mechanism.

4.2.4 Conclusions

The adiabatic picture of rf-dressed collisions confirms that the mechanism that suppresses inelastic loss depends on relative phase of the wavefunctions in the incoming and outgoing inelastic channels, which can be gauged by the relative values of a_{s} and a_{t}. For rf-dressed atoms in their hyperfine ground state, the nonadiabatic matrix elements peak near $R_{\mathrm{X}}^{\mathrm{hf}}$; if $a_{\mathrm{s}} = a_{\mathrm{t}}$ the overall matrix element Eq. 4.1.4 that controls the inelastic loss rate is minimised as χ_i and χ_j are in phase at R_{X}. This is the case for ^{87}Rb, leading to rf-dressed loss rates many orders of magnitude slower than for other alkali-metal atoms.

The nonadiabatic couplings are different for atoms in their upper hyperfine states, they peak at an internuclear distance $R_{\mathrm{X}}^{\mathrm{rf}}$ where the exchange splitting is comparable to the splitting of the rf-dressed states at the trap centre, Δ_{rf}. Since χ_i and χ_j acquire no further phase beyond $R_{\mathrm{X}}^{\mathrm{rf}}$, the same suppression of the inelastic loss rate in ^{87}Rb still exists, but the heights of resonant peaks in the contour plots showing the loss rate as a function of a_{s} and a_{t} are proportional to the integral D_{ij} of this nonadiabatic matrix element. The magnitude of these matrix elements is inversely proportional to the hyperfine splitting of the trapped atoms; a smaller hyperfine splitting leads to more singlet character in the long-range wavefunction of the atomic pair and thus a larger nonadiabatic matrix element.

In a heteronuclear collision dressed with rf radiation, the nonadiabatic couplings show differences depending on what atom is trapped during the collision. For ^{85}Rb + ^{87}Rb the nonadiabatic matrix element peaks at both $R_{\mathrm{X}}^{\mathrm{hf}}$ and $R_{\mathrm{X}}^{\mathrm{rf}}$, but the largest peak differed for each atom in their respective traps.

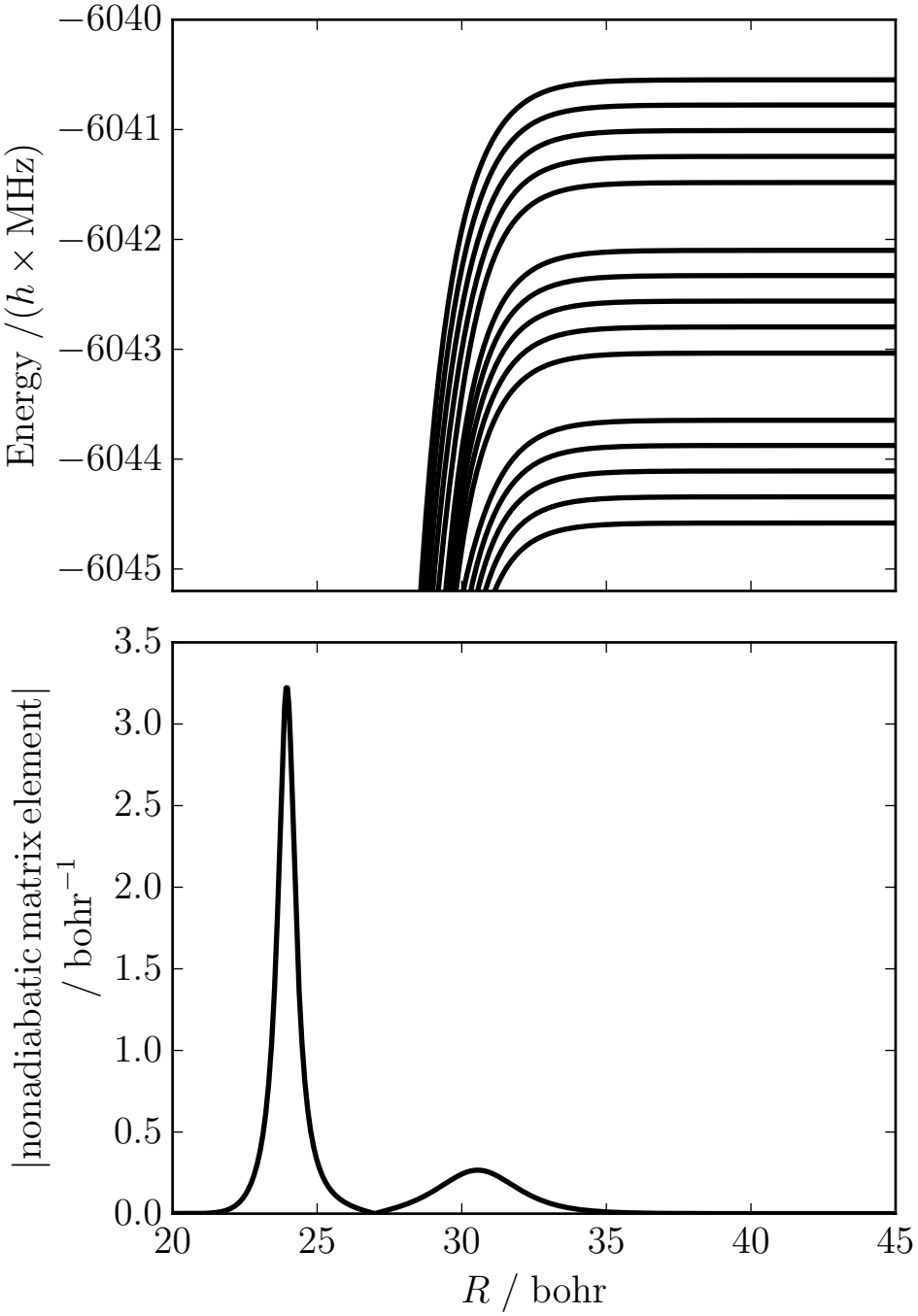

Figure 4.12: (a) Adiabats for rf-dressed collisions of ^{85}Rb and ^{87}Rb atoms with $(f_{87}, f_{85}) = (1, 2)$ at the trap centre for ^{85}Rb (6.42 G) with respect to a pure triplet curve. (b) Nonadiabatic matrix elements between the two highest adiabats in panel (a)

Chapter 5

Conclusions and Future Work

This thesis has investigated the scattering properties of ultracold atoms dressed with rf radiation. Coupled-channel calculations were performed in a photon-dressed basis set; the couplings induced by the rf field were implemented using a dressed-state picture in which a photon number, N, and associated angular momentum projection, M_N, were combined with electronic and nuclear spin functions (s, m_s) and (i, m_i), respectively, in an uncoupled basis set.

Chapter 2 explored the creation of rf-induced Feshbach resonances in the context of solving the *one field problem* of ultracold molecule formation. The chapter focused on zero-energy Feshbach resonances in the heteronuclear system ^{39}KCs, where no suitable resonances exist at magnetic fields where caesium can be cooled to degeneracy. It was shown that a Feshbach resonance could be created using circularly polarised σ_+ rf radiation; a frequency of $\nu = 79.9$ MHz was chosen to couple the incoming ground-state atoms with total angular momentum projection $M_F = 4$ to a molecular bound state with $M_F = 3$ at a magnetic field strength of around 21 G. The molecules formed across this rf-induced Feshbach resonance have long lifetimes $\tau > 180$ ms. The widths of the induced resonances increase quadratically with the strength of the rf field; an amplitude of 4 G is required to induce a resonance of width on the order of 1 mG. Only one type of rf-induced Feshbach resonance was explored in this work, exploration of other polarisations can be envisaged. For example, inducing Feshbach resonances using an rf field with linear π polarisation would allow the formation of molecules with the same M_F as the incoming atoms

at desired magnetic fields.

Chapter 3 investigated collisional losses in rf-dressed magnetic traps. Experiments involving rf-dressed traps typically use ^{87}Rb; whilst one-body nonadiabatic losses have been previously examined in detail in experiments and theoretical studies, two-body collisional losses have not. It was shown that ^{87}Rb is a special case for rf-induced collisional losses, and that these losses are much faster for other alkali metals. The dependence of the rf-induced loss rate on the singlet and triplet scattering lengths $a_{\rm s}$ and $a_{\rm t}$, respectively, was explored, and it was found that the rf-induced loss is minimised when $a_{\rm s} = a_{\rm t}$. Not only does ^{87}Rb have similar values for $a_{\rm s}$ and $a_{\rm t}$, but the values are such that the rf-induced loss receives no enhancement from any kind of resonance leading to a loss rate 6 orders of magnitude smaller compared to ^{39}K.

Collisional losses in a heteronuclear system were also analysed in chapter 3. For ^{87}Rb + ^{85}Rb in their respective hyperfine ground states, the rf-induced loss was found to be much faster than in any homonuclear case, with a rate comparable to rf-free spin exchange ($\sim 10^{-10}$ cm^3 s^{-1}). Due to the separation of the rf-dressed traps for the two atoms in magnetic field, the trapped state of the atomic pair is well defined at magnetic fields between the two traps, and undergoes rf-free spin exchange. The rf-induced loss approaches the rf-free spin exchange of $(m_{f,87}, m_{f,85}) = (-1, 2)$, where m_f is the total atomic angular momentum projection, as a function of decreasing rf intensity, indicating that there is suppression of spin exchange due to the rf dressing. It is predicted that spin exchange will be dominant for rf-dressed heteronuclear systems in which the Landé g-factors are different for the two species. It is possible to avoid such large losses by choosing one rf field frequency for each atom in the mixture, and tuning the frequencies such that the traps for the two atoms overlap. This possibility will require further work to investigate the collisional losses.

Finally, chapter 4 looked at collisions in an rf-dressed trap through the lens of an adiabatic model. The nonadiabatic matrix elements between adiabats of an rf-dressed atomic pair in their ground-states at the trap centre peaked at internuclear distance $R_{\rm X}^{\rm hf}$, where the exchange splitting between the singlet and triplet potential curves is comparable to the hyperfine splitting. When $a_{\rm s} = a_{\rm t}$ the incoming and

outgoing radial wavefunctions are in phase around $R_{\mathrm{X}}^{\mathrm{hf}}$ and this minimises the radial matrix element that controls inelastic processes. When rf-dressed atoms are in their upper hyperfine states the nonadiabatic matrix element peaks at $R_{\mathrm{X}}^{\mathrm{rf}}$, where the exchange splitting is comparable to the (much smaller) splitting induced by the rf radiation. The nonadiabatic effects here are orders of magnitude smaller compared to those for rf-dressed ground-state atoms. This is reflected by smaller resonant peaks in the rf-induced loss rate as a function of a_{s} and a_{t}, compared to those for rf-dressed atoms in their hyperfine ground states. In the heteronuclear case, peaks in the nonadiabatic matrix element were observed at both $R_{\mathrm{X}}^{\mathrm{hf}}$ and $R_{\mathrm{X}}^{\mathrm{rf}}$. The magnitudes of the nonadiabatic effects differed at each trap centre, the reason for which is an interesting open question to be investigated in future work.

Chapter 6

Bibliography

[1] H. K. Onnes, *Nobel lecture: Investigations into the properties of substances at low temperatures, which have led, amongst other things, to the preparation of liquid helium* (1913), in *Nobel Lectures, Physics 1901-1921* (Elsevier Publishing Company, Amsterdam, 1967).

[2] P. Kapitza, *Viscosity of liquid helium below the λ-point*, Nature 74 (1938).

[3] J. F. Allen and A. D. Misener, *Flow of liquid helium-ii*, Nature 75 (1938).

[4] M. H. Anderson, J. R. Ensher, M. R. Matthews, C. E. Wieman, and E. A. Cornell, *Observation of Bose-Einstein condensation in a dilute atomic vapor*, Science 269, 198 (1995).

[5] K. B. Davis, M.-O. Mewes, M. R. Andrews, N. J. van Druten, D. S. Durfee, D. M. Kurn, and W. Ketterle, *Bose-Einstein condensation in a gas of sodium atoms*, Phys. Rev. Lett. 75, 3969 (1995).

[6] E. A. Cornell and C. E. Wieman, *Nobel lecture: Bose-Einstein condensation in a dilute gas, the first 70 years and some recent experiments*, Rev. Mod. Phys. 74, 875 (2002).

[7] W. Ketterle, *Nobel lecture: When atoms behave as waves: Bose-Einstein condensation and the atom laser*, Rev. Mod. Phys. 74, 1131 (2002).

[8] S. N. Bose, *Plancks gesetz und lichtquantenhypothese*, Z. Phys. 26, 178 (1924).

[9] A. Einstein, *Quantum theory of the monatomic ideal gas*, Sitzungsber. Preuss. Akad. Wiss. page 18 (1925).

[10] B. DeMarco and D. S. Jin, *Onset of Fermi degeneracy in a trapped atomic gas*, Science 285, 1703 (1999).

[11] R. H. Fowler, *On dense matter*, Monthly Notices of the Royal Astronomical Society 87, 114 (1926).

[12] A. L. Migdall, J. V. Prodan, W. D. Phillips, T. H. Bergeman, and H. J. Metcalf, *1st observation of magnetically trapped neutral atoms*, Phys. Rev. Lett. 54, 2596 (1985).

[13] E. L. Raab, M. Prentiss, A. Cable, S. Chu, and D. E. Pritchard, *Trapping of neutral sodium atoms with radiation pressure*, Phys. Rev. Lett. 59, 2631 (1987).

[14] S. Chu, L. Hollberg, J. E. Bjorkholm, A. Cable, and A. Ashkin, *3-dimensional viscous confinement and cooling of atoms by resonance radiation pressure*, Phys. Rev. Lett. 55, 48 (1985).

[15] J. Dalibard and C. Cohen-Tannoudji, *Laser cooling below the Doppler limit by polarization gradients - simple theoretical-models*, J. Opt. Soc. Am. B – Opt. Phys. 6, 2023 (1989).

[16] T. Hnsch and A. Schawlow, *Cooling of gases by laser radiation*, Optics Communications 13, 68 (1975).

[17] W. D. Phillips and H. Metcalf, *Laser deceleration of an atomic-beam*, Phys. Rev. Lett. 48, 596 (1982).

[18] C. S. Adams and E. Riis, *Laser cooling and trapping of neutral atoms*, Prog. Quantum Electron. 21, 1 (1997).

[19] W. D. Phillips, *Nobel lecture: Laser cooling and trapping of neutral atoms*, Rev. Mod. Phys. 70, 721 (1998).

[20] N. Masuhara, J. M. Doyle, J. C. Sandberg, D. Kleppner, T. J. Greytak, H. F. Hess, and G. P. Kochanski, *Evaporative cooling of spin-polarized atomic-hydrogen*, Phys. Rev. Lett. 61, 935 (1988).

[21] C. C. Bradley, C. A. Sackett, J. J. Tollett, and R. G. Hulet, *Evidence of Bose-Einstein condensation in an atomic gas with attractive interactions*, Phys. Rev. Lett. 75, 1687 (1995).

[22] G. Modugno, G. Ferrari, G. Roati, R. J. Brecha, A. Simoni, and M. Inguscio, *Bose-Einstein condensation of potassium atoms by sympathetic cooling*, Science 294, 1320 (2001).

[23] S. L. Cornish, N. R. Claussen, J. L. Roberts, E. A. Cornell, and C. E. Wieman, *Stable rb-85 Bose-Einstein condensates with widely tunable interactions*, Phys. Rev. Lett. 85, 1795 (2000).

[24] T. Weber, J. Herbig, M. Mark, H. C. Nägerl, and R. Grimm, *Bose-Einstein condensation of cesium*, Science 299, 232 (2003).

[25] A. G. Truscott, K. E. Strecker, W. I. McAlexander, G. B. Partridge, and R. G. Hulet, *Observation of Fermi pressure in a gas of trapped atoms*, Science 291, 2570 (2001).

[26] D. G. Fried, T. C. Killian, L. Willmann, D. Landhuis, S. C. Moss, D. Kleppner, and T. J. Greytak, *Bose-Einstein condensation of atomic hydrogen*, Phys. Rev. Lett. 81, 3811 (1998).

[27] S. Kraft, F. Vogt, O. Appel, F. Riehle, and U. Sterr, *Bose-Einstein condensation of alkaline earth atoms:* ^{40}Ca, Phys. Rev. Lett. 103, 130401 (2009).

[28] Y. N. Martinez de Escobar, P. G. Mickelson, M. Yan, B. J. DeSalvo, S. B. Nagel, and T. C. Killian, *Bose-Einstein condensation of* ^{84}Sr, Phys. Rev. Lett. 103, 200402 (2009).

[29] J. Werner, A. Griesmaier, S. Hensler, J. Stuhler, and T. Pfau, *Observation of Feshbach resonances in an ultracold gas of* ^{52}Cr, Phys. Rev. Lett. 94, 183201 (2005).

[30] Y. Takasu, K. Maki, K. Komori, T. Takano, K. Honda, M. Kumakura, T. Yabuzaki, and Y. Takahashi, *Spin-singlet Bose-Einstein condensation of two-electron atoms*, Phys. Rev. Lett. 91, 040404 (2003).

[31] A. Frisch, M. Mark, K. Aikawa, F. Ferlaino, J. L. Bohn, C. Makrides, A. Petrov, and S. Kotochigova, *Quantum chaos in ultracold collisions of gas-phase erbium atoms*, Nature 507, 475 (2014).

[32] K. Baumann, N. Q. Burdick, M. Lu, and B. L. Lev, *Observation of low-field Fano-Feshbach resonances in ultracold gases of dysprosium*, Phys. Rev. A 89, 020701 (2014).

[33] P. S. Julienne, *Chaos in the cold*, Nature 507, 440 (2014).

[34] L. D. Carr, D. DeMille, R. V. Krems, and J. Ye, *Cold and ultracold molecules: science, technology and applications*, New J. Phys. 11, 055049 (2009).

[35] J. D. Weinstein, R. deCarvalho, T. Guillet, B. Friedrich, and J. M. Doyle, *Magnetic trapping of calcium monohydride molecules at millikelvin temperatures*, Nature 395, 148 (1998).

[36] M. D. D. Rosa, *Laser cooling molecules*, Eur. Phys. J. D. 31, 395 (2004).

[37] V. Zhelyazkova, A. Cournol, T. E. Wall, A. Matsushima, J. J. Hudson, E. A. Hinds, M. R. Tarbutt, and B. E. Sauer, *Laser cooling and slowing of CaF molecules*, Phys. Rev. A 89 (2014).

[38] B. Hemmerling, E. Chae, A. Ravi, L. Anderegg, G. K. Drayna, N. R. Hutzler, A. L. Collopy, J. Ye, W. Ketterle, and J. M. Doyle, *Laser slowing of CaF molecules to near the capture velocity of a molecular mot*, Journal of Physics B: Atomic, Molecular and Optical Physics 49, 174001 (2016).

[39] M. T. Hummon, M. Yeo, B. K. Stuhl, A. L. Collopy, Y. Xia, and J. Ye, *Magneto-optical trapping of diatomic molecules*, Phys. Rev. Lett. 110, 143001 (2013).

[40] M. Yeo, M. T. Hummon, A. L. Collopy, B. Yan, B. Hemmerling, E. Chae, J. M. Doyle, and J. Ye, *Rotational state microwave mixing for laser cooling of complex diatomic molecules*, Phys. Rev. Lett. 114 (2015).

[41] E. S. Shuman, J. F. Barry, and D. DeMille, *Laser cooling of a diatomic molecule*, Nature 467, 820 (2010).

[42] J. F. Barry, D. J. McCarron, E. B. Norrgard, M. H. Steinecker, and D. DeMille, *Magneto-optical trapping of a diatomic molecule*, Nature 512, 286 (2014).

[43] D. J. McCarron, E. B. Norrgard, M. H. Steinecker, and D. DeMille, *Improved magneto-optical trapping of a diatomic molecule*, New. J. Phys. 17 (2015).

[44] E. B. Norrgard, D. J. McCarron, M. H. Steinecker, M. R. Tarbutt, and D. DeMille, *Submillikelvin dipolar molecules in a radio-frequency magneto-optical trap*, Phys. Rev. Lett. 116, 063004 (2016).

[45] M. H. Steinecker, D. J. McCarron, Y. Zhu, and D. DeMille, *Improved radio-frequency magneto-optical trap of SrF molecules*, ChemPhysChem 17, 3664 (2016).

[46] S. Truppe, H. J. Williams, M. Hambach, L. Caldwell, N. J. Fitch, E. A. Hinds, B. E. Sauer, and M. R. Tarbutt, *Molecules cooled below the Doppler limit*, Nat. Phys. page doi:10.1038/nphys4241 (2017).

[47] I. Kozyryev, L. Baum, K. Matsuda, B. L. Augenbraun, L. Anderegg, A. P. Sedlack, and J. M. Doyle, *Sisyphus laser cooling of a polyatomic molecule*, Phys. Rev. Lett. 118, 173201 (2017).

[48] C. P. Koch and M. Shapiro, *Coherent control of ultracold photoassociation*, Chemical Reviews 112, 4928, pMID: 22489790 (2012).

[49] T. Köhler, K. Góral, and P. S. Julienne, *Production of cold molecules via magnetically tunable Feshbach resonances*, Rev. Mod. Phys. 78, 1311 (2006).

[50] F. A. van Abeelen and B. J. Verhaar, *Time-dependent Feshbach resonance scattering and anomalous decay of a na Bose-Einstein condensate*, Phys. Rev. Lett. 83, 1550 (1999).

[51] F. H. Mies, E. Tiesinga, and P. S. Julienne, *Manipulation of Feshbach resonances in ultracold atomic collisions using time-dependent magnetic fields*, Phys. Rev. A 61, 022721 (2000).

[52] E. Timmermans, P. Tommasini, M. Hussein, and A. Kerman, *Feshbach resonances in atomic Bose-Einstein condensates*, Phys. Rep. 315, 199 (1999).

[53] E. A. Donley, N. R. Claussen, S. T. Thompson, and C. E. Wieman, *Atom-molecule coherence in a Bose-Einstein condensate*, Nature 417, 529 (2002).

[54] J. Herbig, T. Kraemer, M. Mark, T. Weber, C. Chin, H. C. Nägerl, and R. Grimm, *Preparation of a pure molecular quantum gas*, Science 301, 1510 (2003).

[55] S. Dürr, T. Volz, A. Marte, and G. Rempe, *Observation of molecules produced from a Bose-Einstein condensate*, Phys. Rev. Lett. 92, 020406 (2004).

[56] K. Xu, T. Mukaiyama, J. R. Abo-Shaeer, J. K. Chin, D. E. Miller, and W. Ketterle, *Formation of quantum-degenerate sodium molecules*, Phys. Rev. Lett. 91, 210402 (2003).

[57] J. Cubizolles, T. Bourdel, S. J. J. M. F. Kokkelmans, G. V. Shlyapnikov, and C. Salomon, *Production of long-lived ultracold li-2 molecules from a Fermi gas*, Phys. Rev. Lett. 91, 240401 (2003).

[58] S. Jochim, M. Bartenstein, A. Altmeyer, G. Hendl, S. Riedl, C. Chin, J. Hecker Denschlag, and R. Grimm, *Bose-Einstein condensation of molecules*, Science 302, 2101 (2003).

[59] C. A. Regal, C. Ticknor, J. L. Bohn, and D. S. Jin, *Creation of ultracold molecules from a Fermi gas of atoms*, Nature 424, 47 (2003).

[60] A. Frisch, M. Mark, K. Aikawa, S. Baier, R. Grimm, A. Petrov, S. Kotochigova, G. Quéméner, M. Lepers, O. Dulieu, and F. Ferlaino, *Ultracold dipolar molecules composed of strongly magnetic atoms*, Phys. Rev. Lett. 115, 203201 (2015).

[61] P. K. Molony, P. D. Gregory, Z. Ji, B. Lu, M. P. Köppinger, C. R. Le Sueur, C. L. Blackley, J. M. Hutson, and S. L. Cornish, *Creation of ultracold* $^{87}Rb^{133}Cs$ *molecules in the rovibrational ground state*, Phys. Rev. Lett. 113, 255301 (2014).

[62] M. P. Köppinger, , D. J. McCarron, D. L. Jenkin, P. K. Molony, H.-W. Cho, S. L. Cornish, C. R. Le Sueur, C. L. Blackley, and J. M. Hutson, *Production of optically trapped* $^{87}Rb^{133}Cs$ *Feshbach molecules*, Phys. Rev. A 89, 033604 (2014).

[63] T. Takekoshi, L. Reichsöllner, A. Schindewolf, J. M. Hutson, C. R. Le Sueur, O. Dulieu, F. Ferlaino, R. Grimm, and H.-C. Nägerl, *Ultracold dense samples of dipolar RbCs molecules in the rovibrational and hyperfine ground state*, Phys. Rev. Lett. 113, 205301 (2014).

[64] P. K. Molony, P. D. Gregory, A. Kumar, C. R. Le Sueur, J. M. Hutson, and S. L. Cornish, *Production of ultracold* $^{87}Rb^{133}Cs$ *in the absolute ground state: complete characterisation of the STIRAP transfer*, Chem. Phys. Chem. (2016).

[65] P. D. Gregory, J. Aldegunde, J. M. Hutson, and S. L. Cornish, *Controlling the rotational and hyperfine state of ultracold* $^{87}Rb^{133}Cs$ *molecules*, Phys. Rev. A 94, 041403(R) (2016).

[66] M. Gröbner, P. Weinmann, E. Kirilov, H.-C. Nägerl, P. S. Julienne, C. R. Le Sueur, and J. M. Hutson, *Observation of interspecies Feshbach resonances in an ultracold* ^{39}K-^{133}Cs *mixture and refinement of interaction potentials*, Phys. Rev. A 95, 022715 (2017).

[67] H. J. Patel, C. L. Blackley, S. L. Cornish, and J. M. Hutson, *Feshbach resonances, molecular bound states, and prospects of ultracold-molecule formation in mixtures of ultracold K and Cs*, Phys. Rev. A 90, 032716 (2014).

[68] P. S. Julienne, *Ultracold molecules from ultracold atoms: a case study with the krb molecule*, Faraday Discuss. 142, 361 (2009).

[69] K.-K. Ni, S. Ospelkaus, M. H. G. de Miranda, A. Pe'er, B. Neyenhuis, J. J. Zirbel, S. Kotochigova, P. S. Julienne, D. S. Jin, and J. Ye, *A high phase-space-density gas of polar molecules in the rovibrational ground state*, Science 322, 231 (2008).

[70] P. S. Żuchowski, J. Aldegunde, and J. M. Hutson, *Ultracold RbSr molecules can be formed by magnetoassociation*, Phys. Rev. Lett. 105, 153201 (2010).

[71] J. W. Park, S. A. Will, and M. W. Zwierlein, *Ultracold dipolar gas of fermionic* $^{23}Na^{40}K$ *molecules in their absolute ground state*, Phys. Rev. Lett. 114, 205302 (2015).

[72] S. F. Yelin, K. Kirby, and R. Coté, *Schemes for robust quantum computation with polar molecules*, Phys. Rev. A 74, 050301(R) (2006).

[73] D. DeMille, *Quantum computation with trapped polar molecules*, Phys. Rev. Lett. 88, 067901 (2002).

[74] P. Rabl, D. DeMille, J. M. Doyle, M. D. Lukin, R. J. Schoelkopf, and P. Zoller, *Hybrid quantum processors: Molecular ensembles as quantum memory for solid state circuits*, Phys. Rev. Lett. 97, 033003 (2006).

[75] A. Micheli, G. K. Brennen, and P. Zoller, *A toolbox for lattice-spin models with polar molecules*, Nat. Phys. 2, 341 (2006).

[76] I. M. Georgescu, S. Ashhab, and F. Nori, *Quantum simulation*, Rev. Mod. Phys. 86, 153 (2014).

[77] T. E. Wall, *Preparation of cold molecules for high-precision measurements*, Journal of Physics B: Atomic, Molecular and Optical Physics 49, 243001 (2016).

[78] A. Derevianko and H. Katori, *Colloquium: Physics of optical lattice clocks*, Rev. Mod. Phys. 83, 331 (2011).

[79] G. Wilpers, T. Binnewies, C. Degenhardt, U. Sterr, J. Helmcke, and F. Riehle, *Optical clock with ultracold neutral atoms*, Phys. Rev. Lett. 89, 230801 (2002).

[80] D. DeMille, S. Sainis, J. Sage, T. Bergeman, S. Kotochigova, and E. Tiesinga, *Enhanced sensitivity to variation of m_e/m_p in molecular spectra*, Phys. Rev. Lett. 100, 043202 (2008).

[81] T. Zelevinsky, S. Kotochigova, and J. Ye, *Precision test of mass-ratio variations with lattice-confined ultracold molecules*, Phys. Rev. Lett. 100, 043201 (2008).

[82] V. V. Flambaum and M. G. Kozlov, *Enhanced sensitivity to the time variation of the fine-structure constant and $m_\mathrm{p}/m_\mathrm{e}$ in diatomic molecules*, Phys. Rev. Lett. 99, 150801 (2007).

[83] J. J. Hudson, B. E. Sauer, M. R. Tarbutt, and E. A. Hinds, *Measurement of the electron electric dipole moment using YbF molecules*, Phys. Rev. Lett. 89, 023003 (2002).

[84] J. J. Hudson, D. M. Kara, J. Smallman, B. E. Sauer, M. R. Tarbutt, and E. A. Hinds, *Improved measurement of the shape of the electron*, Nature London 473, 493 (2011).

[85] M. R. Tarbutt, B. E. Sauer, J. J. Hudson, and E. A. Hinds, *Design for a fountain of YbF molecules to measure the electron's electric dipole moment*, New Journal of Physics 15, 053034 (2013).

[86] L. Santamaria, C. Braggio, G. Carugno, V. D. Sarno, P. Maddaloni, and G. Ruoso, *Axion dark matter detection by laser spectroscopy of ultracold molecular oxygen: a proposal*, New Journal of Physics 17, 113025 (2015).

[87] D. G. Green, C. L. Vaillant, M. D. Frye, M. Morita, and J. M. Hutson, *Quantum chaos in ultracold collisions between $Yb(^1S_0)$ and $Yb(^3P_2)$*, Phys. Rev. A 93, 022703 (2016).

[88] T. Maier, H. Kadau, M. Schmitt, M. Wenzel, I. Ferrier-Barbut, T. Pfau, A. Frisch, S. Baier, K. Aikawa, L. Chomaz, M. J. Mark, F. Ferlaino,

C. Makrides, E. Tiesinga, A. Petrov, and S. Kotochigova, *Emergence of chaotic scattering in ultracold Er and Dy*, Phys. Rev. X 5, 041029 (2015).

[89] M. D. Frye, M. Morita, C. L. Vaillant, D. G. Green, and J. M. Hutson, *Approach to chaos in ultracold atomic and molecular physics: Statistics of near-threshold bound states for Li+CaH and Li+CaF*, Phys. Rev. A 93, 052713 (2016).

[90] R. V. Krems, *Cold controlled chemistry*, Phys. Chem. Chem. Phys. 10, 4079 (2008).

[91] T. V. Tscherbul, J. Kłos, and A. A. Buchachenko, *Ultracold spin-polarized mixtures of $^2\Sigma$ molecules with S-state atoms: Collisional stability and implications for sympathetic cooling*, Phys. Rev. A 84, 040701 (2011).

[92] V. Singh, K. S. Hardman, N. Tariq, M.-J. Lu, A. Ellis, M. J. Morrison, and J. D. Weinstein, *Chemical reactions of atomic lithium and molecular calcium monohydride at 1 k*, Phys. Rev. Lett. 108, 203201 (2012).

[93] N. Balakrishnan and A. Dalgarno, *Chemistry at ultracold temperatures*, Chem. Phys. Lett. 341, 652 (2001).

[94] L. Essen and J. V. L. Parry, *An atomic standard of frequency and time interval: A cesium resonator*, Nature 176, 280 (1955).

[95] A. G. Martin, K. Helmerson, V. S. Bagnato, G. P. Lafyatis, and D. E. Pritchard, *rf spectroscopy of trapped neutral atoms*, Phys. Rev. Lett. 61, 2431 (1988).

[96] C. Chin and P. S. Julienne, *Radio-frequency transitions on weakly bound ultracold molecules*, Phys. Rev. A 71, 012713 (2005).

[97] G. Zürn, T. Lompe, A. N. Wenz, S. Jochim, P. S. Julienne, and J. M. Hutson, *Precise characterization of ^{6}Li Feshbach resonances using trap-sideband-resolved rf spectroscopy of weakly bound molecules*, Phys. Rev. Lett. 110, 135301 (2013).

[98] C. A. Regal and D. S. Jin, *Measurement of positive and negative scattering lengths in a Fermi gas of atoms*, Phys. Rev. Lett. 90, 230404 (2003).

[99] S. Gupta, Z. Hadzibabic, M. W. Zwierlein, C. A. Stan, K. Dieckmann, C. H. Schunck, E. G. M. van Kempen, B. J. Verhaar, and W. Ketterle, *Radio-frequency spectroscopy of ultracold fermions*, Science 300, 1723 (2003).

[100] K. B. Davis, M.-O. Mewes, M. A. Joffe, M. R. Andrews, and W. Ketterle, *Evaporative cooling of sodium atoms*, Phys. Rev. Lett. 74, 5202 (1995).

[101] P. Zhang, P. Naidon, and M. Ueda, *Independent control of scattering lengths in multicomponent quantum gases*, Phys. Rev. Lett. 103, 133202 (2009).

[102] A. J. Moerdijk, B. J. Verhaar, and T. M. Nagtegaal, *Collisions of dressed ground-state atoms*, Phys. Rev. A 53, 6 (1996).

[103] Y. Ding, J. P. D'Incao, and C. H. Greene, *Effective control of cold collisions with radio-frequency fields*, Phys. Rev. A 95, 022709 (2017).

[104] S. T. Thompson, E. Hodby, and C. E. Wieman, *Ultracold molecule production via a resonant oscillating magnetic field*, Phys. Rev. Lett. 95, 190404 (2005).

[105] C. Klempt, T. Henninger, O. Topic, M. Scherer, L. Kattner, E. Tiemann, W. Ertmer, and J. J. Arlt, *Radio-frequency association of heteronuclear Feshbach molecules*, Phys. Rev. A 78, 061602 (2008).

[106] Beaufils, Q., Crubellier, A., Zanon, T., Laburthe-Tolra, B., Maréchal, É., Vernac, L., and Gorceix, O., *Radio-frequency association of molecules: an assisted Feshbach resonance*, Eur. Phys. J. D 56, 99 (2010).

[107] I. Mordovin, *Radio-frequency induced association of molecules in* ^{87}Rb, Ph.D. thesis, Swinburne University of Technology, Melbourne (2015).

[108] T. Lompe, T. B. Ottenstein, F. Serwane, A. N. Wenz, G. Zürn, and S. Jochim, *Radio-frequency association of Efimov trimers*, Science 330, 940 (2010).

[109] T. V. Tscherbul and S. T. Rittenhouse, *Three-body radio-frequency association of Efimov trimers*, Phys. Rev. A 84, 062706 (2011).

[110] O. Machtey, Z. Shotan, N. Gross, and L. Khaykovich, *Association of efimov trimers from a three-atom continuum*, Phys. Rev. Lett. 108, 210406 (2012).

[111] C. C. Agosta, I. F. Silvera, H. T. C. Stoof, and B. J. Verhaar, *Trapping of neutral atoms with resonant microwave radiation*, Phys. Rev. Lett. 62, 2361 (1989).

[112] D. DeMille, D. R. Glenn, and J. Petricka, *Microwave traps for cold polar molecules*, Eur. Phys. J. D 31, 375 (2004).

[113] P. S. Julienne, *Laser modification of ultracold atomic collisions in optical traps*, Phys. Rev. Let. 61, 698 (1988).

[114] O. Zobay and B. M. Garraway, *Two-dimensional atom trapping in field-induced adiabatic potentials*, Phys. Rev. Lett. 86, 1195 (2001).

[115] O. Zobay and B. M. Garraway, *Atom trapping and two-dimensional Bose-Einstein condensates in field-induced adiabatic potentials*, Phys. Rev. A 69, 23605 (2004).

[116] B. M. Garraway and H. Perrin, *Recent developments in trapping and manipulation of atoms with adiabatic potentials*, J. Phys. B 49, 172001 (2016).

[117] Y. Colombe, E. Knyazchyan, O. Morizot, B. Mercier, V. Lorent, and H. Perrin, *Ultracold atoms confined in rf-induced two-dimensional trapping potentials*, Europhys. Lett. 67, 593 (2004).

[118] K. Merloti, R. Dubessy, L. Longchambon, A. Perrin, P.-E. Pottie, V. Lorent, and H. Perrin, *A two-dimensional quantum gas in a magnetic trap*, New Journal of Physics 15, 033007 (2013).

[119] O. Morizot, Y. Colombe, V. Lorent, H. Perrin, and B. M. Garraway, *Ring trap for ultracold atoms*, Phys. Rev. A 74, 023617 (2006).

[120] W. H. Heathcote, E. Nugent, B. T. Sheard, and C. J. Foot, *A ring trap for ultracold atoms in an rf-dressed state*, New J. Phys. 10, 043012 (2008).

[121] B. E. Sherlock, M. Gildemeister, E. Owen, E. Nugent, and C. J. Foot, *Time-averaged adiabatic ring potential for ultracold atoms*, Phys. Rev. A 83, 043408 (2011).

[122] T. Schumm, S. Hofferberth, L. M. Andersson, S. Wildermuth, S. Groth, I. Bar-Joseph, P. Krüger, and J. Schmiedmayer, *Matter-wave interferometry in a double well on an atom chip*, Nature Physics 1, 57 (2005).

[123] I. Lesanovsky, S. Hofferberth, J. Schmiedmayer, and P. Schmelcher, *Manipulation of ultracold atoms in dressed adiabatic radio-frequency potentials*, Phys. Rev. A 74, 033619 (2006).

[124] I. Lesanovsky and W. von Klitzing, *Time-averaged adiabatic potentials: Versatile matter-wave guides and atom traps*, Phys. Rev. Lett. 99, 083001 (2007).

[125] P. Navez, S. Pandey, H. Mas, K. Poulios, T. Fernholz, and W. von Klitzing, *Matter-wave interferometers using TAAP rings*, New Journal of Physics 18, 075014 (2016).

[126] M. Göbel, *Low Dimensional Traps for Bose-Fermi Mixtures*, Ph.D. thesis, Ruperto-Carola University, Heidelberg (2008).

[127] N. Lundblad, P. J. Lee, I. B. Spielman, B. L. Brown, W. D. Phillips, and J. V. Porto, *Atoms in a radio-frequency-dressed optical lattice*, Phys. Rev. Lett. 100, 150401 (2008).

[128] W. Yi, A. J. Daley, G. Pupillo, and P. Zoller, *State-dependent, addressable subwavelength lattices with cold atoms*, New Journal of Physics 10, 073015 (2008).

[129] G. A. Sinuco-Len and B. M. Garraway, *Radio-frequency dressed lattices for ultracold alkali atoms*, New Journal of Physics 17, 053037 (2015).

[130] P. W. Courteille, B. Deh, J. Fortgh, A. Gnther, S. Kraft, C. Marzok, S. Slama, and C. Zimmermann, *Highly versatile atomic micro traps generated by multi-frequency magnetic field modulation*, Journal of Physics B: Atomic, Molecular and Optical Physics 39, 1055 (2006).

[131] B. Fröhlich, M. Feld, E. Vogt, M. Koschorreck, W. Zwerger, and M. Köhl, *Radio-frequency spectroscopy of a strongly interacting two-dimensional fermi gas*, Phys. Rev. Lett. 106, 105301 (2011).

[132] M. S. Child, *Molecular Collision Theory* (Academic Press, London, 1974).

[133] J. M. Hutson, *Theory of cold atomic and molecular collisions*, in R. V. Krems, W. C. Stwalley, and B. Friedrich (Editors), *Cold Molecules: Theory, Experiment, Applications*, pages 3–37 (Taylor & Francis, London, 2009).

[134] B. R. Johnson, *Multichannel log-derivative method for scattering calculations*, J. Comput. Phys. 13, 445 (1973).

[135] B. R. Johnson, *New numerical methods applied to solving one-dimensional eigenvalue problem*, J. Chem. Phys. 67, 4086 (1977).

[136] F. Mrugala and D. Secrest, *The generalized logderivative method for inelastic and reactive collisions*, J. Chem. Phys. 78 (1983).

[137] M. H. Alexander and D. E. Manolopoulos, *A stable linear reference potential algorithm for solution of the quantum close-coupled equations in molecular scattering theory*, J. Chem. Phys. 86, 2044 (1987).

[138] D. E. Manolopoulos, M. J. Jamieson, and A. D. Pradhan, *Johnson's log derivative algorithm rederived*, J. Comput. Phys. 105, 169 (1993).

[139] J. M. Hutson, *Coupled-channel methods for solving the bound-state Schrödinger equation*, Comput. Phys. Commun. 84, 1 (1994).

[140] E. Arimondo, M. Inguscio, and P. Violino, *Experimental determinations of the hyperfine structure in the alkali atoms*, Rev. Mod. Phys. 49, 31 (1977).

[141] T. M. Hanna, E. Tiesinga, and P. S. Julienne, *Creation and manipulation of Feshbach resonances with radiofrequency radiation*, New J. Phys. 12, 083031 (2010).

[142] J. M. Hutson and C. R. LeSueur, MOLSCAT*: a program for non-reactive quantum scattering calculations on atomic and molecular collisions*, arXiv:1811.09584 (2018).

[143] J. M. Hutson and C. R. LeSueur, BOUND *and* FIELD*: programs for calculating bound states of interacting pairs of atoms and molecules*, arXiv:1811.09111 (2018).

[144] D. J. Owens, T. Xie, and J. M. Hutson, *Creating Feshbach resonances for ultracold molecule formation with radiofrequency fields*, Phys. Rev. A 94, 023619 (2016).

[145] D. J. Owens and J. M. Hutson, *Inelastic losses in radiofrequency-dressed traps for ultracold atoms*, Phys. Rev. A 96, 042707 (2017).

[146] P. S. Żuchowski and J. M. Hutson, *Reactions of ultracold alkali metal dimers*, Phys. Rev. A 81, 060703(R) (2010).

[147] M. Aymar and O. Dulieu, *Calculation of accurate permanent dipole moments of the lowest* $^{1,3}\Sigma^+$ *states of heteronuclear alkali dimers using extended basis sets*, J. Chem. Phys. 122, 204302 (2005).

[148] M. Gröbner, P. Weinmann, F. Meinert, K. Lauber, E. Kirilov, and H.-C. Nägerl, *A new quantum gas apparatus for ultracold mixtures of K and Cs and KCs ground-state molecules*, Journal of Modern Optics 63, 1829 (2016).

[149] D. Borsalino, R. Vexiau, M. Aymar, E. Luc-Koenig, O. Dulieu, and N. Bouloufa-Maafa, *Prospects for the formation of ultracold polar ground state KCs molecules via an optical process*, Journal of Physics B: Atomic, Molecular and Optical Physics 49, 055301 (2016).

[150] M. Guo, B. Zhu, B. Lu, X. Ye, F. Wang, R. Vexiau, N. Bouloufa-Maafa, G. Quéméner, O. Dulieu, and D. Wang, *Creation of an ultracold gas of ground-state dipolar* $^{23}Na^{87}Rb$ *molecules*, Phys. Rev. Lett. 116, 205303 (2016).

[151] N. V. Vitanov, A. A. Rangelov, B. W. Shore, and K. Bergmann, *Stimulated Raman adiabatic passage in physics, chemistry, and beyond*, Rev. Mod. Phys. 89, 015006 (2017).

[152] D. Kleppner, *Professor Feshbach and his resonance*, Physics Today 57, 12 (2004).

[153] C. Chin, R. Grimm, E. Tiesinga, and P. S. Julienne, *Feshbach resonances in ultracold gases*, Rev. Mod. Phys. 82, 1225 (2010).

[154] A. J. Moerdijk, B. J. Verhaar, and A. Axelsson, *Resonances in ultracold collisions of ^{6}Li, ^{7}Li, and ^{23}Na*, Phys. Rev. A 51, 4852 (1995).

[155] M. Theis, G. Thalhammer, K. Winkler, M. Hellwig, G. Ruff, R. Grimm, and J. Hecker Denschlag, *Tuning the scattering length with an optically induced Feshbach resonance*, Phys. Rev. Lett. 93, 123001 (2004).

[156] J. M. Hutson, *Feshbach resonances in the presence of inelastic scattering: threshold behavior and suppression of poles in scattering lengths*, New J. Phys. 9, 152 (2007).

[157] M. D. Frye and J. M. Hutson, *Characterizing Feshbach resonances in ultracold scattering calculations*, Phys. Rev. A 96, 042705 (2017).

[158] R. Ferber, O. Nikolayeva, M. Tamanis, H. Knöckel, and E. Tiemann, *Long-range coupling of $X^1\Sigma^+$ and $a^3\Sigma^+$ states of the atom pair K+Cs*, Phys. Rev. A 88, 012516 (2013).

[159] M. Berninger, A. Zenesini, B. Huang, W. Harm, H.-C. Nägerl, F. Ferlaino, R. Grimm, P. S. Julienne, and J. M. Hutson, *Feshbach resonances, weakly bound molecular states and coupled-channel potentials for cesium at high magnetic field*, Phys. Rev. A 87, 032517 (2013).

[160] T. V. Tscherbul, T. Calarco, I. Lesanovsky, R. V. Krems, A. Dalgarno, and J. Schmiedmayer, *rf-field-induced Feshbach resonances*, Phys. Rev. A 81, 050701(R) (2010).

[161] D. H. Smith, *Inducing resonant interactions in ultracold atoms with a modulated magnetic field*, Phys. Rev. Lett. 115, 193002 (2015).

[162] J. J. Zirbel, K.-K. Ni, S. Ospelkaus, T. L. Nicholson, M. L. Olsen, P. S. Julienne, C. E. Wieman, J. Ye, and D. S. Jin, *Heteronuclear molecules in an optical dipole trap*, Phys. Rev. A 78, 013416 (2008).

[163] Q. Beaufils, A. Crubellier, T. Zanon, B. Laburthe-Tolra, É. Maréchal, L. Vernac, and O. Gorceix, *Radio-frequency association of molecules: an assisted Feshbach resonance*, The European Physical Journal D 56, 99 (2009).

[164] O. Morizot, L. Longchambon, R. Kollengode Easwaran, R. Dubessy, E. Knyazchyan, P.-E. Pottie, V. Lorent, and H. Perrin, *Influence of the radio-frequency source properties on rf-based atom traps*, Eur. Phys. J. D 47, 209 (2008).

[165] G.-B. Jo, Y. Shin, S. Will, T. A. Pasquini, M. Saba, W. Ketterle, D. E. Pritchard, M. Vengalattore, and M. Prentiss, *Long phase coherence time and number squeezing of two Bose-Einstein condensates on an atom chip*, Phys. Rev. Lett. 98, 030407 (2007).

[166] F. Baumgärtner, R. J. Sewell, S. Eriksson, I. Llorente-Garcia, J. Dingjan, J. P. Cotter, and E. A. Hinds, *Measuring energy differences by bec interferometry on a chip*, Phys. Rev. Lett. 105, 243003 (2010).

[167] I. Lesanovsky, T. Schumm, S. Hofferberth, L. M. Andersson, P. Krüger, and J. Schmiedmayer, *Adiabatic radio-frequency potentials for the coherent manipulation of matter waves*, Phys. Rev. A 73, 033619 (2006).

[168] N. Lundblad, S. Ansari, Y. Guo, and E. Moan, *Observations of $\lambda/4$ structure in a low-loss radio-frequency-dressed optical lattice*, Phys. Rev. A 90, 053612 (2014).

[169] M. Shotter, D. Trypogeorgos, and C. Foot, *Enhancement of on-site interactions of tunneling ultracold atoms in optical potentials using radio-frequency dressing*, Phys. Rev. A 78, 051602(R) (2008).

[170] K. A. Burrows, H. Perrin, and B. M. Garraway, *Non-adiabatic losses from radio-frequency dressed cold atom traps: beyond the Landau-Zener model*, Phys. Rev. A 96, 023429 (2017).

[171] M. T. Cvitaš, P. Soldán, J. M. Hutson, P. Honvault, and J. M. Launay, *Interactions and dynamics in Li + Li_2 ultracold collisions*, J. Chem. Phys. 127, 074302 (2007).

[172] C. Strauss, T. Takekoshi, F. Lang, K. Winkler, R. Grimm, J. Hecker Denschlag, and E. Tiemann, *Hyperfine, rotational, and vibrational structure of the $a^3\Sigma_u^+$ state of $^{87}Rb_2$*, Phys. Rev. A 82, 052514 (2010).

[173] G. F. Gribakin and V. V. Flambaum, *Calculation of the scattering length in atomic collisions using the semiclassical approximation*, Phys. Rev. A 48, 546 (1993).

[174] S. Falke, H. Knöckel, J. Friebe, M. Riedmann, E. Tiemann, and C. Lisdat, *Potassium ground-state scattering parameters and born-oppenheimer potentials from molecular spectroscopy*, Phys. Rev. A 78, 012503 (2008).

[175] T. L. Harte, E. Bentine, K. Luksch, A. J. Barker, D. Trypogeorgos, B. Yuen, and C. J. Foot, *Ultracold atoms in multiple radio-frequency dressed adiabatic potentials*, Phys. Rev. A 97, 013616 (2018).

[176] D. Trypogeorgos and C. J. Foot, *Cotrapping different species in ion traps using multiple radio frequencies*, Phys. Rev. A 94, 023609 (2016).

[177] T. Morgan, T. Busch, and T. Fernholz, *Adiabatic potentials using multiple radio frequencies*, arXiv:1405.2534 (2014).

[178] E. Bentine, T. L. Harte, K. Luksch, A. J. Barker, J. Mur-Petit, B. Yuen, and C. J. Foot, *Species-selective confinement of atoms dressed with multiple radiofrequencies*, Journal of Physics B: Atomic, Molecular and Optical Physics 50, 094002 (2017).

[179] C. J. Myatt, E. A. Burt, R. W. Ghrist, E. A. Cornell, and C. E. Wieman, *Production of two overlapping Bose-Einstein condensates by sympathetic cooling*, Phys. Rev. Lett. 78, 586 (1997).

[180] P. S. Julienne, F. H. Mies, E. Tiesinga, and C. J. Williams, *Collisional stability of double Bose condensates*, Phys. Rev. Lett. 78, 1880 (1997).

[181] F. H. Mies, C. J. Williams, P. S. Julienne, and M. Krauss, *Estimating bounds on collisional relaxation rates of spin-polarized ^{87}Rb atoms at ultracold temperatures*, J. Res. Natl. Inst. Stand. Technol. 101, 521 (1996).